Evolution of the shell structure in medium-mass nuclei : search for the 2d5/2 neutron orbital in 69Ni

Mohamad Moukaddam

Institut Pluridisciplinaire Hubert CURIEN STRASBOURG

UMR 7178

N° d'ordre : 1389

Thèse

Thèse

Présentée par

Mohamad MOUKADDAM

pour l'obtention du grade de
Docteur de l'Université de Strasbourg

Spécialité : Physique Subatomique

Évolution de la structure en couches dans les noyaux de masses moyennes: Recherche de l'orbitale $2d_{5/2}$ neutron dans le ^{69}Ni

Evolution of the shell structure in medium-mass nuclei: Search for the $2d_{5/2}$ neutron orbital in ^{69}Ni

Soutenue publiquement le 08 Mars 2012

Composition du jury:

Dr. Patricia ROUSSEL-CHOMAZ	Rapporteur externe
Dr. Nigel ORR	Rapporteur externe
Pr. Benoît GALL	Examinateur
Dr. Florent HAAS	Examinateur
Dr. Gilbert DUCHÊNE	Directeur de thèse
Dr. Didier BEAUMEL	Co-Directeur de thèse

Institut Pluridisciplinaire Hubert Curien – Département de Recherches Subatomiques
23 rue du Loess
BP 28
F-67037 Strasbourg cedex 2
Tél. : +33 (0) 3 88 10 6656
Fax : +33 (0) 3 88 10 6292
http://iphc.in2p3.fr/

CNRS IN2P3 Les deux infinis

UNIVERSITÉ DE STRASBOURG

UNIVERSITÉ DE STRASBOURG

ÉCOLE DOCTORALE DE PHYSIQUE ET CHIMIE PHYSIQUE

DÉPARTEMENT DE RECHERCHE SUBATOMIQUE

T H È S E

pour obtenir le grade de

Docteur de l'Université de Strasbourg

Spécialité : Physique Nucléaire

préparée au laboratoire

Institut Pluridisciplinaire Hubert Curien

Mohamad Moukaddam

Évolution de la structure en couches dans les noyaux de masse moyenne :

Recherche de l'orbitale $2d_{5/2}$ neutron dans le ^{69}Ni

Evolution of the shell structure in medium-mass nuclei : Search for the $2d_{5/2}$ neutron orbital in ^{69}Ni

Thèse dirigée par

Gilbert Duchêne et Didier Beaumel

Jury :

Rapporteur externe :	Mme. Patricia Roussel-Chomaz, CEA, Saclay
Rapporteur externe :	M. Nigel Orr, CNRS, LPC Caen
Examinateur :	M. Benoît Gall, Université de Strasbourg
Examinateur :	M. Florent Haas, CNRS, IPHC
Directeur :	M. Gilbert Duchêne, CNRS, IPHC
Co-Directeur :	M. Didier Beaumel, CNRS, IPN Orsay
Invitée :	Mme. Kamila Sieja, CNRS, IPHC

Acknowledgements

Studying how nature works is no doubt a blessing, how a tree grows or how our sun generates its energy is as beautiful as they appear. I know that not every person is lucky enough to work in the field he likes the most and I must say that physics has been, and still is, my passion since many years and I'm very happy that I've reached this stage of my life. However, I have not gotten there alone. I want to thank every person who helped make this goal possible for me to be at this point.

I would like to start by thanking Christelle Roy and Daniel Huss the present and former directors of the IPHC laboratory for giving me the opportunity to realize my Ph.D. studies and to continue my "scientific" path. A warm thank you also goes to Dr. Marc Rousseau, the director assistant, and M. Jean Schihin, the administrative director. Regards to all of you for facilitating my stay at the IPHC until this very moment.

I would also like to thank my Ph.D. advisors Dr. Gilbert Duchêne and Dr. Didier Beaumel. Thank you for all the help you have given me throughout the Ph.D., mostly through the experiment preparation, the data analysis and the results interpretation and finally the elaboration of the manuscript. My regards to you for your patience and your time spent with me before several deadlines, for your guidance that you have provided in the third year when I was short of ideas. I am also most thankful for the time spent in discussing our respective visions on many of life's issues, I must say that I appreciate your sense of humor and your young spirit, without forgetting all the laughs we shared.

My thanks to Dr. Nigel Orr and Dr. Patricia Roussel-Chomaz for accepting to report my Ph.D. thesis. My "Super Heavy" regards to Professor Benoît Gall as the president of my Ph.D. comity, Dr. Florent Haas and Dr. Kamila Sieja as members of the jury. Your pertinent remarks, comments, questions and advices were very appreciated in this work.

I would also like to acknowledge all the librarians, secretaries, administrative and the IT stuff at the IPHC. In particular François Schmidt, Nicole Gross, Régine Sommer, Florence Diemer, Josiane Heidmann, Nadine Bauer, Gilles Schneider, Nicolas Busser, Fabienne Hamel, Sylviane Molinet, Jean-Pierre Froberger, Benoît Speckel and Jean Schuller, I am most appreciative of all your hard work with me.

A massive thank you goes to the nuclear structure group (CAN), I'm very glad for being a part of it, thank you all for creating this constant field of warmth, joy and above all easy-living. I would like to thank in particular Dr.×Dr. Christian Finck "le meilleur mec du monde" what I like to call him. Thank you for your help in the physics of MWPC and data analysis. You were always ready to answer my questions whenever I knocked on your door, sent you an e-mail or even an sms at anytime. Wherever I may go I'll be missing our critical-cynical-gloomy-black humor, specially in the morning.

I'm very grateful to Florent Haas for the wealth of knowledge he "radiates". His enthusiasm and appetite for knowledge has been rarely rivaled. Florent, I guess it's impossible to have a discussion with you (any time or any where) without learning something about physics and nuclear structure (even in an Irish pub!), I guess this is what I most appreciate in you.

Louise, thank you for the inspiring discussions time and time again, especially on the way back home from the laboratory (and while searching for a place to park your Volvo in our neighborhood). Despite our different backgrounds, and different cultures, it's very intriguing that we are on the same wavelength. I would also like to thank Olivier, Marc (as a colleague), Radomira and François Didierjean for your help and support during my Ph.D., I extend my thanks to Dominique Curien, Christian Beck, Sandrine, Regina, Marie-Hélène Sigward and François Le Blanc for your friendship and support.

Sharing the same floor with the nuclear theory group was very fruitful on the scientific and personal scale. Very special thanks to Fred & Kamila, our Shell-Modelists. Thank you for all your assistance with the Shell-Model calculations, for answering my questions and taking all the time with explaining to me the details of the Shell-Model theory. I would like also to thank you for the special time we spent in Zakopane conferences, it was *bardzo dobrze*! Thanks for your support here and there, now and then.

My thanks goes to Rimantas "Rimas" Lazauskas for helping me with Direct Reactions theory, several times I stepped in your office and I always had the answer on my way out. I want also to congratulate you for your newborn baby "Ula". A warm thanks to Hervé Molique, Johann "Johnny" Bartel my *tovarishch* (comrade), Marianne Dufour and Dominique Spehler. Thank you all for the nice chats we had around tea, and coffee or on the way to the canteen. My thanks to Professor Jerzy Dudek for accepting to be my tutoring advisor in the University of Strasbourg during my Ph.D., thanks also to professor Abdel-mjid Nourreddine who gave me the chance to teach final year undergraduates and for his help when I first came to France. My regards to Dr. Jean-Pierre Engel for being always next to Ph.D. students, thank you for your help at the beginning of my research journey (from Masters) I'll never forget. Your knowledge in statistics and data analysis is much appreciated.

I would like to thank my colleagues a lot, with whom I shared the office. Didier (Didi), it's been great, thank you for your patience and support (especially during the last months), the nice and very informative discussions we shared and above all your sense of humor. I hope that our *beloved* plant, *"BellaCommeTwilight"* will bare witness to our collaboration despite all our differences. Thanks also to Monika and Loïc, with whom I shared this office at different periods.

Many thanks to my Ph.D. fellows Al (one pint is not enough), Samir (mistmorth), Anto (Duc of Moselle-land), Marroush (meine symmetrischen), Dave, Doro, Juju, Flo, Khodor (ezZanjabil), Helenko, Arthuro, David, Estelle, Swensy and Jerôme with whom I shared my best moments on the IPHC campus and in Strasbourg. For those who already finished their Ph.D., I wish them all the success in their new carriers, and for the others I wish you the best of luck in this world!

Few people know what does it means to analyze data from MUST2. Big thanks to my brothers in arms "the MUSTers" Sandra Giron, Geoffroy Burgunder, Adrien Matta and Freddy Flavigny it has been a pleasure to work with you. I'm so thankful for your help during the analysis and I wish you all the best in your carriers. I hope our friendship will find its path no matter what. I would also like to thank the NESTER group at IPNO in particular Faïrouz Hammache, Jack Guillot, Jean-Antoine Scarpaci, Nicolas de Séréville, Pierre Roussel and Serge Franchoo. I extend my thanks to the nuclear Structure groups of GANIL and IRFU/CEA especially Valérie Lapoux, Olivier Sorlin and Laurent Nalpas for being present in our analysis meetings. My thanks goes also to all researchers (LISE team and LPCCaen), engineers and technicians (from Paris and Caen), for setting-up the MUST2 experimental campaign.

Away from research life I've been very lucky to meet the finest people at the dormitories of the "Robertsau". Water-sliding in the corridor of *the forth floor*, group-dinners, dance parties, "Orangerie" park go-outs and many other "conneries" are amongst my sweetest memories. Thanks, in particular, to Lili, Ugur, Amine, Marie, Rym, Clara, Ermal, Julie and Valou. You have always been next to me like a family, I hope our friendship will last longer than my stay in France. I wish you all the best in your lives.

I would like to thank my friends and compatriots Mohamad, Hassaan, Wassila, Inaya & Laurent with whom I had a friendship for more than a decade. Thank you for your caring and support, I hope stay tuned despite the long distances separating us.

Finally I would like to thank my mother and father, my sisters Abir, Nisrine and Farah. I appreciate everything you have done for me until the end of days. If I had the choice to choose my family, I would definitely chose you. Without your love, appreciation, caring and help, I could never be where I am now.

And now my charms are all o'erthrown
And what strength I have's mine own
Which is most faint; now t'is true
I must here be released by you
But release me from my bands
With the help of your good hands
Gentle breath of yours my sails
Must fill, or else my project fails,
Which was to please...

From "The Tempest", by William Shakespeare.

To Aya, Hazar, Adam, Jana, Ala and Lamar.
Love you all khalo!

Résumé en français

Introduction

Ce travail présente l'analyse d'une expérience de physique nucléaire, E507, réalisée en 2009 auprès du "Grand Accélérateur National d'Ions Lourds" (GANIL). Elle fait partie d'une campagne de mesures comprenant deux autres expériences (E530 et E546) qui utilisent le même montage expérimental et visent à étudier la structure nucléaire de noyaux loin de la stabilité.

Le noyau est un ensemble de *"N"* fermions (protons et neutrons) en interaction. Une compréhension complète de sa structure, nécessite la connaissance de l'interaction entre ses composants, ainsi que de puissants outils théoriques pour résoudre le problème fondamental à N-corps. L'interaction entre les nucléons, au sein du noyau, n'est pas complètement connue à l'heure actuelle. Cela rend difficile un traitement du noyau dans une approche purement fondamentale afin d'aider à la compréhension de sa structure. Pour surmonter ces difficultés, des modèles ont été conçus qui tiennent compte, d'une manière effective, des effets de ces interactions mal connues. Ils ont été développés en se basant sur les propriétés des noyaux stables dont ils ont à reproduit les caractéristiques observées expérimentalement et offrent une compréhension globale de la structure nucléaire.

Cependant, le développement des techniques expérimentales (séparation, identification, détection des noyaux, des particules légères, des rayonnements gamma,...) en physique nucléaire, a étendu notre exploration vers des régions très éloignées de la stabilité. Les propriétés des noyaux exotiques (faibles énergies de liaison et grands isospins) permet de tester les modèles établis avec les noyaux stables afin d'améliorer notre compréhension de la structure nucléaire.

Motivations physiques

L'énergie de la couche neutron $2d_{5/2}$ a un impact important sur l'évolution de la structure nucléaire dans la région $N \approx 40$, dans le cadre du modèle en couches. L'expérience a montré que la structure des isotopes riches en neutrons ($N \approx 40$) de Fe et Cr, 2 et 4 protons en-dessous de la fermeture de couche $Z = 28$, sont très déformés dans leur état fondamental [Sorl 03, Ljun 10]. Ce comportement n'a pas été observé le long de la chaîne isotopique voisine des Ni en particulier dans le $^{68}_{28}Ni_{40}$. Ce dernier présente même un comportement de fermeture de couche à $N = 40$ selon les valeurs de $B(E2)$ et $E(2^+)$ [Brod 95, Sorl 02].

Cette érosion brusque de la fermeture de couche à $N = 40$ dans le ^{68}Ni quand on passe à d'autre chaines isotopiques, tel que Fe et Cr, semble similaire au mécanisme qui conduit à l'îlot d'inversion à $N \approx 20$. Dans les deux cas la déformation est provoquée par les excitations quadrupolaires dû à l'occupation par les neutrons des couches appartenant à l'oscillateur harmonique supérieure et présentant une différence de moment orbital $\Delta l = 2$.

Les calculs effectués dans cette région de masse prédisent un nouvel îlot d'inversion à $N = 40$ semblable à celui découvert à $N = 20$. Dans tous ces calculs, l'orbitale neutron $2d_{5/2}$ a été placée de manière à reproduire les données expérimentales permettant l'apparition de la déformation dans la région. Or le gap énergétique $2d_{5/2} - 1g_{9/2}$ à $N = 40$ dans le ^{69}Ni n'a pas été mesuré jusqu'à présent.

L'objectif principal de ce travail est de déterminer expérimentalement ce gap, ce qui est essentiel pour comprendre la structure nucléaire, autour de $N = 40$. La mesure permettera également de prévoir la magicité ou la déformation de ^{78}Ni. Il est à noter que ce noyau se trouve sur le chemin du r-process de nucléosynthèse dans l'explosion supernovae de type II.

Le noyau en question, ^{69}Ni, a déjà été étudié par la désexcitation d'isomère et des corrélations $\beta - \gamma$. Plusieurs états ont déjà été observés jusqu'à ≈ 2700 keV. Cependant, en raison des techniques expérimentales et de la structure de ^{69}Ni, la couche neutron $2d_{5/2}$ n'a pas encore été observée et aucune information concernant cet état n'est disponible.

La réaction de stripping (d, p) est utilisée depuis longtemps comme moyen de sonder la structure en couches des noyaux en fournissant des informations détaillées sur l'énergie à particule individuelle des couches neutrons. Dans ce travail, nous avons utilisé la réaction de transfert $d(^{68}Ni, p)^{69}Ni$. Le noyau ^{69}Ni y est créé dans son état fondamental, qui correspond à l'occupation par le neutron de valence de la couche $1g_{9/2}$ ($l = 4$) ou dans un état excité tel que $2d_{5/2}$ ($l = 2$) qui est l'orbitale que nous recherchons. Grâce à une analyse des sections efficaces différentielles par l'Approximation de Born des Ondes Distordues (DWBA), le moment orbital l et les facteurs spectroscopiques SF des états peuplés peuvent être déterminés.

Montage expérimental

Malgré la durée de vie assez longue de ^{68}Ni (29(2) s), il n'est pas possible de produire et d'extraire chimiquement cet isotope pour fabriquer une cible. En conséquence, une expérience en cinématique directe dans laquelle un faisceau stable intéragit avec une cible de ^{68}Ni ne peut pas être envisagée. Pour surmonter cette difficulté technique, nous avons utilisé la cinématique inverse, où un faisceau de ^{68}Ni est produit et envoyé sur une cible stable contenant des deutons. Il est important de souligner que dans le cas d'une réaction en cinématique inverse, les protons, qui contiennent les informations sur structure du ^{69}Ni, émis dans les angles avant dans le système de centre de masse (CM) sont détectés aux angles arrières dans le système du laboratoire.

Un faisceau primaire de ^{70}Zn produit au GANIL, à une énergie de 62.5 MeV/u, a été fragmenté sur une cible de production de Be d'épaisseur 505 µm placée perpendiculairement au faisceau (à 0°). La fragmentation du ^{70}Zn produit un cocktail de noyaux qui a été filtré dans le spectromètre LISE3 [Anne 92], par la technique de séparation en vol (In-Flight separation), afin de sélectionner le noyau ^{68}Ni avec une bonne pureté ($\approx 85.8\%$ dans notre cas). Le faisceau secondaire contenant le noyau de ^{68}Ni à une énergie de 25.14 A. MeV a été ensuite conduit vers une cible de polyéthylène (CD_2) placée au centre du dispositif expérimental.

L'énergie d'excitation du ^{69}Ni produit par la réaction $d(^{68}Ni, p)$ a été calculée en utilisant la méthode de la "masse manquante" qui nécessite la connaissance de l'énergie et l'angle du proton émis avec une bonne précision. En général, les propriétés optiques des faisceaux d'ions radioactifs produits par fragmentation sont moins bonnes (large émittance et dispersion en énergie) que celles des faisceaux stables et sont caractérisées par des intensités très faibles partiellement compensées par l'utilisation de cibles relativement épaisses. Des dispositifs innovants sont utilisés afin de compenser ces caractéristiques.

L'utilisation de détecteurs de faisceau est primordiale. Nous avons utilisé les détecteurs CATS [Otti 99][1], chambres à fils à basse pression, spécialement conçues pour ce type d'expérience. Deux de ces détecteurs ont été placé en amont de la cible afin de reconstruire, événement par événement et avec précision, l'angle d'incidence des noyaux ^{68}Ni et la position de l'interaction sur la cible.

D'autre part, les contraintes liées à la cinématique inverse imposent l'utilisation de détecteurs de particules légères chargés de grande surface afin de maximiser la couverture en angle solide. L'identification en masse et en charge du noyau de recul détecté et la position et les résolutions en énergie sont essentielles à la qualité des spectres d'énergie d'excitation pour le noyau lourd ^{69}Ni. Pour cette raison, l'ensemble de détecteurs MUST2[2] [Poll 05] a été développé par l'IPN d'Orsay, CEA-Saclay/IRFU, et le GANIL. Le détecteur MUST2 est un ensemble de télescopes identiques, composés de deux étages de détecteurs silicium et d'un détecteur scintillateur de CsI spécialement conçus pour ce type d'expériences. Il s'agit d'une version améliorée de la première génération de déteteurs MUST [Blum 99], avec une plus grande surface de détection et une meilleure granularité, et d'une électronique moderne intégrée. Ces détecteurs ont été placés de façon à couvrir les angles arrières situés entre 104° et 150° dans le laboratoire. Pour les angles les plus en arrière se situant entre 155° et 170°, nous avons utilisé un autre détecteur de particules chargés, S1 [Micr 10], ayant une géométrie annulaire. Sa résolution en énergie et en angle proche de celle des détecteurs MUST2.

Les contaminants du faisceau et le matériel de la cible induisent des réactions parasites et conduisent à la production de protons dans les angles arrières qui contaminent le spectre d'énergie d'excitation du ^{69}Ni. Ces contaminations peuvent être considérablement réduites en imposant une coïncidence avec le noyau lourd de la réaction. Une chambre d'ionisation couplée avec un scintillateur plastique ont été placés au bout de la ligne de faisceau, afin de détecter et séparer les différentes composantes du faisceau.

[1] **C**hambre **À** **T**rajectoire de **S**aclay.
[2] **MU**r à **ST**rips.

Analyse des données

Les détecteurs CATS : Le passage d'un ion chargé dans un détecteur CATS va induire une distribution de charges sur les cathodes (pistes) X et Y du détecteur. Cette distribution de charges est utilisée pour calculer la meilleure estimation de la position de passage (P) du noyau incident. Cette procédure améliore la résolution ab initio égale à la largeur d'une piste (*i.e.* 2.34 mm). Une étude sur la répartition des charges a montré que le nombre minimal de pistes nécéssaires pour avoir une information sur la position de passage ne doit pas être inférieur à trois. Dans ce travail nous avons étudié deux classes différentes d'algorithmes de reconstruction: les méthodes du centre de gravité (COG) d'ordre "n" (où "n" est le nombre de pistes utilisées) et les méthodes analytiques [Lau 95].

Dans les méthodes du centre de gravité, P est calculée comme étant la moyenne sur les positions des pistes déclenchées, pondérées par leur charges respectives. Les auteurs dans [Lau 95, Otti 99] ont montré que selon le nombre de pistes utilisées la position calculée souffre d'erreurs systématiques et une correction doit être prise en compte afin de reproduire la véritable position. Ces erreurs systématiques sont à peu près linéaire dans le cas des méthodes COG d'ordre 3 et 4 et une simple correction peut être faite. D'autre part, les méthodes analytiques sont basées sur l'hypothèse que la distribution de charges peut être assimilée à une fonction en forme de cloche ayant 3 paramètres (amplitude, centroïde, largeur) comme une gaussienne (*Gaus*) ou une sécante hyperbolique au carrée (*Sech*). Dans ce type d'algorithme, réalisé toujours avec 3 pistes, P est calculée comme étant le centroïde de la fonction, ajustée sur les pistes ayant la charge la plus significative. Dans le cas de la *Sech* les pistes latérales doivent être à la même distance de la piste centrale. Les méthodes analytiques sont caractérisées par des erreurs systématiques bien inférieures à celles induites par les méthodes COG [Lau 95].

Afin de valider la reconstruction en position, une grille en laiton, percée de trous de différents diamètres (1 ou 2 mm) positionnés de manière asymétrique, a été placée derrière chaque CATS. L'image des trous a été recueillie sur chaque CATS et un test des algorithmes de reconstruction a été réalisé. La reconstruction utilisant la méthode COG pour 3 bandes a d'abord été testée en appliquant les corrections correpondantes [Lau 95, Otti 99]. La qualité de la reconstruction a été considérablement améliorée après la procédure de correction. Cependant, même avec un choix judicieux des facteurs de correction, l'image des trous présente des césures dues principalement aux erreurs sytématiques. Au contraire, ce phénomène n'a pas été observé lors d'une reconstruction avec les méthodes analytiques. Cela valide l'utilisation de ces méthodes durant l'analyse[3].

Compte tenu des positions de l'impact du faisceau sur les détecteurs CATS1 et CATS2, nous avons calculé la position de l'interaction du faisceau avec la cible en utilisant les distances CATS1-CATS2 et CATS2-cible et en supposant une trajectoire linéaire du noyau incident. Les résolutions du calcul de position en X ($0,65$ mm) et en Y ($0,4$ mm) sur les détecteurs CATS induit une incertitude sur l'angle d'incidence qui a été estimé à ($\sim 0,1°$). Cette incertitude est négligeable devant l'incertitude sur l'angle induite par le straggling en angle dans la cible et par l'incertitude due à la largeur des pistes dans les détecteurs

[3] On a préféré d'utiliser la fonction *Sech* caratérisée par l'erreur sytématique la plus faible [Lau 95].

S1 et MUST2. La largeur à mi-hauteur (LMH) de la distribution du temps de vol de l'ion entre CATS1 et CATS2 est utilisée pour déterminer leur résolution temporelle (0, 37 ns) en supposant que les deux détecteurs CATS ont à peu près les mêmes caractéristiques.

Les détecteurs MUST2 et S1 : Pour déterminer l'énergie et le temps des particules chargées légères dans les détecteurs MUST2 et S1, il est nécessaire de réaliser un étalonnage. Pour déterminer l'énergie mesurée par les détecteurs silicium à pistes (DSSD) dans MUST2 et S1 et les cristaux silicium-lithium (Si(Li)), subdivisées en 8 pads, situés derrière l'étage DSSD dans MUST2, nous avons utilisé une source 3-α dont les énergies d'émission sont connues avec précision.

Avant la procédure d'étalonnage des détecteurs un test avec la source 3-α a été réalisé sur la précision de positionnement de la cible[4] au cours de la campagne. Le nombre de coups reçus par chaque strip des 4 détecteurs MUST2 comparé aux résultats de simulations monte-carlo, dans a révélé des changements de la position du porte-cible, de l'ordre de quelques mm, à l'égard de sa position originale. Ces changements de position ont été pris en compte pendant l'étalonnage des détecteurs et l'analyse des données.

De même, l'épaisseur des couches mortes[5] des détecteurs MUST2 et S1 fournies par le constructeur des détecteurs ont été vérifiée et des écarts de $\sim 30\%$ ont été constatés par rapport aux valeurs trouvés dans ce travail. Leurs épaisseurs ont été redeterminés par une méthode d'étalonnage itérative et en supposant différentes valeurs d'épaisseur avec un pas de 0.1 µm. L'épaisseur minimisant le plus la différence entre le piédestal calculé et le piédestal physique (0 MeV) a été retenue pour l'analyse des données. Cette estimation de couches mortes est possible dans le cas de détecteurs dotés d'une réponse linéaire en fonction de l'énergie déposée. Les couches mortes associées aux cristaux Si(Li) de MUST2 ont été déterminées selon la même méthode.

La résolution en énergie (LMH) obtenue pour MUST2, en sommant les spectres en énergie de toutes les pistes des quatre détecteurs, est de 31 keV. Une résolution en énergie similaire de 30, 9 keV est mesurées pour le détecteur S1. Concernant les Si(Li), la résolution en énergie (LMH) atteinte en sommant tous les pads est de 66 keV.

Pendant l'analyse de données, les énergies des particules légères détectées sont corrigées des pertes d'énergie dans les couches mortes des détecteur en utilisant des tables de perte d'énergie du code SRIM. Une correction similaire a été appliquée pour la perte d'énergie de ces particules selon l'épaisseur effective traversée au sein de la cible qui dépend de l'angle d'émission. Comme aucune mesure dans l'expérience ne fournit l'endroit de l'intéraction du faisceau ^{68}Ni au sein de la cible, nous avons considéré que toutes les réactions ont lieu dans son plan central.

Le DSSD de MUST2 et S1 fournit une mesure de l'énergie cinétique (E) et une mesure du temps de vol (ToF) entre CATS2 et le détecteur déclenché. Les particules légères

[4] Le porte-cible est monté sur un bras mobile, contrôlé depuis de la chambre d'acquisition.

[5] Les couches mortes sont dues aux techniques de fabrication des détecteurs silicium en général. La collection des charges induite par les particules détectés n'est pas possible dans ces régions de détecteurs vu l'absence du champ électrique. En conséquence, elles peuvent induire une sous-estimation de l'énergie mesurée.

arrêtées dans le DSSD sont identifiées en utilisant la technique $ToF - E$. La ligne des protons est remarquable par l'énergie maximale déposée dans le DSSD qui à peu près égale à 6 MeV (8 MeV) et correspond à une épaisseur de 300 µm (500 µm) du DSSD dans MUST2 (S1). Quant aux particules qui deposent une partie de leur énergie dans le DSSD (dE) et s'arrêtent complétement dans le Si(Li) en déposant une énergie (E), elles sont identifiées à l'aide de la technique $\Delta E - E$.

Chambre d'ionisation et scintillateur plastique : La chambre d'ionisation et le scintillateur plastique ont été utilisés pour identifier les noyaux lourds de la réaction dont le ^{69}Ni. La performance de la chambre d'ionisation n'a pas été optimisée pour fonctionner à l'intensité nominale de l'expérience, *i.e.* $\approx 10^5$ *pps*, et souffrait d'un taux d'empilement "pile-up"[6] très important. Le principal contaminant, ^{70}Zn, représente 8 % de l'intensité du faisceau. Deux autres contaminants de moindre importance représentent 2 % et 3.8 % de l'intensité du faisceau. Ils étaient parfaitement séparables du ^{68}Ni mais n'ont pas été identifiés. La sélection de ^{68}Ni a été réalisée en corrélant l'énergie E dans le plastique en fonction du temps de vol CATS2-plastique.

Spectre d'énergie d'excitation : En connaisant les caractéristiques cinématiques de trois des quatre particules impliquées dans une réaction à deux corps, les caractéristiques de la dernière particule (^{69}Ni dans notre cas) sont déduites en utilisant les lois de conservation de l'énergie et de la quantité de mouvement. Dans cette expérience, nous avons mesuré l'énergie cinétique et la position du proton[7]. L'énergie d'excitation du ^{69}Ni a ensuite été calculée en utilisant la méthode de la "masse manquante".

Efficacité géométrique et section efficace différentielle : L'efficacité géométrique du système de détection est estimée par la simulation de Monte-Carlo développées dans ce travail et exposées dans l'annexe A. Elle prend en compte les positions des détecteurs MUST2 et S1 dans l'espace et simule une émission isotrope d'une source de particules située à la position de la cible. La variation de l'efficacité en fonction de l'angle d'émission est obtenue à partir du nombre de particules détectées dans un angle donné.

La section efficace différentielle expérimentale est calculée en tenant compte du nombre de particules ^{68}Ni incidentes, du nombre de noyaux de deutons dans la cible et du nombre de protons détectés dans chaque tranches angulaires corrigé par l'efficacité géométrique. Elle est exprimée dans le système de référence lié au laboratoire et doit être transformée dans le système de centre-de-masse (CM) afin d'être comparée à des sections efficaces calculées. La conversion se fait en utilisant le Jacobien [Mich 64] qui est un terme purement cinématique, qui transforme la section efficace d'un sytème de référence dans un autre système en mouvement de translation relatif.

[6] Empilement: (pile-up en anglais) Chevauchement en temps des signaux correspondant à l'énergie déposée des différentes particules détectés. Le "pile-up" réduit considérablement la résolution du détecteur.

[7] Les caractéristiques des particules dans la voie d'entrée sont connues.

Résultats expérimentaux

Afin d'extraire un spectre d'énergie d'excitation propre lié à la réaction d'intérêt, plusieurs sélections ont été faites. Les principales sont les suivantes:

- la zone de la cible CD_2 éclairée par le faisceau,
- les protons observés dans les détecteurs de particules chargées placés aux angles arrières et identifiés par les techniques $\Delta E - E$ et $ToF - E$,
- les noyaux de recul ^{69}Ni après identification des résidus lourds dans le scintillateur plastique en utilisant la technique $ToF - E$.

L'état fondamental et un état excité à environ $2,5$ MeV sont bien prononcés. En outre, des structures apparaissent vers 4 MeV et $6 - 7$ MeV. Une forte densité d'états est visible pour les énergies d'excitation au-dessus du seuil de séparation d'un neutron (S_n) qui vaut $4,59$ MeV. Le spectre finale était contaminé par un fond dû aux réactions parasites. Jusqu'à une énergie d'excitation d'environ 8 MeV, ce fond provient principalement de deux origines:

- les réactions dues Carbone dans la cible de CD_2,
- la cassure deuton induite par le faisceau.

Les deux fonds ont été soustraits du spectre d'excitation d'énergie afin d'en extraire les informations spectroscopiques.

Afin d'estimer le fond dues au Carbone dans la cible, la cible de CD_2 ($2,6$ mg/cm^2) est remplacée par une cible de Carbone pur de 2 mg/cm^2 d'épaisseur. Les données obtenues à partir de cette cible sont analysées de la même manière que les données de la cible CD_2. Le spectre d'énergie d'excitation correspondant fourni la forme du fond dû au Carbone. Ce dernier a été normalisé sur les énergies négatives du spectre d'excitation d'énergie obtenue avec la cible de CD_2 puis soustrait. Nous avons utilisé la méthode dite *"estimation par noyau"* [Parz 62] qui est une méthode statistique utilisée dans l'estimation de la fonction de densité de probabilité d'une variable aléatoire. Elle permet d'extraire une fonction de densité de probabilité non-parmétrique à partir d'un histogramme de faible statistique.

Le deuton est un noyau faiblement lié qui se brise facilement (break-up) en un proton et en neutron lors de collisions nucléaires. Le proton de cette réaction peut ensuite être détecté dans un détecteur MUST2 ou S1 et son spectre associé se rajoute à celui des protons de la réaction d'intérêt. Nous n'avons pas accès à la distribution de l'énergie des protons de brisure du deuton, comme ce fut le cas pour les protons dus au Carbone dans la cible de CD_2. Une méthode alternative a été utilisée pour estimer sa contribution au spectre d'excitation d'énergie. Contrairement à la réaction d'intérêt, cette réaction conduit à trois particules en voie de sortie. Pour une description complète de cette cinématique à 3-corps nous avons effectué des calculs d'espace de phase. Une estimation du fond proton induit par cette réaction est possible en utilisant des méthodes numériques de

type Monte-Carlo basées sur une réaction $d(^{68}Ni, pn)^{69}Ni$. Les quadrivecteurs énergie-impulsion des protons issus de ces calculs sont ensuite injectés dans la simulation pour en sélectionner les protons susceptibles d'être observés par nos détecteurs. Les protons virtuellement détectés sont stockés puis analysés de manière identique aux données réelles. Par cette procédure, le fond simulé tient compte de la fonction de réponse du dispositif expérimental telle que la résolution en énergie et l'efficacité de détection. Une distribution non-paramétrique basée sur la méthode d'*"estimation par noyau"* est utilisée pour estimer la forme de ce fond.

Les spectres d'énergie d'excitation sont analysés jusqu'à 8 MeV pour plusieurs plages angulaires choisies suivant l'efficacité géométrique du système de détection. La plage angulaire la plus arrière ($156° - 170°$) couverte par le détecteur S1 est prise comme référence car la contimination due au carbone et à la brisure du deuton y est plus faible. Cinq états ont été identifiés et leurs énergies ont été fixées. Deux d'entre eux sont situés au-dessus de l'énergie de séparation du neutron.

La section efficace différentielle expérimentale pour chaque état est extraite de la distribution angulaire des protons dans S1 et MUST2. Elle est comparée aux sections efficaces différentielles calculées par un modèle de réaction basé sur la théorie de DWBA[8] en utilisant un potentiel d'entrée adiabatique [Varn 91] et un potentiels de sortie [Koni 03]. Les sections efficaces différentielles ADWA sont calculées à l'aide du code DWUCK4 [Kunz 74]. Deux informations principales peuvent être obtenues à partir de l'analyse des sections efficaces différentielles. La forme de la distribution angulaire dépend du moment orbital transféré l. Le facteur spectroscopique SF est déduit de la section efficace différentielle expérimentale en utilisant une procédure de normalisation. Le SF est obtenu par un ajustement de χ^2 de la distribution théorique sur les données expérimentales.

Interprétation dans le cadre du modèle en couches

Le premier pic du spectre d'énergie d'excitation est identifié comme étant l'état fondamental de ^{69}Ni. L'analyse a permis de déterminer que le moment angulaire du transfert de neutrons est $l = 4$ ce qui correspond à l'orbitale $1g_{9/2}$ avec un facteur spectroscopique $SF = 0,53 \pm 0,13$. Les états correspondants à la partie restante de la force n'ont pas été peuplés dans cette expérience indiquant une forte fragmentation de cette orbitale dans ^{69}Ni. Selon les calculs du modèle en couches, l'essentiel de la force de l'orbitale $1g_{9/2}$ est concentré dans l'état fondamental et le reste est extrêmement fragmenté à des énergies plus élevées ce qui est en accord avec les résultats expérimentaux de ce travail. Cependant, les calculs prédisent une plus grande valeur du facteur spectroscopique à 0 MeV ($SF_{SM} = 0,86$). Cette différence entre la valeur expérimentale et le calcul peut être expliqué par l'absence des orbitales supérieures de la couche *gds* sans sous-estimer les incertitudes expérimentales et celles systématiques liées aux choix des potentiels utilisés dans les calculs DWBA et ADWA.

Le second pic correspond à un état excité de ^{69}Ni à 2,48 MeV. Un moment orbital $l = 2$ lui est clairement attribué, correspondant à l'orbitale $2d_{5/2}$ d'après l'analyse ADWA

[8] Distorted Wave Born Approximation : L'approximation de Born des ondes distordues.

avec un facteur spectroscopique de $0,86 \pm 0,22$. Il est important de mentionner que la largeur du pic (LMH) à cette énergie est $1,5$ fois plus grande que celle de l'état fondamental. Cette différence de largeur n'a pas été reproduite par une simulation GEANT4[9], dans laquelle les effets expérimentaux (résolutions des détecteurs et épaisseur de la cible) sont pris en compte. Cela suggère que l'état en question est un doublet. L'analyse du premier état excité donne un doublet d'énergies $2,05$ MeV et $2,74$ MeV, ayant comme facteurs spectroscopiques $0,32 \pm 0,10$ et $0,44 \pm 0,13$ respectivement, associé à un transfert $l = 2$.

Les calculs du modèle en couches prédisent la présence d'un doublet d'états $5/2$ à des énergies d'excitation faibles ($1,5$ MeV), ce qui est en bon accord avec la mesure. Toutefois, la distribution de la force du doublet $2d_{5/2}$ donnée par le modèle en couches est très asymétrique et ne peut pas expliquer la LMH observée expérimentalement pour le premier état excité. Cependant, la répartition de force entre les deux composantes du doublet donnée par le modèle en couche est sensible à l'énergie de l'orbitale $2d_{5/2}$ introduite dans le calcul. Un bon accord entre les calculs et le résultat expérimental est obtenu en augmentant l'énergie de l'orbitale $2d_{5/2}$ de 1 MeV. Cet effet a été utilisé pour fixer précisement la position de l'orbitale $2d_{5/2}$, jusqu'à présent déterminée indirectement dans les calculs du modèle en couches par l'apparition de la collectivité dans les noyaux riches en neutrons de Fe et Cr de la région $N \approx 40$. Nos résultats confirment l'énergie relativement basse de l'orbitale $2d_{5/2}$ dans le ^{68}Ni, et l'importance de tenir compte de l'orbitale en question dans les calculs de modèle en couches menés dans la région $N = 40$.

L'analyse ADWA du troisième pic à $4,19$ MeV d'énergie d'excitation montre que différentes valeurs de l sont possibles pour expliquer les résultats expérimentaux. L'attribution d'un moment orbital $l = 4$ correspondant à l'orbital $1g_{7/2}$ conduit à un facteur spectroscopique de $0,26 \pm 0,08$. D'autre part, l'attribution d'un moment orbital $l = 2$ conduit à un facteur spectroscopique de $0,51 \pm 0,15$ si l'état est identifié comme la population de l'orbitale $2d_{5/2}$. Le dernier cas est le plus favorisé vis-à-vis de la valeur de χ^2, si bien que la somme des facteurs spectroscopiques sur les premier et deuxième état excité viole la règle de somme ($SF = 1,27 \pm 0,38$). Cette attribution $2d_{5/2}$ est raisonnable si l'on tient compte des erreurs expérimentales. D'autre part, l'attribution $l = 4$ ($1g_{7/2}$) est en meilleur accord avec les calculs du modèle en couches puisque aucun fragment significatif de l'orbitale $2d_{5/2}$ n'est prévu vers $4 - 5$ MeV d'énergie d'excitation.

Au-dessus de l'énergie de séparation du neutron, deux résonnances sont observées aux énergies $5,43$ MeV et $6,39$ MeV. L'extraction de leur moment orbital souffre d'une part d'un manque de points expérimentaux dans leur distribution angulaire et d'autre part d'incertitudes sur l'importance du fond de la brisure du deuton. La comparaison avec les distributions calculées par ADWA est réalisée sur trois (quatre) des cinq points expérimentaux dans le cas de la première (deuxième) résonnance. Selon la minimisation de la valeur de χ^2, l'état à $5,43$ MeV peut correspondre à un transfert $l = 2$ associé à l'orbitale $2d_{3/2}$ avec un facteur spectroscopique de $1,64 \pm 0,42$ qui viole la règle de somme même si on tient compte des barres d'erreur. En outre, une telle attribution conduisant à un facteur spectroscopique voisin de l'unité n'est pas favorisée à ces énergies d'excitation auxquelles les orbitales ont plutôt tendance être très fragmentées. Par conséquent, une

[9]Effectué par nos collaborateur à l'IPN Orsay [Giro 11].

attribution d'un moment orbital $l \geqslant 4$ est privilégiée. Pour un transfert $l = 4$ (5) associé à la population de l'orbitale $1g_{7/2}$ ($1h_{11/2}$), nous trouvons un facteur spectroscopique $SF = 0,27 \pm 0,13$ ($SF = 0,17 \pm 0,04$). Le dernier état à $6,39$ MeV est raisonnablement reproduit par les distributions calculées correspondant aux transferts $l = 4$ ($SF = 0,52 \pm 0,13$). Les conditions expérimentales pour ces deux derniers états ne permettent pas d'attributions de moments angulaires et de valeurs de facteurs spectroscopiques plus tranchées. De plus les calculs du modèle en couches ne donnent aucune indication sur la nature de ces états car l'espace de valence utilisé pour les neutrons n'inclut pas les orbitales placées au-dessus de l'orbitale $2d_{5/2}$ ($3s_{1/2}$, $1g_{7/2}$, $2d_{3/2}$).

Conclusions et perspectives

Une expérience a été réalisée en 2009 au GANIL afin de rechercher l'orbitale neutron $2d_{5/2}$ dans le noyau ^{69}Ni. Le faisceau de ^{68}Ni était produit avec une énergie de $25,14$ MeV/u par la fragmentation d'un faisceau primaire de ^{70}Zn à une énergie de $62,5$ MeV/u sur une cible de production de Be. Les noyaux d'intérêt ont été sélectionnés à l'aide de la technique de séparation en vol dans le spectromètre magnétique LISE conduisant à un faisceau secondaire de ^{68}Ni assez pur ($\approx 85.8\%$). Celui-ci interagit avec une cible de CD_2 et produit des réactions de transfert d'un seul neutron $d(^{68}Ni, p)$ dont l'étude fait l'objet de ce travail. Ces réactions constituent un outil efficace pour déterminer l'énergie d'excitation, le moment orbital et le facteur spectroscopique des états peuplés à basse énergie d'excitation.

Cette étude est d'un grand intérêt pour la région $N \approx 40$ où la déformation des isotopes riches en neutrons de Fe et Cr a été mise en évidence expérimentalement à basse énergie d'excitation. Dans une approche de type modèle en couches, les excitations deux particules-deux trous de l'orbitale neutron $1g_{9/2}$ vers l'orbital neutron $2d_{5/2}$ contribuent fortement à cet effet, et ce d'autant plus que la différence d'énergie $1g_{9/2} - 2d_{5/2}$ est faible [Caur 05, Ljun 10, Lenz 10].

Le dispositif expérimental a été conçu pour l'étude des réactions directes dans une cinématique inverse. Le détecteurs CATS, MUST2, S1 ainsi qu'un scintillateur plastique ont permis la détection et l'identification de la particule légère chargée et des noyaux lourds en coïncidence. Le spectre d'énergie d'excitation du noyau lourd est calculé en utilisant la méthode de la masse manquante en se basant sur les mesures d'énergie et de position de la particule légère dans les détecteurs MUST2 et S1. L'identification des noyaux lourds dans le scintillateur plastique était obligatoire pour sélectionner la réaction d'intérêt.

L'étude de la réaction de transfert $d(^{68}Ni, p)$ a permis d'améliorer nos connaissances sur les états neutrons de basses énergies observés pour la première fois dans le ^{69}Ni. Cinq états ont été identifiés et les énergies correspondantes ont été établies. Deux d'entre eux sont situés au-dessus de l'énergie de séparation du neutron. La section efficace différentielle expérimentale pour chaque état est comparée aux résultats d'un modèle théorique basé sur la DWBA et utilisant un potentiel d'entrée adiabatique.

Le moment angulaire et le facteur spectroscopique correspondant à chaque état sont extraits par une minimisation de χ^2.

Finalement, les spectres d'énergie d'excitation obtenus au cours de ce travail présentaient une faible statistique. L'expérience montre les limitations du système de détection pour l'étude d'états d'énergie d'excitation élevée dans le ^{69}Ni. L'amélioration de l'efficacité de détection, de la résolution en énergie, de la granularité du détecteur et du débit des données du dispositif expérimental ainsi que l'augmentation des intensités de faisceaux exotiques sont les paramètres clés pour ce type d'études dans l'avenir. Les détecteurs tels que GASPARD (un détecteur au silicium à haute granularité pour la détection de particules chargées) couplé à PARIS et/ou AGATA (pour la détection des rayonnements γ), actuellement en cours de développement, ainsi que les futures installations de faisceaux radioactifs (SPIRAL2) permetteront de réaliser des avancées décisives dans la compréhension de la matière nucléaire aux limites de la stabilité.

Contents

Introduction

This work presents the analysis of a nuclear physics experiment, E507, performed in 2009 at the "Grand Accélérateur National d'Ions Lourds" (GANIL). It is a part of an experimental campaign including two other experiments (E530 and E546) using the same experimental setup and aiming to study the nuclear structure far away from stability.

Nuclear physics is the branch of modern physics that studies the properties of the atomic nucleus. In the late 19^{th} century, it was established that the matter was made up of atoms, all identical for a given chemical species. Following the pioneering work of Rutherford, a new picture of the composition of the atom has been proposed in 1911, the planetary model. The latter consists of negatively charged electrons orbiting around a positively charged nucleus, where almost all the mass is concentrated. In 1930, a very penetrating radiation was observed when bombarding light nuclei by alpha particles. A breakthrough in understanding the composition of the nucleus was achieved through the work of Frederic and Irène Joliot-Curie in 1932, by using this radiation to knock-out protons from hydrogenated material. This work led Chadwick to discover the nature of this radiation and at the same time the last constituent of the nucleus, the neutron.

As presently known, the nucleus is a system of *"A"* interacting fermions *i.e.* *"Z"* protons and *"N"* neutrons. A complete understanding of its structure, requires the knowledge of the interaction between its components as well as powerful theoretical tools to solve the mathematical problem generated by its many-body nature. The "full" interaction between nucleons inside the nucleus is not completely known at present, which induces difficulties to treat the nucleus in a pure fundamental approach in order to help understanding its structure. The situation gets even more difficult with inclusion of 3-body forces known to play important roles in the nucleus.

To overcome these difficulties, models have been devised taking into account via effective interactions the effects of such unknown correlations. These models were first developped based on the properties of stable nuclei and were able to some extent to reproduce the observed characteristics. However, the constant development of experimental techniques in nuclear physics, has extended our knowledge to regions far away from stability where the structure of exotic nuclei could be studied. The study of exotic nuclei offers a test of the proton-neutron interaction when different valence orbitals are occupied. In that way, new components of the nuclear force are explored for a better understanding of nuclear-matter properties.

The goal of the present work is to search for the $2d_{5/2}$ neutron state in the neutron-rich nucleus ^{69}Ni. The energy position of the $2d_{5/2}$ have a large impact on the shell evolution in the $N \approx 40$ region. Fe and Cr chains in this region exhibit large deformation [Sorl 03, Ljun 10] unlike the Ni chain that shows a different behaviour in particular $^{68}_{28}Ni_{40}$ which has a spherical character according to its $B(E2)$ and $E(2^+)$ values [Brod 95, Sorl 02].

Large-scale shell-model calculations [Lenz 10] are able to reproduce these deformations by including the neutron $2d_{5/2}$ orbital in the neutron valence space. They also predict that the energy of the $2d_{5/2}$ orbital is placed arround 1.5 MeV above the ground state. Moreover, knowing the position of the $2d_{5/2}$ neutron orbital in ^{69}Ni will help to conclude firmly about the magicity, or not, of ^{78}Ni.

The nucleus in question, ^{69}Ni, has already been studied by isomer-*decay* and $\beta-\gamma$ correlations, and several states have already been observed up to ≈ 2700 keV. However, due to the experimental techniques and the structure of ^{69}Ni, the $2d_{5/2}$ neutron orbital has not yet been observed and no information concerning this state was available. Direct reactions at low energy are a powerful tool to study the structure of nuclei. In particular, the transfer reactions provide access to the orbital momentum and spectroscopic factor of the different populated excited states. All of these characteristics are directly comparable to shell-model calculations. In this experiment we used the $d(^{68}Ni,p)^{69}Ni$ transfer reaction to feed the $2d_{5/2}$ neutron orbital .

Despite the rather long lifetime of ^{68}Ni (29(2) s) it is not possible to produce and extract this isotope in order to produce a target. Therefore, experiments in direct kinematics in which a *"known"* stable beam impinges a ^{68}Ni target cannot be envisaged. Instead, we use inverse kinematics where a beam of the unstable nuclei is produced (by fragmentation in our case) and sent on a stable target. The beam of ^{68}Ni was produced at GANIL at an energy of 25.14 A MeV and then guided by the LISE3 spectrometer [Anne 92] to a deuterated Polyethylene (CD_2) target in the experimental area.

In general, the optical properties of radioactive ion beams produced by fragmentation are poorer than those of stable ones and characterized by very low intensities. Innovative devices must be used in order to compensate these characteristics. Beam Trackers, such as CATS [Otti 99], are necessary to reconstruct with precision the angle of diffusion of the particles and the position of interaction on the target. On the other hand, the low intensity beams and inverse-kinematic constraints require detectors of large area in order to maximize the covered solid angle. In addition, position and energy resolutions are crucial to the quality of the excitation spectra obtained for the heavy residue. For this reason the MUST2 array [Poll 05] was developped by the IPN-Orsay, CEA-Saclay/IRFU, and GANIL collaboration. The MUST2 array [Blum 99] is an ensemble of identical telescopes, composed of several stages of silicon and CsI detectors especially designed for this type of experiments. It is an improved version of the first generation MUST array, with larger detection area and better resolution and using modern technology electronics.

In the first chapter we introduce the modern shell model, followed by a brief description of shell evolution at N=20 in a shell-model approach, believed to have a similar shell evolution mechanism to the region of interest at N=40. Then we discuss the onset of deformation around N=40 and the motivations that led us to study the ^{69}Ni nucleus. Finally, we make a short overview of the present understanding of ^{69}Ni nucleus structure. The second chapter is devoted to the experimental setup. We start by introducing the experimental method and its constraints. We then present briefly the beam production and guidance through LISE3 and the different detectors used for the data analysis. In the third chapter we present the offline analysis consisting of calibration and particle

identification for each detector. Then we present the reconstruction, in the beam tracker detectors and the light-charged particle detectors, of the physical observables used to calculate the excitation energies and the differential cross sections. Finally, in the fourth and final chapter, we present the excitation-energy spectrum after selecting the events of interest. Then we present the DWBA analysis of the calculated differential cross sections along with the identification of the energy levels and the extraction of the corresponding spectroscopic factors. Finally, we discuss the newly discovered states and the neutron $1g_{9/2} - 2d_{5/2}$ shell gap in ^{69}Ni and its impact on the shaping of nuclei arround $N = 40$.

Chapter 1

Physics motivations

1.1 Nuclear shell-model and magic numbers

Extensive studies of the experimental data, provided by direct experimentation on the atomic nucleus, have revealed certain regularities and correlations in its structure. Figure 1.1 shows the excitation energy of the first excited 2^+ state with respect to the number of neutrons in nuclei. The highest the excitation energy, the more difficult to excite the nucleus and the more stable it is. Independently of the isotopic chain, it is quite clear that nuclei having specific numbers of neutrons are particularly favored in terms of nuclear stability.

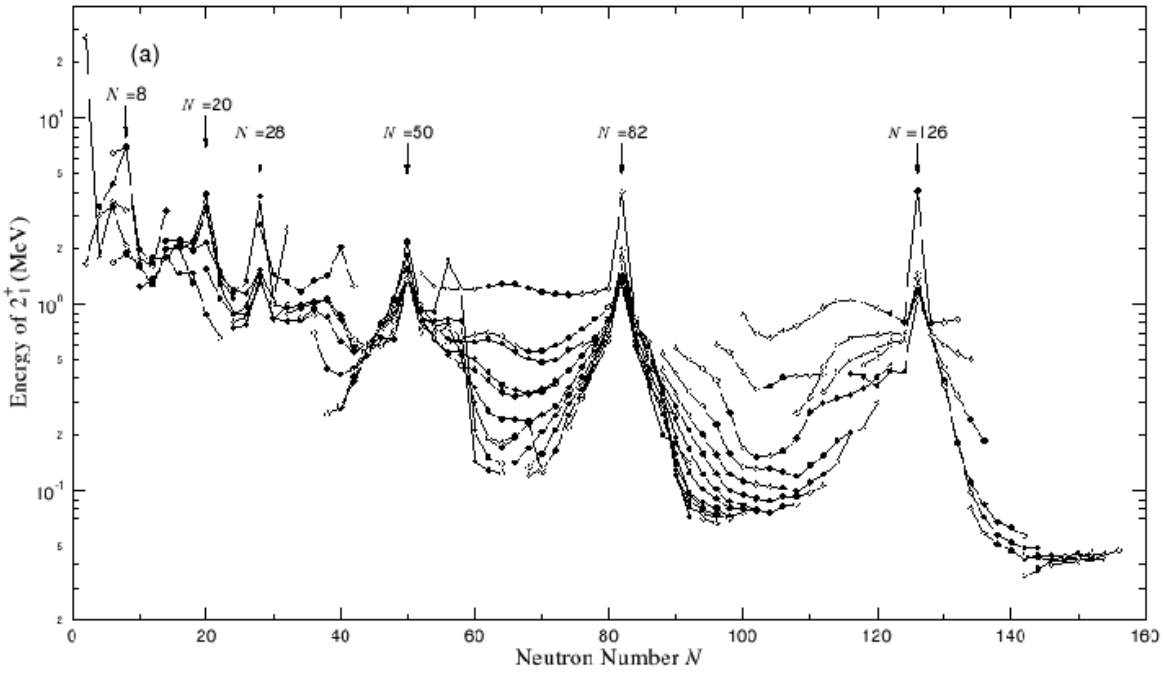

Figure 1.1: *A compilation of $E(2^+)$ with respect to number of neutrons in even-even nuclei. The isotopic chains are connected by lines. The $E(2^+)$ values are peaked for specific neutron numbers indicating an increased stability. (Extracted from [Rama 01])*

Another experimental value by which we can measure the stability of a nucleus is the reduced transition probability $B(E2 : 0^+ \rightarrow 2^+)$. The latter is a measure of the capacity of a nucleus to be excited into a 2^+ state. This value is plotted against the proton number

in figure 1.2. Regardless of the isotonic chain, we notice that the $B(E2)$ values are reduced considerably for nuclei having the same specific numbers as before, this time for protons.

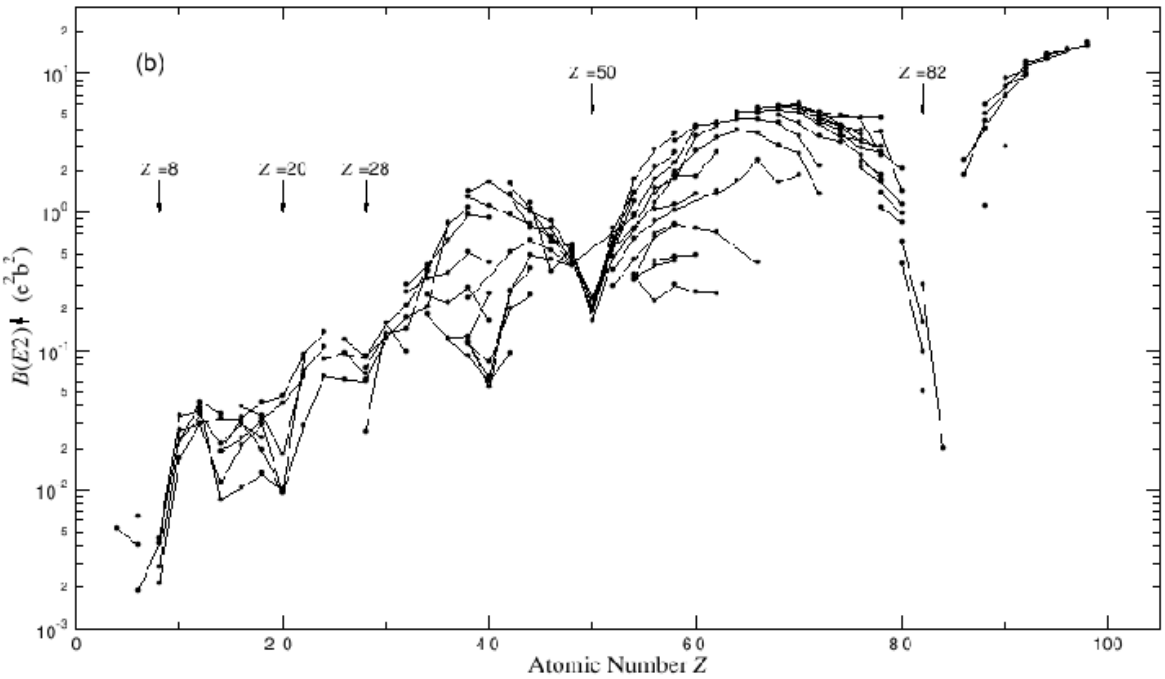

Figure 1.2: *A compilation of $B(E2)$ with respect to number of protons in even-even nuclei. The isotopic chains are connected by lines. The $B(E2)$ values are peaked for specific proton numbers indicating an increased stability. (Extracted from [Rama 01])*

Elsasser was the first to discover in 1933 [Elsa 34] the existence of these "special numbers", indicating their relation to the stability of nuclei. Nowadays, these numbers are found in the literature under the name "magic numbers" and are listed as

$$2, 8, 20, 28, 50, 82, 126$$

where the last magic number (*i.e.* 126) has been observed experimentally only in the case of neutrons (*cf.* figure 1.2).

Nuclear models were developped in an attempt to reproduce the magic numbers and understand how neutrons and protons within atomic nuclei are structured. It was well known in atomic physics that electron-binding energies undergo sharp changes just after a closed electron shell and atomic magic numbers were well established. Analogously, it was reasonable to suppose that in the nuclear case, these magic numbers correspond also to closed shells of nucleons. The problem then reduces to solving Schrödinger equation with the kinetic energy of each nucleon $t(i)$ and the *right* nuclear potential $U(\vec{r})$. Calculations of the energy levels using simple nuclear potentials (Square well, Harmonic oscillator (HO)) failed to reproduce the observed magic numbers. The correct prescription of the nuclear potential was found by Mayer [Goep 49] and independently by Haxel, Jensen, and Suess in the same year [Haxe 49] by adding "empirically" a strong spin-orbit coupling

term. The nuclear potential, which manages to reproduce the magic numbers, can be written as follows.

$$U(\vec{r}) = \frac{1}{2}mw^2\vec{r}^2 + D\vec{l}^2 - C\vec{l}\cdot\vec{s}. \tag{1.1}$$

The successful model, called the independent-particle model, assumes that nucleons are independent (no mutual interactions) and are confined by:

1. an isotropic harmonic oscillator ($\frac{1}{2}mw^2\vec{r}^2$),
2. a surface-correction[1] ($D\vec{l}^2$),
3. a strong attractive spin-orbit term ($C\vec{l}\cdot\vec{s}$).

Where $\vec{l}$, $\vec{s}$, C and D are the angular momentum, the intrinsic-spin and two coupling constants, respectively.

Figure 1.3 shows how the observed magic numbers are reproduced. Using a *HO* potential, the orbitals are degenerate in energy despite having different $\vec{l}$ and $\vec{s}$. The energy levels at this stage depend on the principal quantum number N (left hand side of figure 1.3). Adding a surface correction to the nuclear potential lifts the degeneracy of energy levels having same N but different orbital numbers $\vec{l}$. The resulting energy levels are shown in the center of the figure 1.3. Finally, adding a spin-orbit term to the potential splits further each orbit having $\vec{l} \neq \vec{0}$ into two levels characterised by a spin $j_- = l - s$ and $j_+ = l + s$ (right hand side of figure 1.3).

The energy separation of a spin-orbit doublet (*e.g.* $1f_{5/2} - 1f_{7/2}$) is proportional to the coupling ($\vec{l}\cdot\vec{s}$) thus it is greater for a greater angular momentum $\vec{l}$. The effect on the lower energy levels is rather weak as moderate l values are involved ($0 \leqslant l \leqslant 2$). This explains why the first *HO* gaps (*i.e.* having 2, 8 and 20 nucleons) are conserved and observed experimentally as nuclear magic numbers. On the contrary, the spin-orbit coupling-effect on the higher energy levels involving larger l values is much stronger. For instance, the lowering of the $1f_{7/2}$ orbital due to spin-orbit splitting in the $1f_{5/2} - 1f_{7/2}$ doublet creates a new gap after the filling of 28 nucleons. The same mechanism applies for the $1g_{7/2} - 1g_{9/2}$ doublet where the $1g_{9/2}$ becomes an intruder in the harmonic shell $N = 3$ and generates the magic number $N = 50$, washing-out the original *HO* magic number $N = 40$. A similar effect takes place for higher energy levels creating the $N = 82$ and $N = 126$ shell gaps.

[1] The surface correction is not needed if one uses a Woods-Saxon potential instead of a harmonic oscillator.

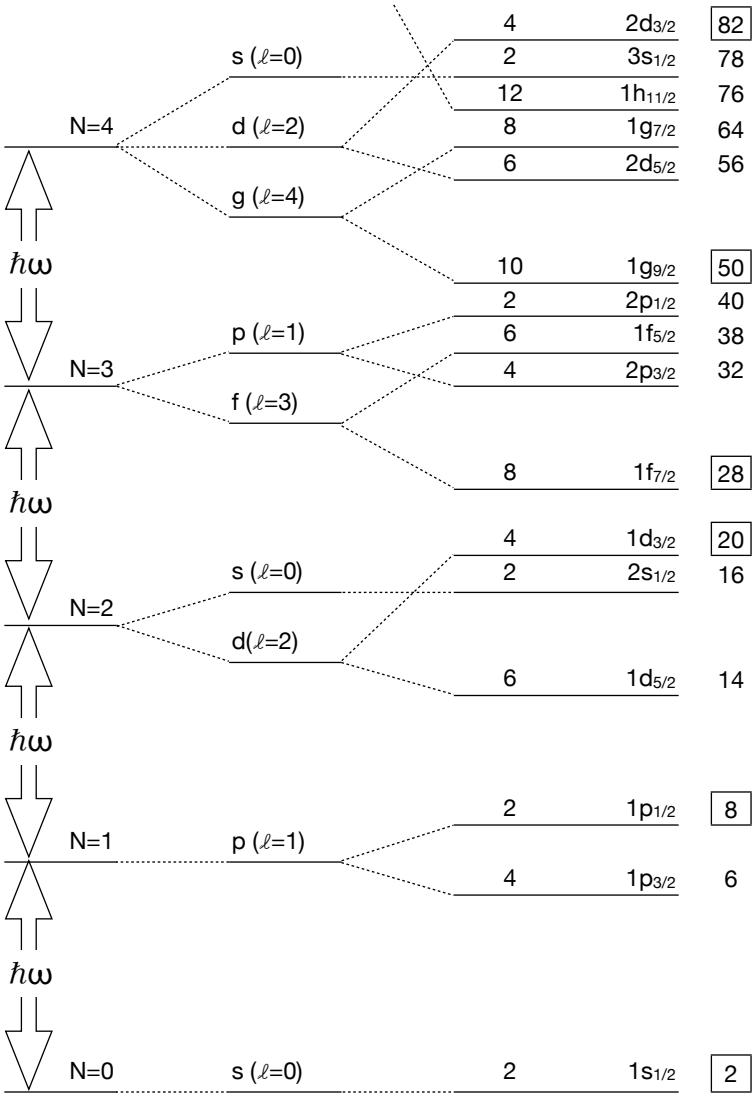

Figure 1.3: *On the left side the energy levels produced by the Harmonic oscillator. The intermediate structure corresponds to the adding of the surface correction. On the right side, shell structure according to nuclear shell model when adding the spin-orbit term to the nuclear potential. To the right of each level are shown the cumulative number of nucleons. The filling of each shell reproduce the magic numbers (inside a box).*

In addition to the explanation of the magic numbers, the major success of the nuclear independent shell-model was the prediction of the spin and parities of the ground states of most of the nuclei in the valley of stability. Even-even nuclei (even number of protons and neutrons) are characterized with $0\hbar$ ground-state spins and a positive parity $J^\pi = 0^+$. For nuclei with one nucleon outside a closed shell, or one nucleon vacancy (hole) in a closed shell, the nuclear ground-state spin and parity are determined by the extra nucleon or hole. Finally, the spin-parity of odd-odd nuclei are determined by the spin-coupling of the single proton and neutron.

1.2 Modern shell-model

1.2.1 Nucleus as an A-body problem and modern shell-model approach

For nuclei located further away from shell-closure, the independent-particle model diverges, and fails to reproduce the measured properties. It seems efficient only in the region limited to closed shells and their vicinity. This is related to some degrees of freedom which were neglected in the first model, most importantly the interaction between nucleons.

Assuming two-body interactions only, the nuclear Hamiltonian can be formally written as the sum of kinetic energy t_i and the potential energy between two nucleons V_{ik}, summed over all the nucleons:

$$H = \sum_{i=1}^{A} t_i + \frac{1}{2}\sum_{i=1}^{A}\sum_{k>i}^{A} V_{ik}(\vec{r_i} - \vec{r_k}) \tag{1.2}$$

A formal solution of this A-body problem would consist of :

1. finding an appropriate single-particle wavefunction basis to describe a nucleon in some state; $|\phi_i\rangle = a_i^\dagger|0\rangle$ where $a_i^\dagger$ is the creation operator of a nucleon on this state,
2. building an A-body wavefunction describing the nucleus with a Slater determinant using the single-particle basis $|\phi_\alpha\rangle = det(\prod_{i=1}^{A}\phi_i)$,
3. a physical state $|\Psi\rangle$, in this case, would be a linear combination of $|\phi_\alpha\rangle$; $|\Psi\rangle = \sum_\alpha C_\alpha|\phi_\alpha\rangle$,
4. and finally solving $H|\Psi\rangle = E|\Psi\rangle$ by diagonalizing the infinite matrice $\langle\Psi|H|\Psi'\rangle$.

The 2-nucleon interaction is known to be attractive having a range ~ 1 fm and very repulsive at very short distances reflecting the complexity of its nature. Nevertheless, the independent-particle model success in the region close to the valley of stability, shows that the bare nucleon-nucleon interaction can be regularized in the nuclear medium and an "effective" interaction can be found such that,

$$H\Psi = E\Psi \rightarrow H_{eff}\Psi_{eff} = E\Psi_{eff} \tag{1.3}$$

However, an exact solution of such a many-body problem can rarely be obtained, except for the lightest masses, and approximations are then used to solve the problem. The first step towards an approximate solution is to introduce a single-particle potential $U_i(\vec{r})$ and the expression can then be rearranged separating the Hamiltonian into two parts as follows,

$$H_{eff} = \underbrace{\sum_{i=1}^{A}(t_i + U_i(\vec{r}))}_{H_0} + \underbrace{\left[\sum_{i=1}^{A}\sum_{k>i}^{A} V_{ik}(\vec{r_i} - \vec{r_k}) - \sum_{i=1}^{A} U_i(\vec{r})\right]}_{H_{res}} = H_0 + H_{res} \tag{1.4}$$

The H_0 part describes an ensemble of independent particles moving in an effective average potential $\sum_{i=1}^{A} U_i(\vec{r})$. It represents the very notion of the mean field approach described earlier. Solving the Schrödinger equation only with this term will provide the aforementioned single-particle energies(*cf.* figure 1.3) and the "appropriate" single-particle wavefunction basis $|\phi_i\rangle$ to describe the nucleus. The remaining part H_{res}, corresponds to the residual interactions responsible of the detailed structure of the nucleus.

Under the second quantization formalism the Hamiltonian in equation 1.4 applied on a physical state $|\Psi\rangle$ becomes,

$$H_{eff}|\Psi\rangle = \sum_{i}^{A} \varepsilon_i a_i^\dagger a_i|\Psi\rangle + \sum_{ijkl} V_{ijkl}^{JT} \left[(a_i^\dagger a_j^\dagger)^{JT}(a_k a_l)^{JT}\right]^{00}|\Psi\rangle \tag{1.5}$$

- $a_i^\dagger$ a_i are operators creating or anhilating a particle in a generic state "i ",
- J and T represent the coupled angular momentum and isospin, respectively,
- $V_{ijkl}^{JT} = \langle\phi_i\phi_j(JT)|H_{res}|\phi_k\phi_l(JT)\rangle$, where $ijkl$ may be any of the orbitals occupied by the interacting nucleons.

Following the formal solution described in section 1.2.1, the final step after finding $|\phi_i\rangle$ and building the physical state $|\Psi\rangle$ would be to diagonalize the Hamiltonian matrix. Since the matrice is of infinite dimensions, it is more practical for diagonalization procedure, to divide the Hilbert space containing all the states of the nucleus into three parts (*cf.* figure 1.4):

1. an inert core consisting of orbitals that are forced to be always full,
2. a valence space containing the orbitals bearing the main part of the interaction between valence nucleons,
3. an external space representing all the remaining orbits that are always empty.

The diagonalization procedure is only done in the valence space. The valence space must contain the relevant degrees of freedom for a given problem as demanded by the effective interaction. The safer valence spaces for shell-model calculation are those comprised between magic closures. However, this is not a general rule and in some cases the inclusion of orbitals beyond the gap is required in order to understand shell-evolution, *e.g.* the "island of inversion" at $N = 20$ discussed later in section 1.3.

1.2.2 Realistic effective interaction

According to the work of M. Dufour and A. Zuker [Dufo 96] any effective interaction can be split into two parts,

$$H_{eff} = H_m(monopole) + H_M(multipole), \tag{1.6}$$

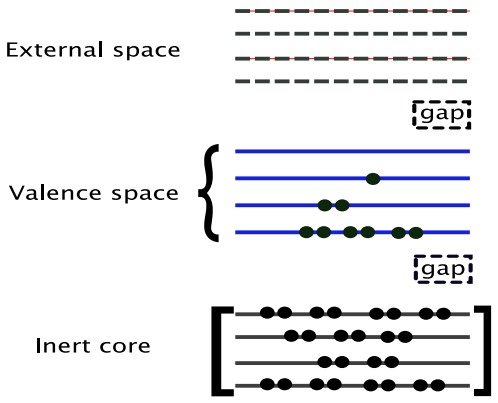

Figure 1.4: *Hilbert space scheme describing the nucleus. The Hilbert space is divided into three parts : Inert core, Valence space, External space. For more explanation see text..*

where H_m contains all the terms that are affected by spherical Hartree-Fock variation, and thus responsible for global saturation properties and spherical single-particle behaviour. The second term H_M contains pairing, quadrupole and higher multipole terms of the interaction.

For all realistic interactions the H_M part is correct [Abzo 91, Caur 94] unlike the H_m part that must be treated phenomenologically. For exemple, shell-model calculations derived from microscopic Nucleon-Nucleon (NN) forces fails to reproduce the anomalous behavior of the oxygen isotopes, where the last bound Oxygen (^{24}O) is particularly close to the stability valley compared to neighboring Nitrogen and Fluorine chains (^{24}N, ^{31}F). Recently, Otsuka *et al.* [Otsu 10] showed that taking into account microscopic three-nucleon forces explains naturally the Oxygen anomaly and demonstrated that 3N-forces are expected to play a crucial in shell-closures.

However, in the present shell-model approach the 3N-forces are not considered and NN-forces are corrected by phenomenological procedures in order to obtain a realistic **effective** interaction able to reproduce the observed phenomena and to compensate other degrees of freedom not taken into account. The correction is greatly simplified by the important relation between H_{eff} and H_m [Dufo 96]:

$$\langle CS \pm 1|H_{eff}|CS \pm 1\rangle = \langle CS \pm 1|H_m|CS \pm 1\rangle, \tag{1.7}$$

where $|CS \pm 1\rangle$ represents a nucleus having a closed shell plus or minus one nucleon. According to equation 1.7 the monopole part H_m is responsible for the evolution of the single-particle energies (SPE) inside the model space when applied to a nucleus of simple structure such as a *closed shell* and a *closed shell plus or minus 1 particle*. In other words, experimental values from nuclei having a simple structure are directly related to the monopole part of the Hamiltonian and can be used in phenomenological corrections of the total interaction.

The explicit form of H_m can be written as,

$$H_m = H_{sp} + \sum_{ij,\tau\tau'} \left(V_{ij}^{\tau\tau'} \frac{n_{i\tau}(n_j\tau' - \delta_{ij}\delta_{\tau\tau'})}{(1+\delta_{ij}\delta_{\tau\tau'})} \right), \tag{1.8}$$

where H_{sp} is the single-particle term generated by the core orbits and

$$V_{ij}^{\tau\tau'} = \frac{\sum_J V_{ijij}^{JT}[J]}{\sum_J [J]}, \tag{1.9}$$

with the sums over Pauli allowed values. J represents the coupled angular momentum and (τ, τ') stands for a (π,π), (ν,ν) or (π,ν) interaction. In other words, $V_{ij}^{\tau\tau'}$ is the average value of all two-body matrix elements (TBME) V_{ijij}^{JT} corresponding to the possible spin orientation J.

According to equation 1.8, the SPE of an orbital i is shifted by $V_{ij}^{\tau,\tau'}$ multiplied by the occupation number of the orbital j and i $(n_{i\tau}n_{j\tau})$. This leads to a change in the SPE and influences the evolution of shell-closures[2], in particular in neutron-rich nuclei.

1.3 Shell evolution at N=20

A vanishing of a shell-closure in the chart of nuclides has been found for the neutron magic number $N = 20$ [3]. It rises from the separation between $\nu 1d_{3/2}$ of the $sd-shell$ and $\nu 1f_{7/2}$ of the $pf-shell$ (see figure 1.3). One of the first experimental evidence was made in ^{32}Mg by Détraz *et al.* and Guillemaud-Mueller *et al.* [Detr 79, Guil 84] who found an unexpectedly low excitation energy of the first excited 2^+ state (0.885 MeV) compared to the neighbouring less neutron-rich isotones (see figure 1.5a).

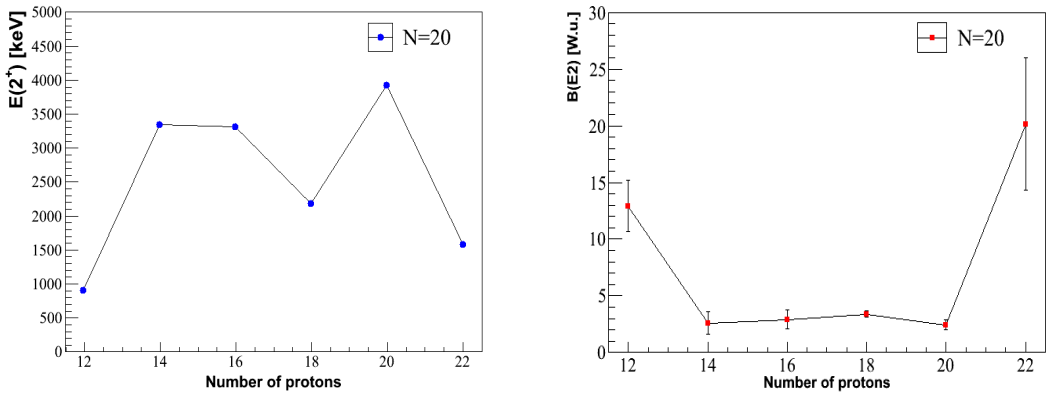

(a) **(b)**

Figure 1.5: *(a) $E(2^+)$ and (b) $B(E2)$ values for even-even $N = 20$ isotones. (Extracted from NNDC database [NNDC].)*

The $B(E2)$ value was measured later on using Coulomb excitation [Moto 95] and found to be equal to 14.9 W. u. (454 e^2fm^4), suggesting that ^{32}Mg is no longer spherical

[2] It is noteworthy to mention that small inaccuracies in the value of $V_{ij}^{\tau,\tau'}$ can produce large effects in shell-model calculations for the relative position of the orbitals due to the quadratic terms of the occupation numbers.

[3] The first indication of a vanishing shell-closure was spotted at $N = 8$.

but rather well deformed. Figure 1.5b shows the evolution of $B(E2)$ through the isotonic $N = 20$ chain from ^{42}Ti to ^{32}Mg. The $B(E2)$ value stays roughly constant between $Z = 20$ and $Z = 14$ meaning that the $N = 20$ gap remains quite strong after the removal of 6 protons successively from the $\pi d_{3/2}$ and $\pi s_{1/2}$, and increases suddenly by a factor of about 4 in ^{32}Mg, indicating a weakening of the magic gap $N = 20$ when additional protons are removed from the $\pi d_{5/2}$.

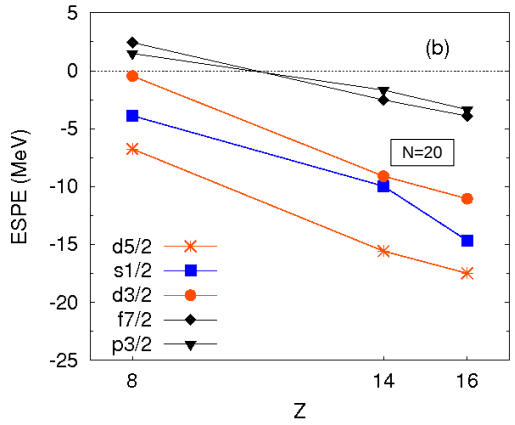

Figure 1.6: *Neutron effective single-particle energies at $N = 20$ versus the number of protons. The x-axis shows only the number of protons corresponding to the total filling of the levels $\pi 1p_{1/2}$ (8), $\pi 1d_{5/2}$ (14) and $\pi 2s_{1/2}$ (16). The details of the interaction used are found in reference [Lenz 10].*

The sudden increase of the $B(E2)$ indicates that neutrons are occupying not only the $sd-shells$ but also the $fp-shells$. Figure 1.6 shows the effective SPE for $N = 20$ taken from [Lenz 10], between $Z = 8$ and 16. A steep rise of the $d_{3/2}$ orbital from $Z = 14$ down to $Z = 8$ leads to a substantial reduction of the $N = 20$ gap.

This could be mainly attributed to the large value of the proton-neutron monopole interaction $V^{\pi\nu}_{d_{5/2}d_{3/2}}$, as pointed out by Otsuka *et al.* [Otsu 01], which weakens rapidly when protons are removed (see equation 1.8). The spherical $N = 20$ gap thus becomes not large enough to prevent the development of excitations and correlations in the intruder $fp-shell$ in ^{32}Mg, and its ground state is dominated by $2p-2h$ excitations[4]. The neutrons tend to occupy the intruder state due to the reduction of the $N = 20$ gap and the presence of quadrupole partners $1f_{7/2} - 2p_{3/2}$. The ^{32}Mg nucleus then belongs to the so-called *"island of inversion"* [Warb 90], where the intruder configurations are dominant in the ground state. This was already proposed by Zuker *et al.* [Zuke 95] that the minimum valence spaces able to develop quadrupole collectivity should contain at least a $(j, j-2..)$ sequence of orbits such as $1f_{7/2} - 2p_{3/2}$ at $N = 20$.

[4] A minimum of $2p-2h$ excitations is required to create a positive parity state across the $N = 20$ gap formed by orbits of different parities, *i.e.* sd and fp, positive and negative parity, respectively.

1.4 N=40 sub-shell

1.4.1 Magicity of ^{68}Ni

The doubly magic character of ^{68}Ni nucleus (closed $Z = 28$, $N = 40$) was suggested in the early 1980s [Lomb 83, Bern 82]. The $N = 40$ gap is the relic of the harmonic oscillator, washed out by the strong spin-orbit potential. It is formed between the $N = 3\hbar\omega$ and $N = 4\hbar\omega$ shells (see figure 1.3).

Medium-mass neutron-rich nuclei are expected to have a diffuse surface as compared to stable nuclei due to excess of neutrons. As a consequence, the derivative of the mean-field potential is thought to be weaker, which in turn reduces the spin-orbit surface term [Doba 94]. This leads to a restoring of the gap at $N = 40$ (and eventually a reduction of that at $N = 50$).

The first experimental evidence of the magic character of the $N = 40$ in ^{68}Ni was made by Broda *et al.* [Brod 95]. The structure of ^{68}Ni was probed by deep-inelastic reactions of ^{64}Ni on ^{130}Te creating the nucleus of interest. Inspection of $\gamma-\gamma$ coincidences revealed 3 states including a 2^+ state at 2033 keV. Figure 1.8a (in section 1.4.2) shows the evolution of the excitation energies of the first 2^+ states $E(2^+)$ for the even-even Ni isotopes. The $E(2^+)$ values are comprised between 1200 keV and 1400 keV for ^{58}Ni to ^{66}Ni and rises suddenly to 2033 keV for ^{68}Ni which suggests the existence of a significant subshell-closure at $N = 40$.

Another observable can be used to determine experimentally the more or less collective character of a nucleus, the quadrupole excitation probability $B(E2; 0^+ \rightarrow 2^+)$. Figure 1.8b shows the $B(E2)$ values for the even-even Ni chain. The low $B(E2)$ obtained for ^{68}Ni (3.2(7) W. u.) [Sorl 02] is even comparable to the cases of doubly magic nuclei such as ^{16}O (3.3(3) W. u.) or ^{40}Ca (2.3(4) W. u.) and reinforces the assumption on the magicity of $N = 40$ for ^{68}Ni.

The large 2^+ energy and small $B(E2)$ value for ^{68}Ni could be interpreted as a sign for a sub-shell-closure at $N = 40$, however, the separation energy of two neutrons (S_{2n}) does not show any evidence of such effect [Raha 07]. This could be explained by the fact that the neutron-fermi level lies between the $fp-shells$ of negative parity and the $1g_{9/2}$ of positive parity. The neutrons in the $fp-shells$ could cross the $N = 40$ "gap" only by pairs due to the conservation of parity. This could explain why ^{68}Ni shows at the same time high 2^+ energy and no sign of shell-closure in the neutron separation energy.

For example, the state at 2.848 MeV in ^{68}Ni is due to the excitation across the $N = 40$ gap of one neutron from the $2p_{1/2}$ orbital in the $1g_{9/2}$ orbital which explains its negative parity and its isomeric character (0.86(5) ms). The calculations reproduce well its excitation energy within ~ 70 keV. Experimental and theoretical value $B(E2)$ values shown by thin arrows on both schemes for the $2^+_1 \rightarrow 0^+_1$ transition compare fairly well. They are small which underlines the spherical character of ^{68}Ni.

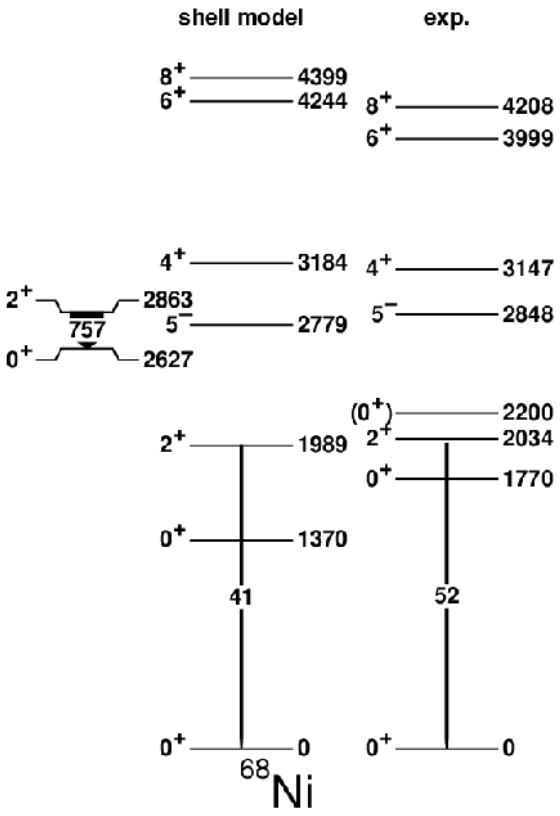

Figure 1.7: *Calculated level scheme of ^{68}Ni (left-hand side) compared to the experimental level scheme (right-hand side). The agreement is excellent. The experimental $B(E2) : 2_1^+ \rightarrow 0_1^+$ (expressed in $[e^2\mathrm{fm}^4]$) value is also well reproduced.*

Recently, a third 0^+ state associated to a $2p-2h$ exitation has been predicted at 2202 keV excitation energy in ^{68}Ni [Pauw 10]. Recently, ^{68}Ni has been populated in a multi-nucleon transfer reaction performed at GANIL with EXOGAM [Simp 00] and VAMOS [Pull 08]. An isomeric 0^+ state with a half-life of 216 ns [Dijo 11] has been established at 2200 keV excitation energy. It has been interpreted as the Pauwels's predicted $2p-2h$ state. Shell-model calculations involving four particle and hole excitations predict the excitence of a superdeformed 0^+ state at 2627 keV which could correspond to the state observed at 2200 keV. We can also notice a high $B(E2)$ value predicted for the $2_2^+ \rightarrow 0_3^+$ transition, not observed experimentally, inferring its well deformed character.

1.4.2 Onset of deformation in the $N \sim 40$ region

The structure of Fe and Cr nuclei, 2 and 4 protons below the $Z = 28$ shell-closure, respectively, gives a better understanding of this region where both chains were extensively investigated experimentally. The $E(2^+)$ systematics of the even-even $_{24}Cr$, $_{26}Fe$ and $_{28}Ni$ are shown in figure 1.8a. When approaching the $N = 40$ neutron number, the chains of Fe and Cr isotopes show a different behavior compared to the Ni isotopes. They both exhibit a drop in the excitation energy of their first 2^+ states starting at $N = 36$ and $N = 32$ in Fe and Cr, respectively. The deformation is stronger in the Cr chain where the $E(2^+)$ curve decreases slightly steeper compared to the one for Fe isotopes. The curves also indicate that the deformation increases with increasing neutron number, and the nuclei become progressively more collective.

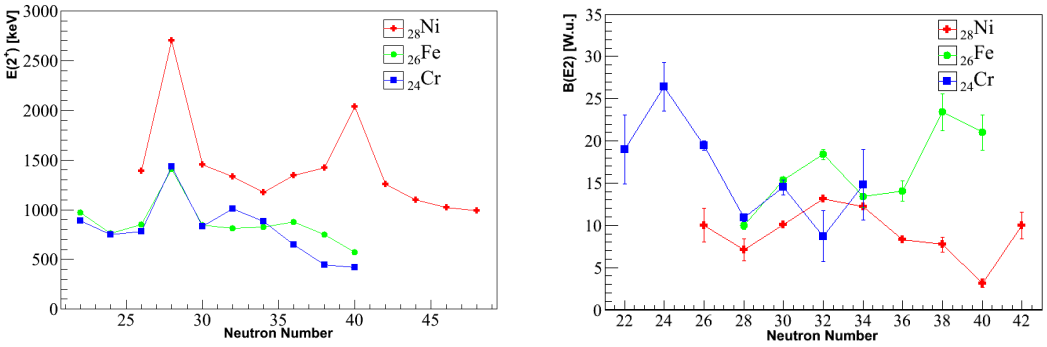

(a) (b)

Figure 1.8: *Evolution of the $E(2^+)$ (a) and $B(E2)$ (b) values of the even-even $_{24}Cr$, $_{26}Fe$ and $_{28}Ni$ chains. The sudden rise of the $E(2^+)$ value in ^{68}Ni compared to the neighbouring Ni isotopes suggests a magic character of the nucleus. Note the same signature for the doubly magic ^{56}Ni. On the left side, the lowest $B(E2)$ value is observed for ^{68}Ni. Unlike $_{28}Ni$, the $E(2^+)$ values of $_{24}Cr$ and $_{26}Fe$ chains exhibit an increasing deformation with increasing number of neutrons, this conclusion is strengthened by the known $B(E2)$ values for $_{28}Ni$ and $_{26}Fe$ isotopes.*

The same conclusion can be drawn by looking to $B(E2; 2^+ \rightarrow 0^+)$ values shown in figure 1.8b for the same isotopic chains. In the case of Fe, the $B(E2)$ values are roughly stable around 15W. u.($\approx$ 200 e^{2}fm^4) from $N = 32$ to $N = 36$. Adding 2 more neutrons induce a rapid increase of $B(E2)$ indicating an onset of large collectivity in these nuclei. For the Cr chain the value of $B(E2)$ at $N = 34$ is larger compared to the one at $N = 32$ indicating an onset of collectivity. However, due to the large error bars further measurements are needed to confirm this hypothesis.

These experimental results show clearly that the spherical neutron sub-shell-closure in ^{68}Ni is quickly washed out with removal of proton pairs. The sudden transition from the spherical ^{68}Ni to more proton deficient $N \approx 40$ isotones with deformed intruder configurations seems to have some similarity to the situation in the $N \approx 20$ "island of inversion". In both cases the developping quadrupole collectivity can be related to the occupation of neutron intruder orbitals from the next oscillator shell. Though the $N = 20$ shell gap is larger than the $N = 40$ one, the situation is similar if we replace the sequence of levels $1d_{3/2}$, $1f_{7/2}$ and $2p_{3/2}$ in $N = 20$ by $1f_{5/2}$, $1g_{9/2}$ and $2d_{5/2}$ in $N = 40$. Figure 1.9 shows a shell-model orbital scheme of the regions in question.

To understand further the onset of collectivity in neuron-rich Fe and Cr chains, large-scale shell-model calculations were performed in [Sorl 03, Ljun 10] in different valence neutron spaces comprising fp, $fp + g$ and $fp + gd$ orbitals in order to reproduce the experimental $B(E2)$ and $E(2+)$ values. In all references, only the space including the full $fp + gd$ model space was able to reproduce the low $E(2+)$ excitation energies measured in $^{60,62}Cr$ and $^{64,66}Fe$ demonstrating the major role played by the $2d_{5/2}$ neutron state in triggering the collectivity in these nuclei.

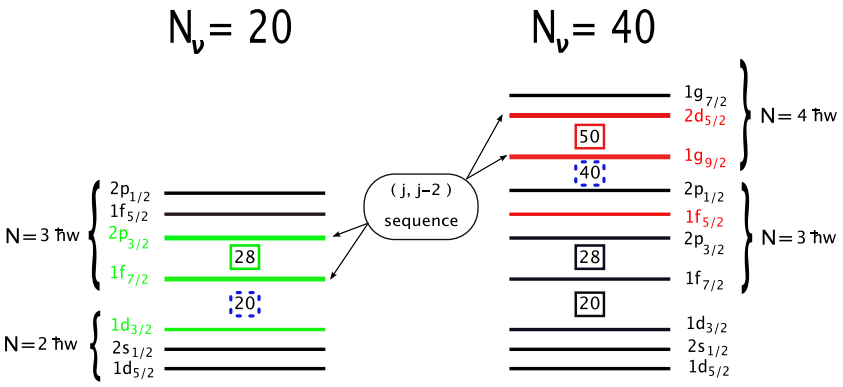

Figure 1.9: *Two shell-model structures showing levels $1d_{3/2}$-$1f_{7/2}$-$2p_{3/2}$ (left hand side in green) and $1f_{5/2}$-$1g_{9/2}$-$2d_{5/2}$ (right hand side in red). The levels corresponding to the j, $j-2$ sequence of orbitals are indicated with arrows in both cases. The similarity between the level sequences could be responsible of a new island of inversion at $N = 40$. For more details see text.*

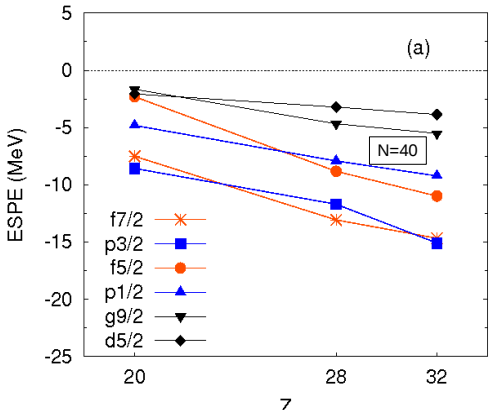

Figure 1.10: *Neutron effective single-particle energies at $N = 40$ versus the number of protons. The x-axis shows only the number of protons corresponding to the total filling of the levels $\pi 1d_{3/2}$ (20), $\pi 1f_{7/2}$ (28) and $\pi 2p_{3/2}$ (32). The details of the used interaction are found in reference [Lenz 10].*

The same conclusion could be derived from shell-model calculations performed recently by Lenzi et al. [Lenz 10]. The interaction used in Lenzi's calculation is used as a starting point of the shell-modell calculations performed for this work. The calculated effective SPE for the valence orbitals at $N = 40$ are shown in figure 1.10. It is noteworthy to mention also the large scale shell-model calculations done by Kaneko *et al.* [Kane 08] who managed to reproduce fairly well the $E(2^+)$ values of $^{60,62}Cr$ measured in [Sorl 03] without including the $2d_{5/2}$ orbit in their calculation.

In conclusion, excitation energy $E(2^+)$ and $B(E2)$ values exhibit a shell-closure behaviour in ^{68}Ni, while S_{2n} does not show such an effect. The HO closed shell at $N = 40$ in $^{68}_{28}Ni$ is weak and isolated and loses its strength in $^{64}_{24}Cr$ and $^{66}_{26}Fe$. Removing $\pi f_{7/2}$ protons from ^{68}Ni prompts the $\nu f_{5/2}$ orbit to move into the (small) $N = 40$ shell gap, so that $^{66,64}Fe$ and $^{60,62}Cr$ shows features of deformation. Calculations performed in this mass region predict a new island of inversion at $N = 40$ similar to the one discovered at $N = 20$. In all of these calculations the $2d_{5/2}$ orbital has been placed in a way to reproduce the experimental data and to enable the appearance of deformation in the region. However, the $2d_{5/2} - 1g_{9/2}$ energy gap for $N = 40$ in ^{68}Ni is not yet known. The main aim of this work is to determine this gap experimentally, which is essential to understand further the

nuclear structure around $N = 40$ and would help to draw preliminary conclusions about the magicity of ^{78}Ni. Depending on the scenario considered, the latter nucleus is lying on the r-process path of nucleosynthesis in supernovae explosion.

1.5 State of the art: ^{69}Ni

The experiment was proposed in order to locate the neutron orbital $2d_{5/2}$ relatively to the neutron orbital $1g_{9/2}$ in ^{69}Ni. The position of the neutron orbital $2d_{5/2}$ is very important in this mass region because it will directly provide the $N = 50$ gap in $^{69}_{29}Ni_{40}$. Since the discovery of ^{69}Ni nucleus [Dess 84] it has been studied by different experimental techniques and several states have already been observed up to 2700 keV. The level scheme in figure 1.11 summarizes the state of the art on the structure of ^{69}Ni before our experiment.

The $9/2^+$ ground state of ^{69}Ni nucleus results from the occupation of $\nu 1g_{9/2}$ by its single valence neutron. The ground-state decay was first investigated by [Bosc 88, Joki 97], it decays through β-emission into ^{69}Cu with a half-life of 11.2(9) s last measured by means of $\beta - \gamma$ spectroscopy [Fran 01].

The first experiment revealing the low lying excited states of ^{69}Ni was performed by R. Grzywacz *et al.* [Grzy 98] at GANIL. The study of ^{69}Ni was done on line after fragmentation of a $^{86}Kr^{34+}$ beam with an energy of 60.3 A MeV on a rotating ^{nat}Ni target 100 µm thick. ^{69}Ni nucleus was created in an isomeric state (2701 keV, $J^\pi = 17/2^-$) and has been studied by γ-spectroscopy in five high-purity germanium detectors. Its identification was confirmed by the known γ radiation from other Ni fragments. Several γ rays were attributed to ^{69}Ni and the associated energy levels and the proposed spins and parities are shown in figure 1.11.

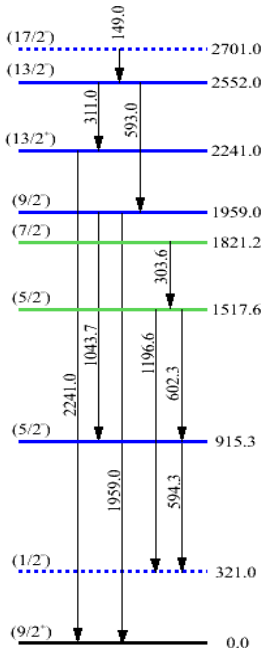

Figure 1.11: *The known energy levels in ^{69}Ni measured for the first time by γ-spectroscopy from isomeric decay (R. Grzywacz et al., blue lines) and β-decay of ^{69}Co (W.F. Mueller et al., green lines). Isomeric states are represented by dashed lines.*

The half-life of the $17/2^-$ isomeric state decaying to $13/2^-$ was found to be 0.439(3) µs. Another low-lying isomeric state was discovered at 321 keV with a suggested $1/2^-$ spin-parity and a half-life of 3.5(9) s [Fran 98, Pris 99]. The latter decays by the allowed Gamow-Teller β-emission feeding the low-lying $3/2^-$ states in ^{69}Cu as reported in [Pris 99, Muel 99].

W.F. Mueller *et al.* [Muel 99] studied ^{69}Ni by the β-decay of ^{69}Co produced at the

LISOL facility at the Louvain-la-Neuve cyclotron laboratory. ^{69}Co nuclei were produced in a proton induced fission reaction of ^{238}U and selected by both the mass spectrometer LISOL and the laser excitation set on Co resonance. γ rays were detected in two Ge detectors placed behind thin plastic scintillators for β detection. Two more energy levels with their spin-parity assignement were discovered in ^{69}Ni in this study (see green lines in figure 1.11).

Only allowed-β decays were observed in this experiment, starting from the negative-parity ^{69}Co ground state ($J^{\pi} = 7/2^{-}$). Hence no positive parity could be fed due to selection rules and the excited state of the single-particle energy corresponding to a single neutron on the $\nu 2d_{5/2}$ orbital has not been identified.

The structure of ^{69}Co consists of a single $1f_{7/2}$ proton hole and two $1g_{9/2}$ neutrons beyond the $N = 40$ subshell closure. Its β-decay into the ^{69}Ni is driven predominantly by allowed Gamow-Teller decay of an $1f_{5/2}$ core neutron to fill the proton hole in $1f_{7/2}$ leaving the daughter nucleus (^{69}Ni) with one-neutron hole and two neutrons in the $1f_{5/2}$ and $1g_{9/2}$ states, respectively. Based on this image, it is possible to understand the origin of the energy level at 915 keV as the coupling of a $1f_{5/2}$ hole to a core of ^{70}Ni ($\nu 1f_{5/2}^{-1} \otimes^{70} Ni(g.s.)$). The origin of the $1/2^{-}$ isomeric state at 321 keV is attributed to the $\nu 2p_{1/2}^{-1} \otimes^{70} Ni(g.s.)$ configuration.

Above 1500 keV, the principal configuration of energy levels could be explained by the coupling of a neutron hole in the fp-shell to an excited core of ^{70}Ni (*e.g.* the $5/2^{-}$ level at 1517.6 keV could be identified as $\nu 2p_{1/2}^{-1} \otimes^{70} Ni(2^{+})$). In general all the negative parity states in ^{69}Ni can be interpreted as the coupling of a hole to a ^{70}Ni core. The $13/2^{+}$ is the only state with positive parity observed at 2241 keV and is possibly rising from a neutron in the $\nu 1g_{9/2}$ state coupled to ^{68}Ni core in its 2^{+} excited state which lyies at a close energy (2033 keV) as mentionned earlier in section 1.4.1.

The half-lives of $5/2^{-}$ and $13/2^{-}$ levels at 915 and 2552 keV de-exciting by 594 keV and 593 keV γ-rays, respectively, were measured by Mach *et al.* [Mach 03] by means of the Advanced Time-Delayed $\gamma\gamma(t)$ method. Measurements were performed using an array of four small $BaF2$ detectors at the LISE spectrometer in GANIL following the fragmentation on a ^{9}Be target of a ^{76}Ge primary beam at 60 MeV/u. The reported half-lives ($B(E2)$) values are given as 0.120(34) ns (3.8(11) W.u.) and 0.519(24) ns (0.63(3) W.u.) for the energy levels at $5/2^{-}$ and $13/2^{-}$, respectively. The measured half-lives range (0.1 to 1 ns) is a strong indication of the $E2$ nature of the transition and thus strengthens the related spin-parity assignements first proposed in [Grzy 98].

Transfering a neutron into ^{68}Ni will select naturally the single-particle energies of ^{69}Ni. Figure 1.12 shows an heuristic shell-model of the $^{68}Ni + neutron$. ^{69}Ni nucleus could be created in its ground state which, in this simple picture, corresponds to the occupation of the $\nu 1g_{9/2}$ orbital ($l = 4$) by the valence neutron or in an excited state *e.g.* the $\nu 2d_{5/2}$ ($l = 2$) orbital we are searching for. Measuring the excitation energies of the populated 5/2+ states, in one neutron transfer reaction, allows to obtain the information on the fragmentation of the $2d_{5/2}$ orbital and its effective single-particle energy.

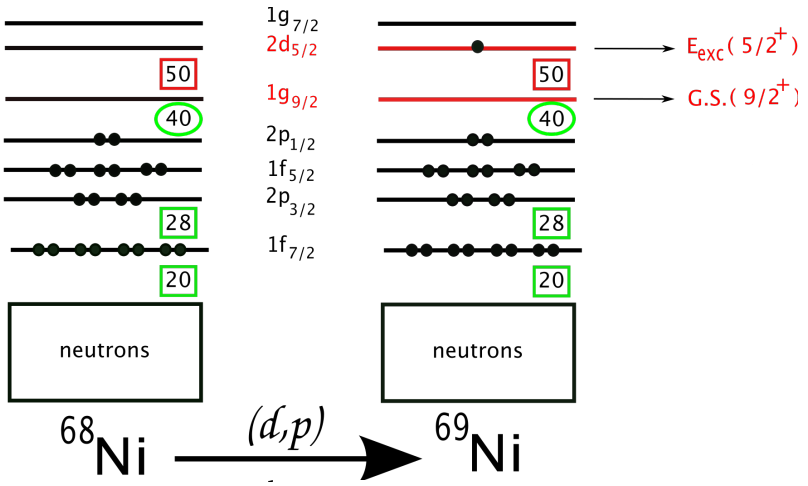

Figure 1.12: *On the left hand side a shell-model of the ^{68}Ni. A (d,p) reaction on ^{68}Ni transfers a neutron to its empty orbitals and infers the single-particle structure of ^{69}Ni nucleus (right hand side).*

1.6 Probing nuclear structure with nuclear reactions

Nuclear reactions are found in a wide variety going from compound nucleus formation to direct reactions passing by what is called "intermediate processes". The type of information available from reaction measurements depends on the nature and energy of the projectile and target nuclei.

In the compound nucleus reactions (see figure 1.13) the projectile and the target nuclei coalesce to form an excited compound system. The resulting nuclear system stays together sufficiently long ($\gg 10^{-22}$ s) for its excitation energy to be shared more or less uniformly by all its constituent nucleons. If enough energy is carried by one particle or a group of nucleons, the compound nucleus decays by emitting this particle. Otherwise, it undergoes de-excitation by β or γ-decay. The reaction can be written as

$$A + a \rightarrow C^* \rightarrow B^* + b. \tag{1.10}$$

Because of the delay between formation and decay, the compound nucleus is usually said to have lost memory of the input channel nuclei by which it was formed. In this case available information about the nuclear structure from this type of reaction will be closely related to the compound system it self. In direct reactions processes the projectile makes a peripheral contact with the target and immediatly separates *e.g.* elastic/inelastic scattering or transfer reactions shown in figure 1.14. In this type of reactions the system processes directly or within a few steps from initial to final states without forming an intermediate compound nucleus. In contrast with the compound-nucleus formation, the simplicity of direct reactions ensures that the target nucleus is only slightly rearranged to form the residual nucleus and their nuclear structures are similar. The duration required to complete a direct reaction is $\leq 10^{-22}$ s leaving no time for appreciable transfer of energy and thus exciting preferentially the low-lying states of the residual nucleus. For these reasons direct reaction are suitable tools to probe low-energy nuclear structures.

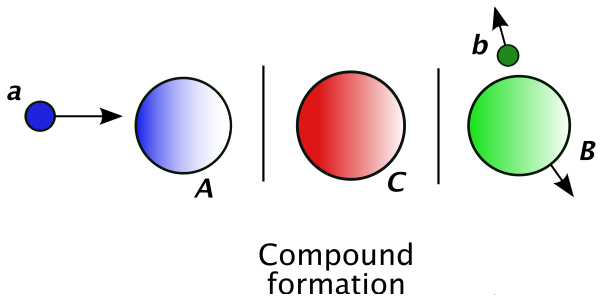

Figure 1.13: *A schematic illustration of compound-nucleus formation followed by a decay of light particles.*

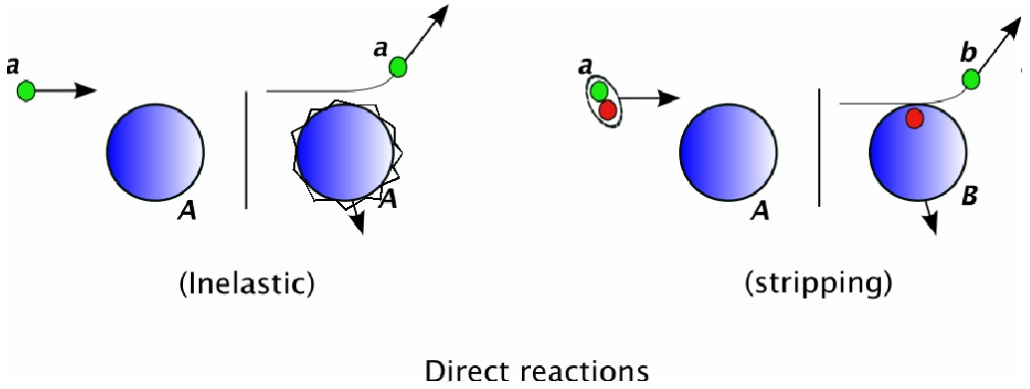

Figure 1.14: *A schematic illustration of two types of direct reactions, inelastic reaction (on the left-hand side) and stripping of one nucleon (on the right-hand side).*

The (d, p) stripping reaction has long been used as a mean of probing the single-particle structure of nuclei providing detailed information on neutron SPE. In particular, through Distorted-Wave Born Approximation analyses it has been used to determine the orbital angular momentum and spectroscopic factors of specific states in the heavy residue.

With the advent of beams of exotic nuclei there has been a renewed interest for charged-particle spectroscopy and especially for the (d, p) stripping reaction used to investigate the structure of neutron-rich nuclei via reactions in inverse kinematics.

Chapter 2

Experimental setup

In this chapter we will introduce the experimental setup used to study the inverse kinematics $d(^{68}Ni, p)$ reaction. The experimental method will be detailed, along with the experimental constraints. This study will be followed by a description of the beam production and the detector setup used during the analysis.

2.1 Experimental method and associated constraints

The structure of the ^{69}Ni nucleus was probed using the stripping reaction $d(^{68}Ni, p)$ in which a neutron is transferred to the ^{68}Ni nucleus to create the nucleus of interest. The transfered neutron will tend to populate single-particle states in ^{69}Ni. According to shell-model calculations the $2d_{5/2}$ neutron state lies in the energy range 1 to 3 MeV, accessible by the reaction chosen.

Knowing the kinematical characteristics of three of the four particules involved in a two-body reaction, the characteristics of the last particle are deduced by using the conservation laws. In this experiment we have measured the kinetic energy and the position of the proton[1]. The excitation energy of the ^{69}Ni was then calculated using the "missing mass" method explained in the next chapter.

Since ^{68}Ni is radioactive (half-life = 29 s), the reaction is studied in inverse kinematics where the heavy particle, that is the ^{68}Ni nucleus, is accelerated and impinges on a deuteron target. The kinematics of this reaction is depicted in figure 2.1. Unlike direct kinematics, the light particle moves in the opposite direction with respect to the motion of the Center of Mass system (CM) in the laboratory. It follows that the interesting forward CM angles of the proton corresponds to the backward angles in the laboratory system.

The calculated kinematical lines for $d(^{68}Ni, p)^{69}Ni$ show clearly that a rather good resolution on the measured energy is required in the most backward angles ($\theta_{lab} \geq 150°$) in order to distinguish low-lying excitation energies in ^{69}Ni. On the contrary, the resolution on energy becomes less demanding for decreasing angles. In this range it is the resolution on the measured angle that is most important.

For illustration, the figure 2.2 shows the absolute value of the error done in the calculation of the excitation energy (ΔE_{exc}) for an erroneous estimation of the measured energy

[1] The kinematic characteristics of the particles in the entrance channel are known from the beam tracker detectors.

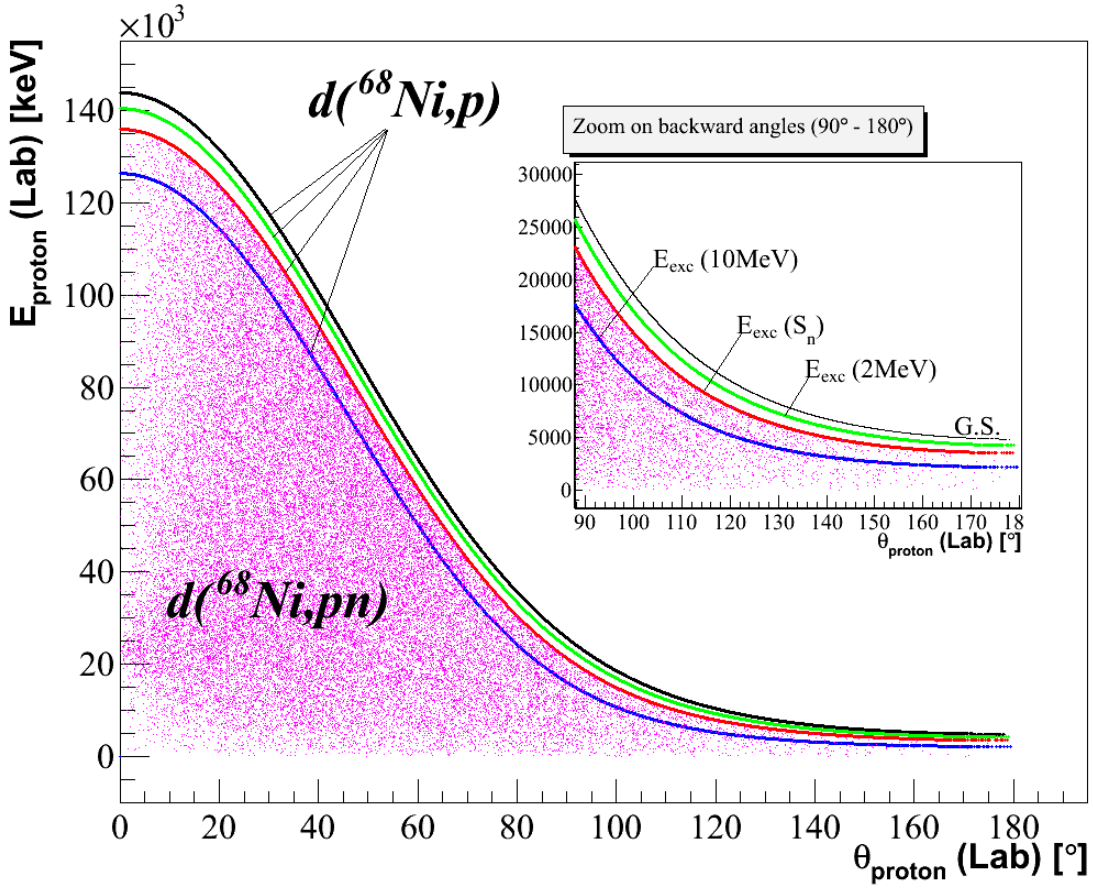

Figure 2.1: *The kinematics of the $d(^{68}Ni,p)^{69}Ni$ reaction for several excited energies. the deuteron break-up $d(^{68}Ni,pn)$ is represented in purple. The insert depicts the same spectrum zoomed on the backward angles.*

of the proton or its angle of emission. ΔE_{exc} reaches 200 keV when an error on the proton energy attains $\Delta E_p = 60$ keV and 400 keV for errors on angle up to $\Delta\theta_p = 0.6°$. It is noteworthy to mention that ΔE_p and $\Delta\theta_p$ are close to the energy and angular resolution of our detection system.

The errors related to the use of Rare Isotopes Beams (RIB) are due to their large emittance, broad energy spread, and low intensities. The latter is partially compensated by the use of relatively thick targets. The large emittance of the beam convoluted with the angular-straggling of the light charged particle in the target affects seriously the measurement of its angle of emission.

As a consequence, the use of beam tracking detectors is mandatory. The beam tracking detectors will provide, event by event, the direction and the hit location on the target of the beam-particle. Low pressure Multi Wire Proportional Chambers (MWPC) are a suitable solution due to their minor effect on the energy and incident angle of the detected particle. In our case we have used the CATS detectors (Chambre à Trajectoire de Saclay) [Otti 99]. Light-charged particle detectors with a high granularity will provide the hit position of

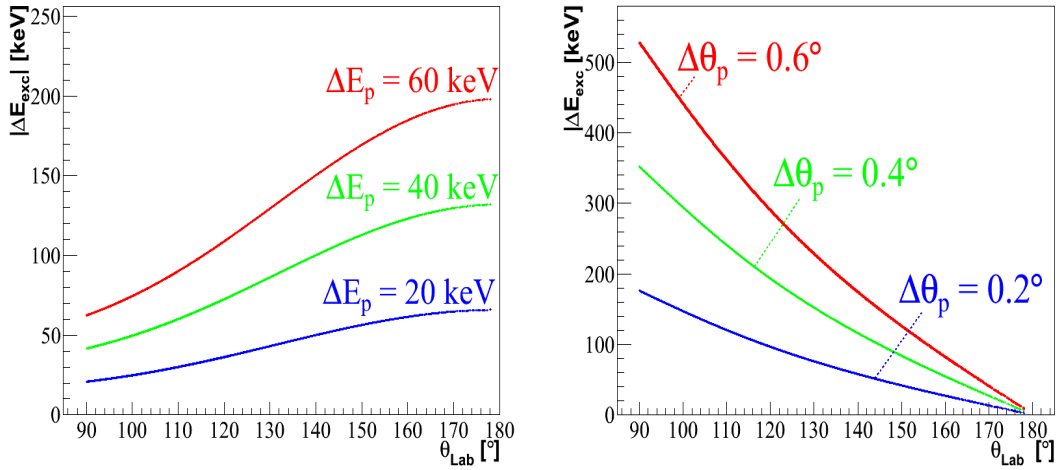

(a) $E_{exc} = f(\theta_p, \Delta E_p)$ **(b)** $E_{exc} = f(\theta_p, \Delta\theta_p)$

Figure 2.2: *Energy shift on calculated excitation energy as a function of a shift in the recoil proton energy (left) and angle of emission (right) for the* $d(^{68}Ni, p)$ *reaction at* 25.14 MeV/u. *Red, Green and blue graphs correspond to a fixed error of* 60, 40 *and* 20 keV, *respectively on the proton energy in the left panel, and to a fixed error of* 0.6°, 0.4° *and* 0.2°, *respectively on the proton angle of emission* θ *in the right panel.*

the light emitted particle with a relatively high precision. For this task we have used the MUST2 array [Poll 05]. Both detectors are presented further in this chapter. For the most backward angles ranging between 155° and 170° we have used another light-charged particle detector with an annular geometry, called S1, which presents a rather equivalent energy resolution but a worsen angular resolution as compared to the MUST2 array. As mentioned above, the excitation energy resolution is dominated by the recoil-particle energy resolution at the most backward angles.

The beam contaminants and the target material, lead to parasitic reactions that may interfere in the final excitation-energy spectrum. The presence of other nuclei in the beam may induce the same transfer reaction leading to protons in backward angles. The carbon in CD_2 target would also induce reactions leading to protons in the backward angles that could contaminate the ^{69}Ni excitation-energy spectrum.

These contaminations can be significantly reduced by requiring a coincidence with the heavy particle from the two-body reaction. Our heavy-residue detectors (an ionization chamber coupled with a plastic scintillator) were placed at the end of the beam line as shown in figure 2.3.

2.2 Beam production

The Ganil facility (*cf.* figure 2.4) delivers a wide spectrum of high-intensity ion beams ranging from ^{12}C to ^{238}U and accelerated up to 95 MeV/u and 7.8 MeV/u, respectively.

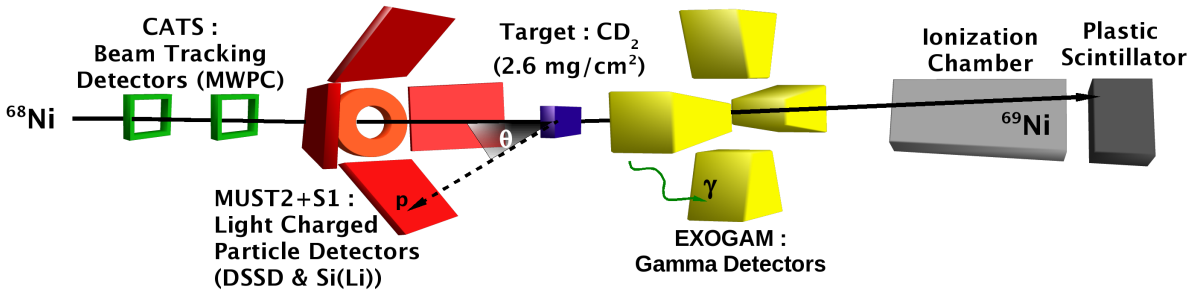

Figure 2.3: *An exploded view for the full experimental setup used in the whole experimental campaign showing respectively from left to right, two beam trackers (CATS), a set of light-charged particle detectors (MUST2 and the annular DSSD), a CD_2 target, four γ-ray detectors (EXOGAM clovers), an ionisation chamber and a plastic scintillator. The proton emission angle is calculated event by event, between the incident-ion trajectory and the proton trajectory as shown in the drawing. The reaction $d(^{68}Ni, p)^{69}Ni$ can be selected.*

GANIL uses two methods to produce RIB.

Isotope separation On Line (ISOL): In this method a primary beam (formed of light or heavy ions) impinges on a high-temperature thick target, producing radioactive and stable species via spallation, fission, or fragmentation reactions of the projectile. The products are stopped and neutralized inside the target due to its thickness. Under the form of neutral atoms, the radioactive products diffuse in the crystalline structure of the target impelled by its high temperature ($\approx 2000°$). Then, they are transferred to an ion source in order to be ionised, extracted and selected by a mass separator. After selection, the produced beam can be directly used for low-energy experiments or post-accelerated to the required energies. The resulting beams are ion-optically (emittance, energy resolution, timing structure) of excellent quality but the production and selection processes and the eventual re-ionization in the ion source can be slow and even inefficient leading to severe losses for short-lived nuclei or for isotopes from refractory elements. This is why ISOL technique are mainly used to produce relatively long-lived isotopes (ms to several s), with energies hardly exceeding 25 MeV/u at SPIRAL[2] in GANIL.

In-Flight separation: In this method the radioactive isotopes are produced by projectile fragmentation or in-flight fission on a relatively thin target. The reaction products, endowed with a velocity close to that of the primary beam, recoil out of the target and form the secondary beam. The beam lines using this technique are generally followed by a magnetic spectrometer in order to separate the nuclei of interest from the many other secondary produced fragments. The combination of a magnetic field and energy loss in wedges placed in the beam trajectory enables to extract the nucleus of interest from the fragment cocktail. The in-flight separation method can be applied to the production of all kinds of unstable nuclei independent of their chemical nature. Furthermore a short

[2] **S**ystème de **P**roduction d'**I**ons **R**adioactifs **A**ccélérés en **L**igne.

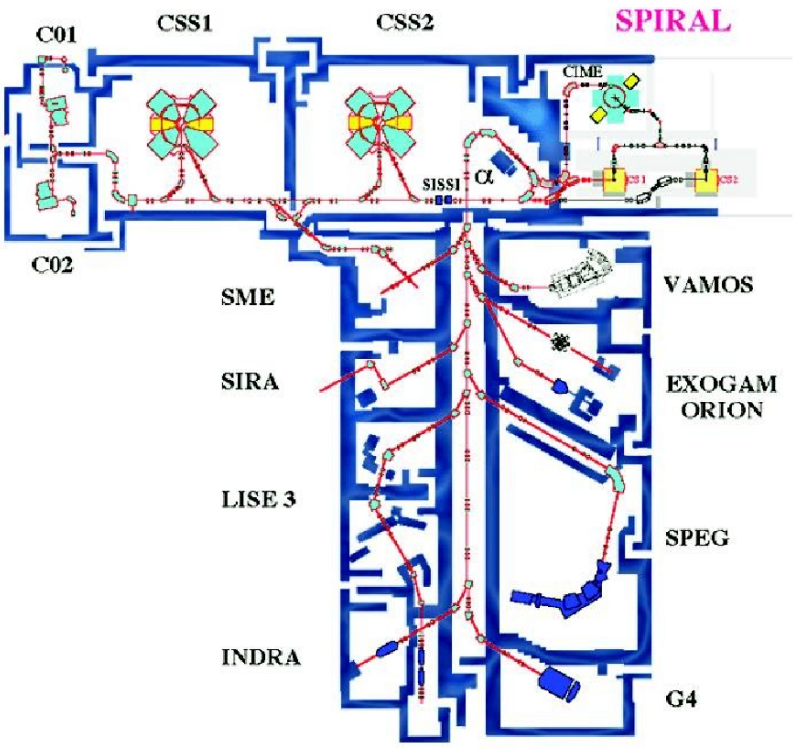

Figure 2.4: *GANIL facility and its different installations.*

transit time of the beam through the separator (in the order of 100 ns) puts very low limit on the half-life of unstable nuclei to be studied. Finally, the cross-section of fragmentation reactions are relatively high, allowing the production of RIBs very far from stability with intensities up to 10^4 pps.

In our experiment, we have used the LISE [Anne 92] (*cf.* 2.5) line to produce the ^{68}Ni secondary beam. The ^{68}Ni were produced at an energy of 25.14 MeV/u using the In-Flight separation technique with a good purity of $\approx$ 85.8%. A primary beam of neutron-rich ^{70}Zn at an energy of 62.5 MeV/u was fragmented on a production target made out of Be and located in the target-box of D3 area[3]. Its thickness was 505 µm at 0°. The ^{70}Zn fragmentation produced a cocktail of nuclei that has been filtered along the LISE spectrometer in order to select the nuclei of interest, ^{68}Ni. The selection in LISE is briefly described in the following paragraph.

When the secondary beam passes through the dipole $D1$ its constituents will sense the magnetic field B and will deviate under the influence of a force F,

$$F = QvB = \frac{mv^2}{\rho} \tag{2.1}$$

where Q, v and m are the charge state, the velocity and the mass of the beam particle,

[3]Due to the large primary beam current, a rotating target is used. Its orientation relative to the beam axis is variable in order to modify its effective thickness for the fine tuning of the secondary beam production.

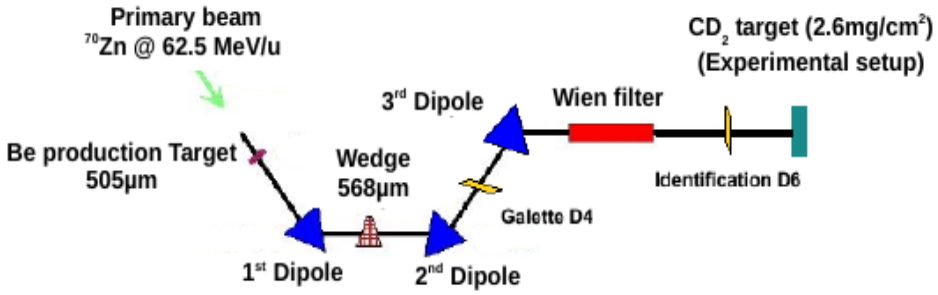

Figure 2.5: *The LISE magnetic spectrometer.*

respectively, and ρ is the radius of the trajectory of the particles. Equation 2.1 leads to,

$$B\rho \propto \frac{mv}{Q} \tag{2.2}$$

which means that by selecting a given magnetic rigidity $B\rho$, we select ions with same ratio mv/Q. To increase further the particle selection, a triangular wedge inserted between dipoles $D1$ and $D2$, intercepts the ions trajectory. The ions, according to Bethe-Bloch formula, will undergo an energy loss,

$$\delta E \propto \frac{Q^2}{v^2} \tag{2.3}$$

The energy E of the ions will then decrease proportionally to $\frac{m^3}{Q^2}$ since

$$\frac{\delta E}{E} \propto \frac{Q^2}{mv^4} \propto \frac{m^3}{Q^2} \tag{2.4}$$

By reducing the $B\rho$ of the second dipole $D2$, we only select ions having the ratio m^3/Q^2.

Assuming that the ions of atomic mass A are totally ionized ($Q = Z$), the selection in terms of m and Q reduces to a selection in terms of A and Z, the characteristics of a specific ion of interest.

Finally, a third selection can be performed, this time on the velocity of the particles, by using a Wien filter. In a Wien filter the ions are exposed to an electric field E perpendicular to a magnetic field B, both perpendicular to the ion trajectory. The corresponding forces will tend to deviate the ions away from the theoretical beam line unless the forces are exactly the same. In this case the selected velocity will be $v = E/B$ since

$$F_e = F_m \Rightarrow QE = QvB \Rightarrow E = vB \tag{2.5}$$

By adjusting the bias voltage of this filter, the ratio E/B is controlled as well as the transmitted velocity inside D6 where the experimental setup is located. The parameters of LISE are shown in table 2.1.

Primary beam	^{70}Zn
Energy	62.5 A MeV
Production target	^{9}Be, 505 µm, 0°
$B\rho_1$	2.5587 Tm
Wedge	^{9}Be, 1099 µm
$B\rho_2$	1.7641 Tm
Wien filter voltage	1 kV
Primary beam intensity	1.5 µA e
Secondary beam intensity	$8 \cdot 10^4$ pps

Table 2.1: *LISE general parameters, and primary and secondary beam intensities during the experiment.*

2.3 Targets

The choice of a target material depends on the reaction used and the chemical expertise to prepare the material. In order to perform a stripping reaction in inverse kinematics, we have used two deuterated Polyethylene (CD_2) targets of different thicknesses prepared by the "Service des cibles" at the Institut de Physique Nucléaire à Orsay, France (IPNO) from (CD_2) powder[4] of purity 98%.

The thickness of a target will influence significantly the light-charged particles in the backward angles in our case. Thick targets will increase energy and angular straggling leading to a poor resolution on the calculated excitation energy. On the contrary, a very thin target would not produce the needed statistics. The effect of target thickness on the energy resolution is estimated by Monte-Carlo simulation. This information is of great importance in the analysis of the excitation energy spectrum.

In order to study the excited states of ^{69}Ni a good compromise of target thickness is 2 mg/cm^2. During the analysis of the experiment, the target thickness was measured [Giro 11] at IPN-Orsay and was found to be 2.6 ± 0.1 mg/cm^2. Since the beam will also induce reactions on the carbon, a 2 mg/cm^2 target of pure carbon was used to estimate the background reactions generated by the carbon in the (CD_2) target during the experiment. Finally a thick 30 mg/cm^2 CD_2 target was used at the end of the experiment dedicated to γ-spectroscopy in the Germanium detectors.

All the targets were inserted in large size frames (3 cm $\times$ 3 cm) and mounted on the TIARA [Catf 03] target changer shown in figure 2.3. The changer consists in a wheel capable of supporting four targets. The changing of the target is done by remote-control from the acquisition room.

[4]Product of Cambridge Isotope Laboratories, USA.

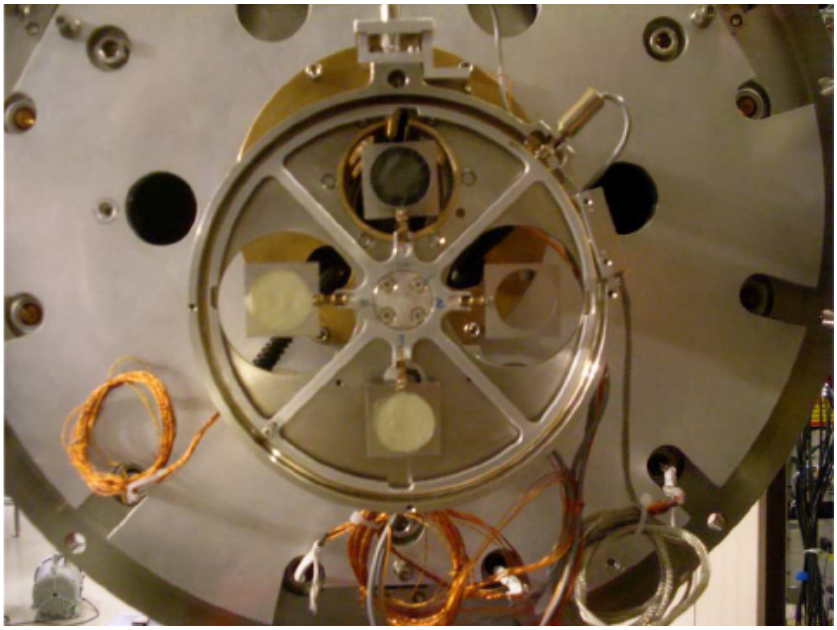

Figure 2.6: *TIARA Target changer consisting of a wheel capable of supporting four different targets. When a target is selected, a mechanical arm holds it and moves it to a defined position.*

2.4 CATS : the beam tracker detector

In order to reconstruct the impact position on the CD_2 target and the angle of incidence of the beam particles, two beam tracker detectors (CATS) were placed upstream at 92.6 and 52.6 cm to the reaction target. Each detector was placed in separated compartment provided by the "Laboratoire de Physique Corpusculaire de CAEN" (LPC-Caen, France) where the detector can be slid in and out from the beam line. Tracking detectors must provide a high-detection efficiency, without disturbing the projectile trajectory, and a good timing resolution. The CATS detectors fulfill these constraints and can be used for beams with rather modest intensities up to a few 10^5 particules per second (pps).

2.4.1 Description

The active area of a CATS detector is $70 * 70$ mm^2 (see figure 2.7). This detector consists of an anode plane of goldened tungsten wires sandwiched between two perpendicularly segmented cathode planes. The anode plane contains 71 wires of diameter 10 µm all parallel with 1 mm pitch. The cathode planes consist of 28 goldened aluminum strips, of 2000 Å thickness, evaporated on a 0.9 µm Mylar foil, and having a width of 2.34 mm each. The cathode pitch is 2.54 mm taking into account an interstrip of 0.2 mm. The distance between the anode plane and each cathode plane is 3.2 mm, forming two chambers around the anode plane filled with pure isobutane (C_4H_{10}) at a pressure of 8 mbar. Another 1.5 µm Mylar window is added on each side of the detector protecting the cathodes. Finally the operating positive voltage of the anode was set to 560 V with respect to the

cathodes connected to the ground potential.

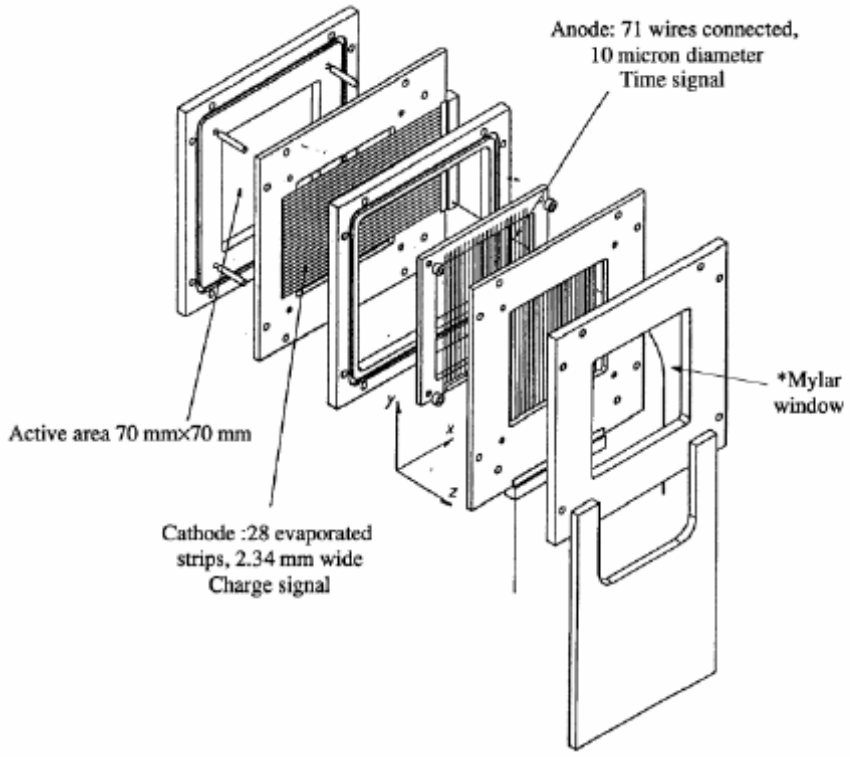

Figure 2.7: *Exploded view of a CATS detector*

2.4.2 Operating principle

A charged particle traversing the CATS detector ionizes the filling-gaz forming electron-ion pairs. Because of the potential difference between the cathode strips and the anode wires the electron travels towards the wires along the electric field line (see figure 2.8) gaining enough energy to ionise further gas molecules. Near the wires the field intensity is greater and the acceleration of electrons increases, leading to an avalanche of electron-ion pairs. The fast induced signal of electrons on the anode wires serves as a time reference, while the slower induced signal on both cathode planes, due mostly to the positive ion drift, is used for position-sensing. In general, several cathode strips sense the passage of an ion, which forms a hit pattern. The centroid of this hit pattern coincides with the ion passing-position.

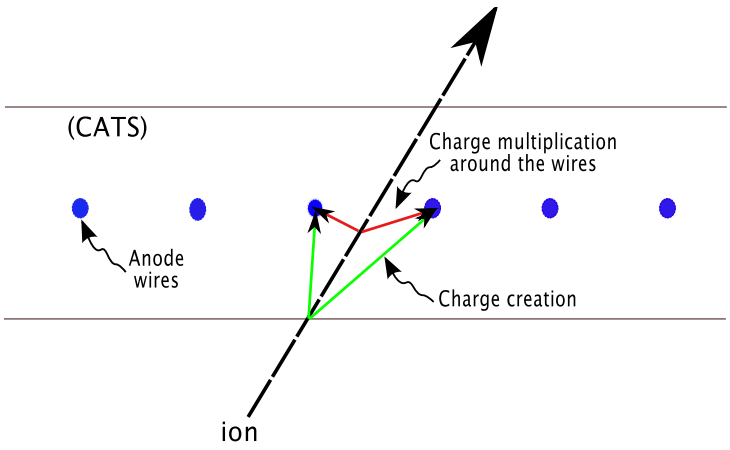

Figure 2.8: *Representation of charge multiplication in a Multi Wire Proportional Chamber.*

2.5 Light charged particle detectors

2.5.1 S1 Description

The detector described in this section will be refered to as S1, the design number of its producer Micron Semiconductor [Micr 10]. S1 is a DSSD with annular geometry providing position, energy and time information for light charged particules. It has an active surface of 53 cm^2 and a thickness of approximately 500 µm, insuring a dynamic range of 8 MeV for protons. The inner and outer diameters of the active area are 48 mm and 96 mm, respectively. The detector is depicted in figure 2.9.

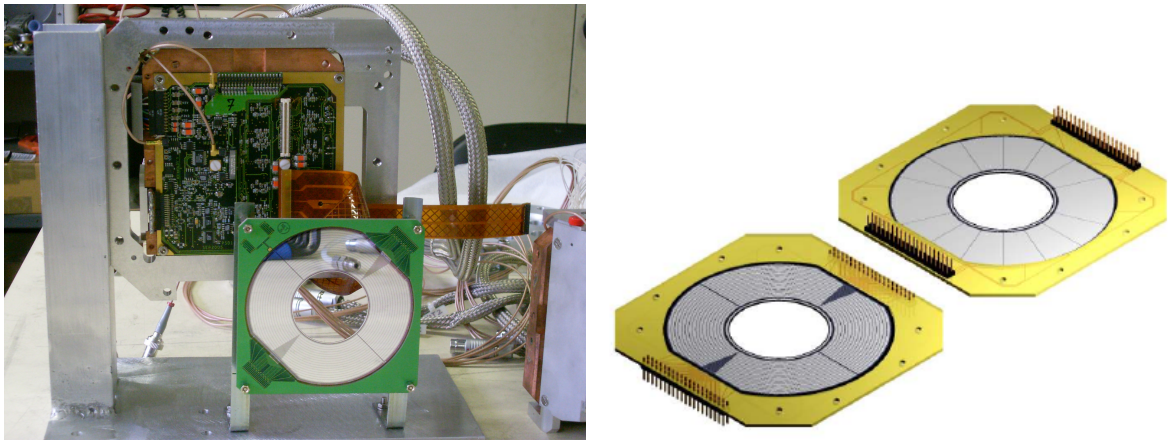

(a) **(b)**

Figure 2.9: *(a) S1 detector (foreground of the photo) and its electronic card. (b) S1 detector showing separately its front side (left) and back side (right).*

It has 16 concentric rings on the front side with a radial-pitch of 1.5 mm providing the polar angle of the detected particle and 16 sectors on the back side with an angular

pitch of 22°33′ providing the azimuthal angle. Each ring on the front side is further segmented into four parts corresponding to four quadrants, each one has an independent read-out. Correspondingly, four sectors in the back side lies behind a single front-side quadrant. Thus, there are a total of 64 channels on the front side for concentric rings and 16 channels for the sectors at the back side. Similarly to the first stage of MUST2, the front side (detection side) is covered by 400 nm thick aluminum layer, while the back side is protected by a 300 nm layer of gold. The connectors of the initial S1 was modified by the manufacturer in order to fit with MUST2 Kapton connectics.

2.5.2 MUST2 Description

MUST2 [Poll 05] is the second generation of the MUST [Blum 99] array consisting of an ensemble of independent modules. Each module is composed of three stages providing altogether position, energy and time measurements identification of light charged particules. An exploded view of the detector is shown in figure 2.10.

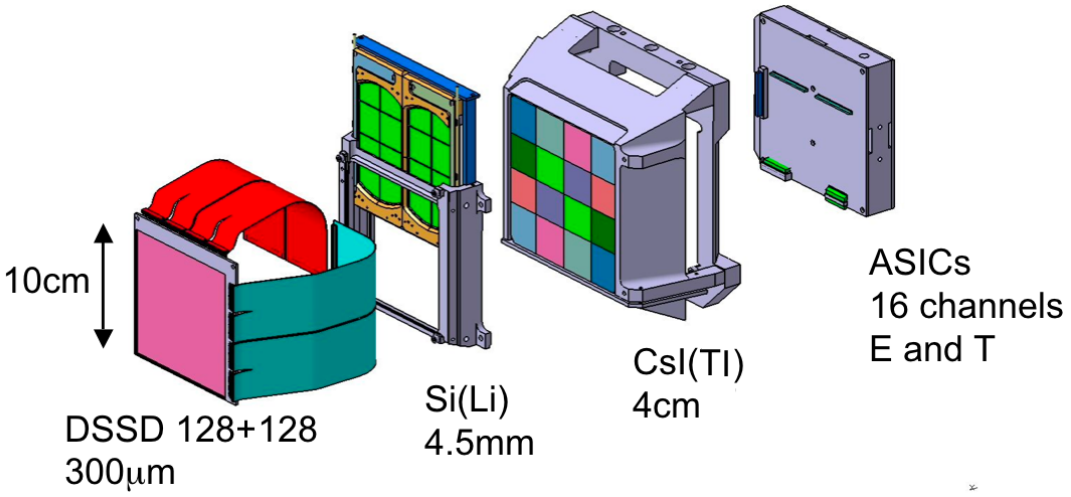

Figure 2.10: *Exploded view of a MUST2 Telescope.*

2.5.2.1 First stage

The first stage is a large-area double-sided Silicon strip detector (DSSD) made by Micron semiconductors. It has an active surface of 100 cm×100 cm and a thickness of 300 ± 5 µm, enabling to measure protons with full energy up to 6 MeV. The detector segmentation consists of 128 strips on each side. On both sides the charges are collected on a 400 nm thick aluminum layer deposited on the strips. This aluminum layer insures a pulse-shape that is independent of the hit location on a particular strip, which is important for a good time-of-flight resolution. The strip signals are transmitted to the front-end electronics placed at the back of the telescopes. Energy and time pulses were transmitted using Kapton connectors used originaly for DSSDs in MUST2.

2.5.2.2 Second stage

This part of the detector consists of two identical *lithium-drifted silicon* crystals (102 mm× 56 mm × 5 mm) of two types made by Jülich Reaserch Center[5] in Germany (3 detectors), and the detector department of IPN-Orsay respectively (1 detector). One pair of crystals is held together by a common aluminum frame mounted 17 mm behind the DSSD. A pair of Si(Li) is shown in figure 2.11. Each crystal is electrically segmented into 8 pads

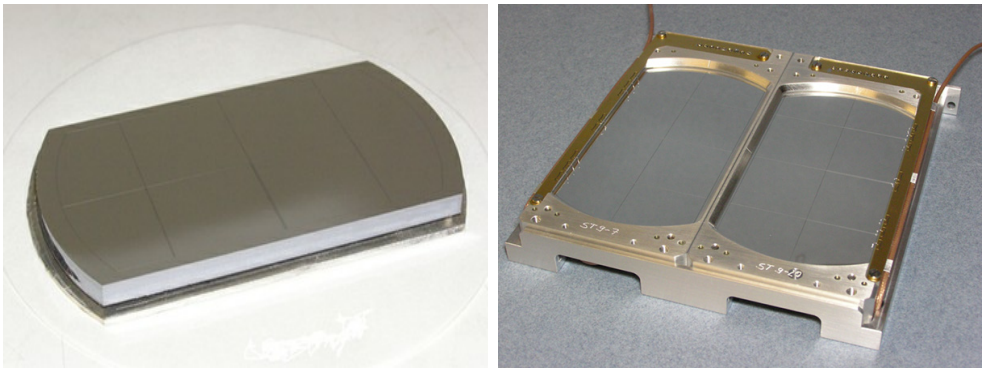

(a) (b)

Figure 2.11: *Second stage of a MUST2 Telescope. A Si(Li) crystal before mounting (a). A pair of Si(Li) crystals with their coresponding aluminum frame (b).*

(20 mm × 20 mm) having independent energy channels. The pads on the borders are shaped to fit the aluminum frame (see figure) hence reducing slightly the detection surface. When coupled to the DSSD, the covered dynamic range for a proton is 31 MeV.

2.5.2.3 Third stage

The third and final stage of the detector is made out of 16 Cesium ioded scintillator crystals with thallium as the activator material. When stacked together a truncated pyramidal-shape takes form with a detection surface of 30 mm × 30 mm and 40 mm depth for each crystal. This detector is placed 30 mm behind the DSSD and can stop protons up to 115 MeV. This stage of the telescope was not used during the experiment since the reaction dynamics was fully covered by the two first stages. The applied bias of the first and second stage was held constant during the whole campaign and is given below in table 2.2.

[5] Jülich Forschungszentrum.

Detector	DSSD voltage (V)	DSSD current (μA)	Si(Li)-1 voltage (V)	Si(Li)-1 current (μA)	Si(Li)-2 voltage (V)	Si(Li)-2 current (μA)
T1	80	1.30	400.5	28.02	600.6	8.36
T2	80	1.00	600.5	5.48	600.6	4.08
T3	60	0.70	600.7	5.40	600.6	4.02
T4	80	0.40	450.3	16.42	450.2	14.92
S1	60	0.60				

Table 2.2: *Bias voltage applied on the Silicon detectors and their inverse currents during the experiment.*

.

2.5.3 MUST2 electronics

The MUST2 electronics hardware is composed of three basic units:

- the MATE ASICS,
- the MUFEE boards,
- the MUVI VXI modules,

described in the following sections.

2.5.3.1 The MATE ASICs

MATE, **M**ust **A**sic for **T**ime and **E**nergy, is an **A**pplication **S**pecific **I**ntegrated **C**ircuit (ASIC) designed by the "Service d'Electronique des Détecteurs et d'Informatique" (SEDI) at the CEA, Saclay, in collaboration with IPN Orsay. Its main role is to process signals delivered from the MUST2 detector. One MATE has sixteen channels and can treat the signals from sixteen detector units of any of the three MUST2 stages discribed above. The architecture of one channel is given in figure 2.12. The first stage of a single channel is a Charge Sensitive Amplifier (CSA) for bipolar signals[6]. The Amplifier can treat energies up to 60 MeV, the amplification of charges is linear for energies between 0 and 45 MeV, above which a non-linearity of 6.10^{-2} % takes place.

The CSA is followed by two branches destinated to treat energy and time of the detected particle. The energy branch consists of a shaper and a *Track and Hold* unit. After amplification, the pulse is shaped with a *CR-RC* filter having 1 μs of peaking time for the DSSD and 3 μs for the Si(Li) and the CSI(Tl) stages. The shaping reduces the noise, which improves the resolution and preserves the amplitude of the physical signal.

[6]The X and Y strips signals are of different polarities.

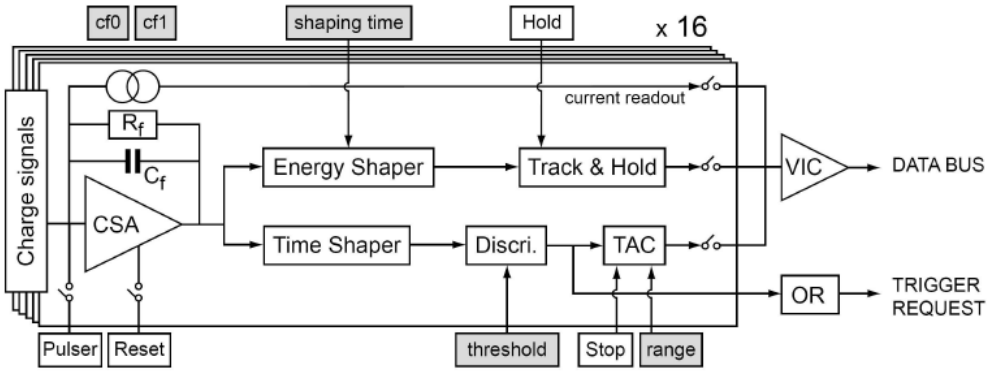

Figure 2.12: *Electronic diagram of one of the sixteen channels in a MATE unit.*

Afterwards the amplitude is memorized in the *Track and Hold* unit waiting for a *Hold* command to trigger the read-out phase.

The time branch also consists of a shaper, followed by a Leading-Edge Discriminator (LED) and finally by a Time to Amplitude Converter (TAC). When the amplitude of the time-shaped pulse is larger than a programmable threshold, the LED sends a *start* signal to the TAC, the conversion of time continues until the arrival of an external *stop* signal. After treating energy and time pulses, the analog signals are transmitted through a Voltage-to-current Converter (VIC) to the 14 *bits* Analog to Digital Converter (ADC) of the MUVI card discussed below. The intrinsic resolution of electronics is 20 keV for energy and 500 ps for time, for further details *cf.* [Moug 08].

2.5.3.2 MUFEE

The MATEs for each MUST2 module, are implanted on two quasi-identical MUFEE cards (**Mu**st **F**ront **E**nd **E**lectronics), connected to the detectors via 20 cm length kapton tapes. On each card there is a total of nine MATEs where eight of them are destined for treating one side of the DSSD ($8 \times 16 = 128$ strips) and the ninth MATE is reserved for the 16 Si(Li) pads on MUFEE-X card or the 16 CsI(Tl) pads on the MUFEE-Y card.

These cards are the interface by which the MATEs communicate with the detector and the MUVI card. Besides their role of multiplexer[7], the MUFEE cards transmit the strip pulses to the MATEs using Time-Division Multiplexing, where the signals are sequenced, one after the other, and then associated with the appropriate MATE channel. They also transmit commands from the MUVI card such as the reading-out of an event and TAC *stops*.

MUFEE cards are also the host of inspection elements such as temperature sensors that can be exploited for sending an alarm signal when a programable temperature threshold

[7]Multiplexers are mainly used to increase the amount of data to be sent within a certain amount of time and limit the number of cables.

is reached, and a linear pulse generator for test and calibration purposes. They are placed close behind the detector in the reaction chamber in a copper block. A liquid cooling system is used to evacuate the heat excess. The liquid[8] goes through and out of the copper block supporting one MUFEE card from each side as shown in figure 2.13 taken from [Moug 08].

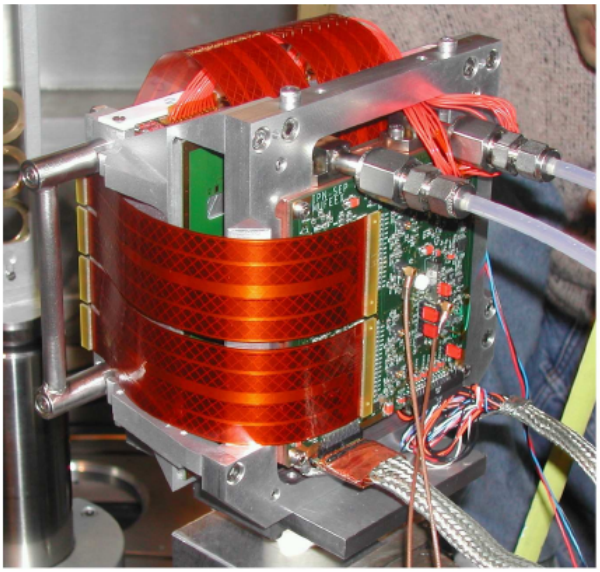

Figure 2.13: *Cooling system of a MUST2 Module along with the metallic block and one of the MUFEE cards. The other MUFEE card lies on the other side of the metallic block.*

2.5.3.3 MUVI

The MUVI card (**Mu**st in **VXI**) [Baro 03] represents the last basic unit of the MUST2 electronics, and can be regarded as the interface between the acquisiton system and the MUST2 detectors. It is a single width unit in VXI-C mounted outside the reaction chamber, and consists of four independent Control Acquisition Sectors (CAS). Each CAS card controls and commands a single MUST2 module and insures the following tasks:

1. Coding of all analogic data (energy and time) from the ASICs,
2. Generate trigger after a read-out command,
3. Transmit to MUFEE cards the *Stop* signals for TAC,
4. Transmit read-out and data coding using the 14 *bits* ADC,
5. Perform pedestal and differential non-linearity corrections.

[8] Consisting of water mixed with alcohol in the same proportions.

2.6 Heavy-residue detectors

A gridded ion chamber and a plastic scintillator were placed at the end of the beam line. These detectors were used to identify the heavy-residue nucleus using $\Delta E - E$ and $E - ToF$[9] techniques.

2.6.1 Ionization Chamber

The ionization chamber was an electron-sensitive gridded ion chamber, operational in pulse mode, designed at GANIL. Its characteristics are summarized in table 2.3.

The ionization of gas molecules by a passing charged particle, creates ion pairs *(electron + positive ion (hole))* along it's track. The deposited energy is proportional to the number of electron-hole pairs created. The electrons and ions (charge carriers) drift in opposit directions inside the volume of the ionization chamber due to the electric field generated by the cathode and anode. The motion of these charge carriers induces an electric signal that can be used to estimate the energy loss of the beam-like particle in this detector.

The output electric signal depends also on the velocity of the charge carriers and their positions inside the volume of the detector. Since the mass of an electron is lighter with respect to the mass of the corresponding ion, its drift velocity is ~ 3000 times greater. In these conditions the output signal will be a mixture of a *fast* pulse with a short rise time due to the fast electron motion and a *slow* pulse with a long rise time due to the slow ion motion.

Operational mode	pulse mode
Active volume	60 mm × 60 mm × 100 mm
Filling gaz (pressure)	CF_4 (70 mbar)
V_{Anode}	+600 V
Frisch grid	0 V
$V_{Cathode}$	−600 V

Table 2.3: *General characteristics of the ionization chamber*

The dependence of the pulse amplitude on the position of interaction and the *slow*-hole component signal can be removed by using a *Frisch grid* placed close to the anode (see figure 2.14). The operation principle of a Frisch grid is explained as follows. The electron-hole pairs are created in the active volume between the grid and the cathode where the grid is maintained to an intermediate potential between the electrodes. The electrons, under the influence of the reigning electric field will move on towards the anode and pass through the *Frisch grid*. The signal is therefore only measured over the volume between the grid and the anode. This way, the hole component of the signal is screened since the only charge carriers between the grid and the anode are the electrons.

[9] **T**ime **o**f **f**light.

During this experimental campaign the output signal was stored in an analogic acquisition where the deposited charge was integrated in 3 µs time interval. Data were also digitized in 8.75 µs time intervals with a frequency of 400 MHz (*i.e.* 350 samples).

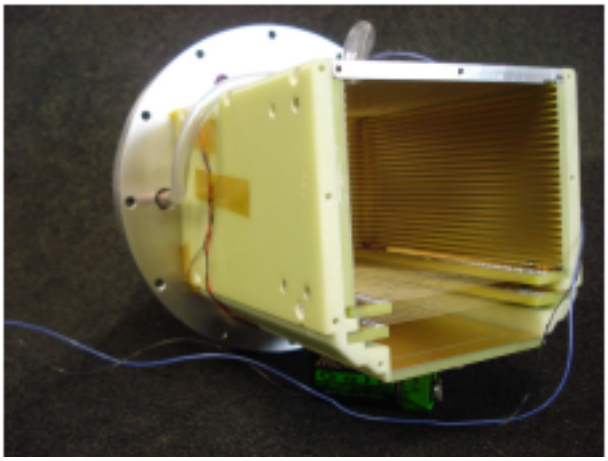

Figure 2.14: *Ionization chamber in E507. The Frisch grid is located in the bottom of the chamber just above the anode plate.*

2.6.2 Plastic detector

The plastic scintillator has a detection surface of 6 cm × 6 cm and is coupled to a photomultiplier (see figure 2.15). This detector was used to measure the energy of the beam-like particules and their Time-of-Flight with respect to the time reference detector (CATS2). The plastic material absorbs the kinetic-energy of the projectile-like particle and reemits it in the form of visible light (fluorescence). The emitted light is then guided by a light-pipe to a photomultiplier. The latter converts the scintillation pulse into a usable electrical signal.

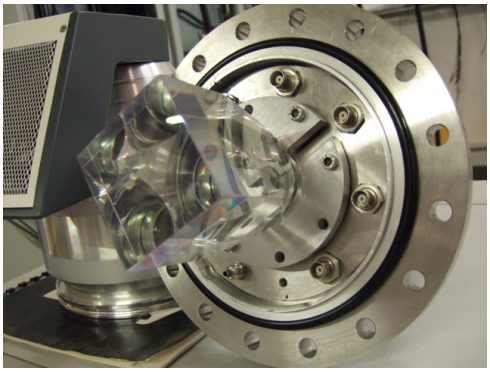

Figure 2.15: *Plastic scintillator coupled to a light-pipe.*

2.7 γ-ray detectors : EXOGAM

EXOGAM is a compact, highly efficient and segmented germanium-detector array [Simp 00] suited for γ–ray spectroscopy. The original array is composed of 16 modules called "clovers"(*cf.* figure 2.16a), four of them were used along the whole experimental campaign. Each clover consists of 4 independent crystals, closely packed together in the same housing, each one being electrically segmented into 4 regions which makes in total 64 segments corresponding to 16 independant crystals.

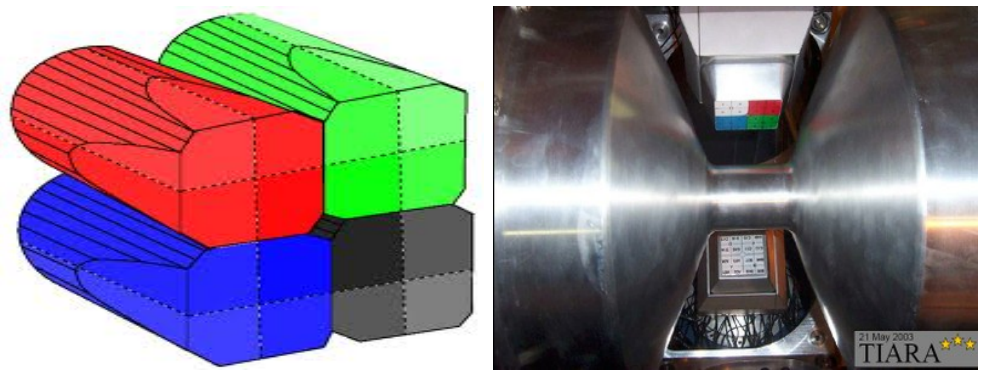

(a) **(b)**

Figure 2.16: *Exogam clover consisting of 4 independent crystals. Each crystal is segmented into 4 electrically-independent regions (a). Close geometry of Exogam coupled with TIARA setup(b).*

The charge from the whole crystal volume is collected with the central contact and gives an accurate measurement of the energy of the incoming γ-rays while each individual segments are sensitive to only a fraction of the total volume.

The clovers were located close to the target point as shown in figure 2.16b. This configuration increases the solid angle sustained by each *Ge* crystal but degrades the energy resolution due to Doppler effect. The resolving power can be restored by using the electrically-independent segments to reduce the opening angle of the detector.

In our experiment the target was shifted 5 cm upstream so as to increase the angular coverage of the light-charged particules detectors. Data from EXOGAM are not exploited in the present work.

2.8 Positioning and alignement of detectors

In order to measure the scattering angle of a particle, one must know precisely the position of each position-sensitive detector (CATS and DSSDs) with respect to some reference position in space. The global position of each detector was measured during the experiment setting-up. The measurements were done by the "Instrumentation pour la physique - Alignement" group at the GANIL facility. The position of the different detectors with

Detector	X (mm)	Y (mm)	Z (mm)
CATS1	−0.2	+0.6	−976
CATS2	+0.3	+0.1	−576
Tiara target frame	+0.2	+0.1	−50
T1	−49.17 −49.00 +48.32 +48.11	+63.68 +126.1 +125.69 +63.19	−155.31 −80.75 −80.58 −155.17
T2	+64.67 +127.24 +127.19 +64.63	+47.67 +47.54 −49.76 −49.65	−154.91 −80.42 −80.60 −155.09
T3	+48.70 +48.56 −48.76 −48.61	−65.06 −127.58 −127.60 −65.05	−154.73 −80.30 −80.49 −154.94
T4	−64.31 −127.11 −126.80 −64.02	−49.84 −49.83 +47.43 +47.43	−155.39 −81.11 −80.86 −155.13
S1	−50.31 +49.59 +49.72 −50.22	+49.45 +49.19 −50.62 −50.37	−158.91 −158.75 −158.62 −158.78

Table 2.4: *Positions of the detectors and the target holder, with respect to the hypothetical target position in the E530 experiment [Giro 11]. For CATS1 and CATS2, the measured positions corresponds to the center of the detector. For MUST2, the position of the four corners of the first stage in each Module was measured. And finally for the S1, the 4 measurements were done on the corners of its supporting frame.*

respect to the target hypothetical position in the previous experiment of the campaign are given in table 2.4. The position uncertainties, provided by the geometer, are 0.15 mm in X and Y directions and 3.00 mm in Z direction.

We must mention that all positioning measurements were taken at room temperature and pressure. Vacuum may lead to slight mechanical shifts of the different elements and the uncertainties given by the geometer no more holds. Other experiments already reported position shifts reaching 3 mm [Ramu 09]. This would lead to erroneous angle and energy measurements. The correction of these shifts were taken into account during data analysis. In our case the target was shifted 1 mm towards S1 with respect to the position given by the geometers in such a way to reproduce the ground state at 0 MeV in the excitation energy spectrum (*cf.* 4.1).

2.9 Electronics and data acquisition

The same data acquisition logic was used for the whole experiment campaign. In this section, we will explain briefly the general acquisition setup. The detailed electronics diagrams of each detector can be found in Appendix B.

The selection of a "good" event requires an electronics module that is able to receive signals from several detectors and decide wether the acquisition chain must be triggered or not. The GMT (*Ganil Master Trigger*) fulfills these requirements. It is a decision module developped in GANIL in VXI-C format. It can receive and treat 16 logic signals coming from master detectors. When the GMT judges an event is valid, it generates a trigger signal called FAG (Fenêtre d'Acquisition Ganil). Any signal produced by any detector is read only if it is in time coincidence with the FAG gate reference.

Detector(s)	(allowed event / total events)
CATS1	(1/1000)
CATS2	(1/3000)
T(1,2,3,4)	(1/1)
S1	(1/1)
logic OR (T_{all})	(1/1)
logic OR (T_{all},S1)	(1/1)
EXOGAM	(1/200)
Ion Ch.	(1/1000)
Plas. Sc.	(1/1000)

Table 2.5: *GMT trigger channels. T_{all} refers to the set of the four MUST2 modules. In contrast with other detectors, MUST2 and S1 are allowed to trigger the acquisition chain whenever they detect a particle.*

The delayed logic-signal from CATS2 detector, made valid by time coincidence with the FAG gate, represents the common stop to all of the detectors. The start signal, on

the other hand, is the logic signal from the fired detector itself (in case of MUST2 this signal is sent by the MUVI card).

The channels of the GMT were set to receive the 12 master signals shown in table 2.5. The detectors intercepting the beam (*i.e.* CATS, Plastic...) or having a high detection rate (EXOGAM), can not be allowed to trigger the acquisition system each time they detect an event, since they would saturate the acquisition chain. Dividers are used in order to reduce by orders of magnitude the rate of these detectors in the GMT trigger (see right-hand side column in table 2.5). When the signal is valid, it is encoded by an electronic specific for each detector. The amplitude or the charge of the signal is read and processed by an adapted electronic module in order to record the energy or the time associated.

Hardware Configuration (ADC, QDC, TDCS, MATES) is done via a graphical interface called DAS (Data Acquisition System). The latter allows to manage electronics settings, to acquire the data event by event, and to partially treat them on line. A visualization interface provides a way to control the proper functioning of the detectors, as well as viewing the analyzed spectra online.

Chapter 3

Data analysis

In this chapter, the different stages of data analysis are described. The entire analysis presented here is performed under ROOT "framework".

3.1 Beam-tracking detector : CATS

In order to determine with high precision the impact position of the beam on the target, and its angle of incidence before the interaction, two CATS detectors were place upstream the target.

3.1.1 Charge calibration

The CATS detectors were described in chapter 2. Each cathode strip has its own electronics. Therefore for the same amount of charge deposit, the response is different for each channel. In order to calculate the centroid of a charge-pattern over several cathode-strips one must normalize their corresponding gains to the gain of a strip chosen as a reference[1].

When a strip is fired, all the charges from all other strips will be equally coded, even if no signal was detected. In the latter case, the encoded value corresponds to the background noise and the accumulation of such events leads to a peak close to zero called the pedestal.

The calibration procedure is achieved by injecting a pulser signal on the anode wires inducing a signal on the cathode planes. Each strip receives the same charge and by varying the amplitude of the pulser signal by discrete and equal steps (see figure 3.1a), the dynamic range of the strip is totally covered. The peak positions for each strip is then plotted versus the peak positions of the reference strip, and a linear regression is fitted to the data as shown in figure 3.1.

The normalized charge of a $(\text{strip})_i$ is given by,

$$Q_i = (q_i - p_i)a_i + b_i \tag{3.1}$$

where,

[1] A reference can be any strip characterized by a low noise, a good resolution, a linear response and which has operated along the whole experiment

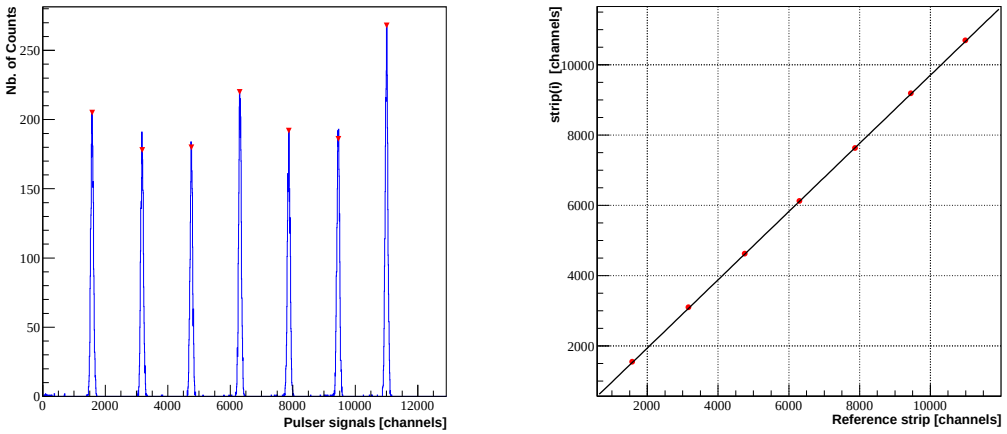

(a) *pulser signal on* $(strip)_i$ **(b)** $(strip)_i$ *vs reference strip*

Figure 3.1: *Calibration of a cathode strip with respect to the reference strip.*

- q_i is the measured charge,
- p_i is the measured pedestal,
- and a_i and b_i are the fitted parameters.

During the offline analysis, a signal is considered valid only if it exceeds a threshold value. This threshold value is determined for each strip by,

$$Q_{thresh} = p_i + \alpha.\sigma \tag{3.2}$$

where σ represents the pedestal width and α is a parameter insuring a clean signal. For this experiment, we set $\alpha = 4$.

3.1.2 Reconstruction Algorithms

The hit pattern induced by the passing ion on the cathode strips is used to calculate the best estimate for the avalanche position, *i.e.* ion position. This procedure improves the resolution, before reconstruction, equal to the strip-width (*i.e.* 2.34 mm). Algorithms which determine the centroid of charge for detectors similar to CATS were already investigated in [Lau 95]. In the present work we have investigated two different classes of algorithms: center-of-gravity and the analytic-function fit.

We define the strip contiguity as the number of contiguous strips having a calibrated charge > 0. Neglecting $\approx 1\%$ of events where only two strips are fired, the minimum number of strips to acquire an information about the passing ion must not be less than three. Table 3.1 gives the percentage of contiguous strips for the same set of events in CATS1.

Nb. of contiguous strips	X	Y
$\geqslant 3$	99.99 %	99.98 %
$\geqslant 4$	96.63 %	96.48 %
$\geqslant 5$	80.86 %	82.36 %
$\geqslant 6$	28.99 %	29.60 %

Table 3.1: *Percentage of contiguous strips in CATS1 detector. A method using 3 contiguous strips (e.g. X^{Sech} or X_3^{COG}) is the best choice for the reconstruction of events in CATS detectors.*

3.1.2.1 Center-of-gravity algorithm

The center-of-gravity algorithm (COG) calculates the trajectory centroid X_n by weighting each strip position x_i with its charge Q_i where n is the number of strips used,

$$X_n^{COG} = \frac{\sum_{i=1}^{n} x_i.Q_i}{\sum_{i=1}^{n} Q_i} \tag{3.3}$$

The strip carrying the largest induced charge is placed at the center of the n-strip distribution, and the other strips are picked alternatively on both sides. In this method it is important to have all the strips and the wires operational during the whole experiment.

The position X_n^{COG} is given in *strip* unit $1 < X_n^{COG} < 28$. The result is transformed to mm using the cathode pitch $w = 2.54$ mm (2.34 mm of strip-width + 0.2 mm of interstrip) where,

$$\mathrm{X_n^{COG}\ [mm]} = (\mathrm{X_n^{COG}\ [strip]} - 14.5) \times w \tag{3.4}$$

When using an odd number of strips (*e.g.* X_3^{COG}) the reconstruction is more precise when the profile of the charge distribution is symmetric with respect to the center of the most significant strip, in other words, when the *real* hit is located in the center of the strip. And it is most erroneous when the charge profile is symmetric with respect to the inter-strip. In the latter case an even number of strips (*e.g.* X_4^{COG}) is more adapted.

Since the systematic errors are roughly linear with respect to the distance separating the real hit position from the center of the most significant strip x_c [Lau 95, Otti 99] a simple correction can be made,

$$x_{corr} = \frac{(x - x_c)}{a_{corr}} + x_c \tag{3.5}$$

where x_{corr} represents the position after correction and a_{corr} is the correction factor. Another correction can also be made for X_4^{COG} though it was not used. In contrast, the systematic errors of higher order COG methods are not linear and simple corrections can not be applied. The correction factors for X_3^{COG} are given in table 3.2. We notice that the corrections on X and Y are similar for the same detector.

plane	a_{corr} (X)	a_{corr} (Y)
CATS1	0.61	0.62
CATS2	0.58	0.57

Table 3.2: *Correction factors for* X_3^{COG}

3.1.2.2 The analytic-function fit algorithm

The analytic-function fit algorithm is based on the hypothesis that the charge distribution can be approximated by an analytical bell-shaped function having 3 parameters (amplitude, mean value, width) such as a Gaussian or a Squared Secant Hyperbolic. This type of algorithm is always done with $n = 3$ strips. In these cases the centroid can be obtained from the charge distribution using the following expressions for the Gaussian function,

$$X_3^{Gaus} = \frac{(X_2^2 - X_1^2)\ln\frac{Q_1}{Q_3} - (X_3^2 - X_1^2)\ln\frac{Q_1}{Q_2}}{(X_2 - X_1)\ln\frac{Q_1}{Q_3} + (X_3 - X_1)\ln\frac{Q_1}{Q_2}} \tag{3.6}$$

When the three strips are contiguous the expression reduces to,

$$X_3^{Gaus} = \frac{w}{2}\frac{\ln\frac{Q_1}{Q_3} - \ln\frac{Q_1}{Q_2}}{\ln\frac{Q_1}{Q_3} + \ln\frac{Q_1}{Q_2}} \tag{3.7}$$

The Squared Secant Hyperbolic function is given by,

$$X_3^{Sech} = \frac{a}{\pi}\tanh^{-1}\left(\frac{\sqrt{\frac{Q_1}{Q_3}} - \sqrt{\frac{Q_1}{Q_2}}}{2.\sinh\frac{\pi.w}{a}}\right) + X_1 \tag{3.8}$$

where,

$$a = \frac{\pi w}{\cosh^{-1}\frac{1}{2}(\sqrt{\frac{Q_1}{Q_3}} + \sqrt{\frac{Q_1}{Q_2}})}. \tag{3.9}$$

Q_1 (X_1) is the charge (position) of the central strip having the most significant charge, Q_2 (X_2) and Q_3 (X_3) are the charges (positions) of the 2^{nd} runner-up and 3^{rd} runner-up strip in charge significance, and w is the cathode pitch. In order to use the formula of X^{Sech} (3.8), the neighboring strips must be at the same distance from the central strip. This restriction is not necessary in case of the Gaussian formula (3.6).

3.1.3 Validity of reconstruction

To check the validity of reconstruction, a grid made by a squared piece of brass with holes of different diameters (1 or 2 mm) and asymmetric positions (*cf.* figure 3.2a) was placed behind each CATS for position calibration. The image of the holes in the grid was

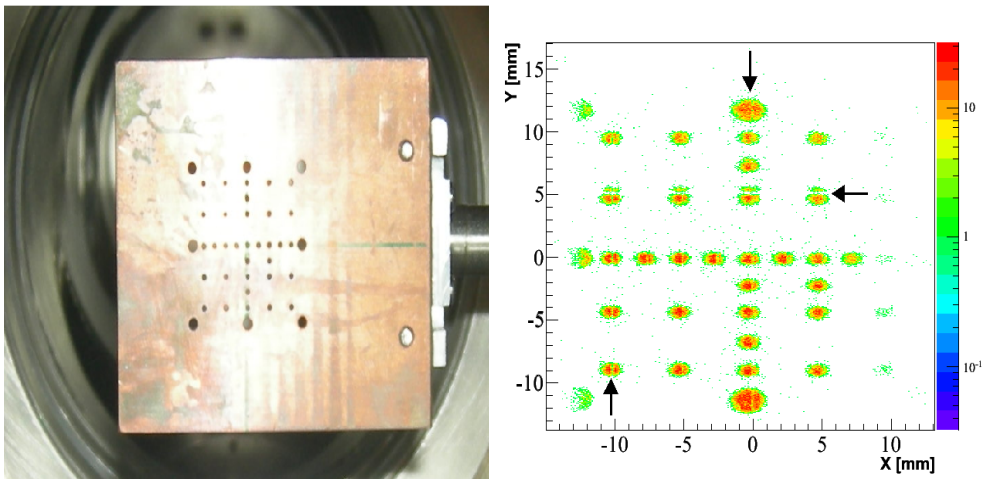

(a) (b)

Figure 3.2: *(a) Grid placed behind CATS1. (b) Reconstruction using X_3^{COG} with correction factors given in table 3.2 .*

collected on CATS and a test of the reconstruction algorithms was made. The grid is also used to identify any strip or plane inversions in the CATS detector.

In figure 3.2 we show the reconstruction using the COG method for 3 strips after applying the correction. The quality of reconstruction has been significantly improved after the correction procedure. However, even with a careful choice of correction factors, a splitting of spot is observed (indicated by black arrows in figure 3.2b).

When using a bell-shaped function, no splitting is observed (see figure 3.3). A comparison of X^{Sech} to X_3^{COG} and X_4^{COG}, respectively shows that the former algorithm is better.

The reliability of the analytic methods can be verified by comparison to the COG methods. In figure 3.3 (c) and (d) panels show the difference between X^{Sech} and X_3^{COG} versus the distance to the center of the strip $(X - X_c)$. The X^{Sech} is similar to X_3^{COG} in the region where the latter is most reliable *i.e.* at the center of the strip. When compared to X_4^{COG}, both methods are in agreement near the borders of a strip. The systematic error of the analytic-function fit is smaller than the one of the COG methods but far from being linear, *i.e.* no simple correction can be done without an appropriate characterization of the detector. In a similar way X^{Sech} was compared to X^{Gaus} and both methods found to be equivalent. However, according to reference [Lau 95], X^{Gaus} has a larger systematic error. For the rest of the analysis the X^{Sech} will be used.

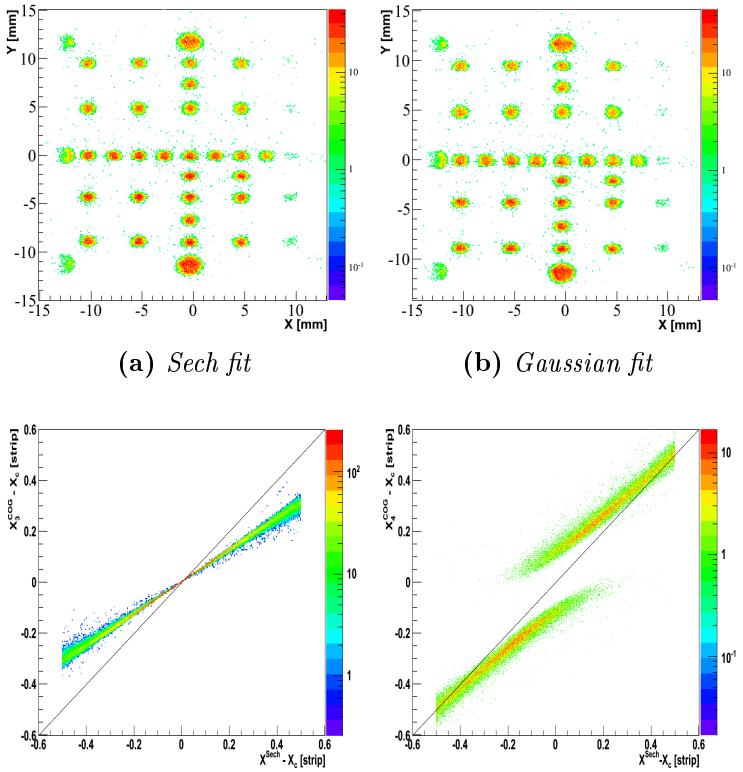

(a) *Sech fit* **(b)** *Gaussian fit*

(c) $X_3^{COG} - X_c$ *vs* $X^{Sech} - X_c$ **(d)** $X_4^{COG} - X_c$ *vs* $X^{Sech} - X_c$

Figure 3.3: *Reconstruction of the grid using* X^{Sech} *(a) and* X^{Gaus} *(b) for the same run. Both methods give similar results. (c) The distance to the center of the most significant strip* X_c *of a position calculated with* X^{COG} *(*$X_3^{COG} - X_c$*) versus the same distance calculated with the analytical method* X^{Sech}*. (d) The same spectrum with* X_4^{COG} *compared to* X_3^{Sech}*.*

3.1.4 Reconstruction of beam on the target

Given the positions of the beam impact on CATS1 and CATS2 (see figure 3.4 on the left-hand side and center panels) we can calculate the position of interaction of the beam with the target (right-hand side of figure 3.4). In order to do so, we use the distance between CATS1 and CATS2 ($C_1C_2 = 400$ mm) and the distance between CATS2 and the target ($C_2C_t = 526$ mm). The method is explained at the end of this chapter, section 3.4.1. We notice that the beam is considerably broad in X and Y directions at CATS1 and CATS2 planes, then it is focused at the target plane in Y-direction ($\Delta Y \approx 5$ mm), with roughly a constant spread in X direction ($\Delta X \approx 15$ mm).

The left-hand side panel of figure 3.5 shows the reconstructed events at the target plane. No selection is made on the trigger and events correspond essentially to reaction events, for which MUST2 or S1 are hit. Clearly, an ellipsoidal beam spot in the center of the figure having the highest beam intensity can be identified. At the exit of LISE, the beam spot is broad and covers the detection surface of the beam trackers. A large fraction of counts in this plot comes from reactions induced by the beam hitting the S1 frame from

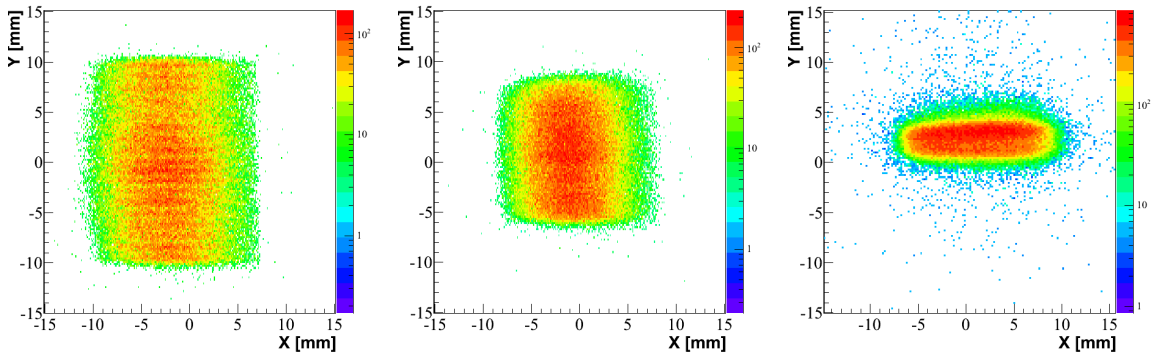

Figure 3.4: *Beam profile reconstructed in the plane of CATS1, CATS2 and the target from left to right, respectively.*

the back. The abrupt change in event density along the horizontal (vertical) lines at about 30 mm from the center of the graph corresponds to the "shadow" of the CATS1 detector where the S1 detector triggers the acquisition system. This "shadow" has the typical squared geometry of the detector as shown in figure 2.7 of chapter 2. Projectiles passing through the hole of S1 without interaction in the target can not be constructed and thus the shadow of S1 is limited to the border of its circular hole ($\varnothing = 48$ mm). Upon selecting the heavy residue in the plastic scintillator at zero degree, the beam reconstruction reduces mainly to the central beam spot as seen on the right-hand side of figure 3.5. In order to avoid reactions induced by the beam hitting the target frame or any other element (beam trackers, S1 detector), a selection of reactions on the CD_2 target material was made and used during the whole analysis and is shown as the black contour in figure 3.5-a.

3.1.5 Resolutions

3.1.5.1 Detection efficiency and time resolution

As described in [Otti 99] time resolution and detection efficiency depends strongly on the incident-ion energy loss in the detector. The energy loss of a ^{68}Ni in the CATS detectors is ≈ 9.8 MeV which is relatively high. The detection efficiency is supposed to be ~ 100 % in CATS1. For a check of the time resolution, the distribution of time intervals between start (CATS1) and stop (CATS2) pulses were recorded. The full width at half maximum of the time distribution is used to determine the time resolution (= 0.37 ns) since both CATS detectors have roughly the same characteristics.

3.1.5.2 Position resolution

To determine the position resolution of the beam trackers, the best way would be to use a beam with low divergence. Since this is not possible in our case we use the measurement performed with a grid in order to determine the resolution. The image of the grid holes

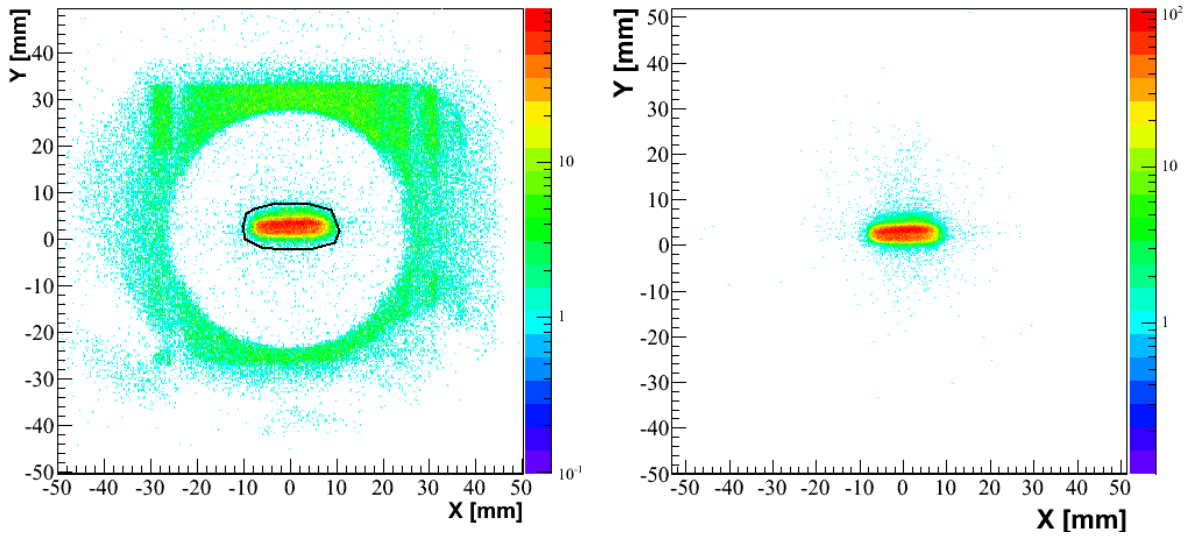

Figure 3.5: *On the left-hand side panel, the geometrical reconstruction of the beam position in the target plane with no selections applied. In the right-hand side panel, is shown the same plot after requesting the heavy residue in the plastic scintillator.*

is formed by a convolution between a window-function representing the width diameter of the hole and a gaussian representing the resolution of the detector. The resolution can be drawn out by deconvoluting the image spot in the X(Y)-direction.

Since the holes are of circular shape, one must select only the events passing around the diameter parallel to X (Y), and having the less possible deviation as shown in figure 3.6a. The events corresponding to the three central holes are then projected on the X-direction (Y-direction), *cf.* figure 3.6 b and c, and fitted by Gaussian-functions in order to extract their full width at half maximum W. The measured widths are averaged over the three central pics leading to W_{mes}. Position resolution (W_{res}) is then deconvoluted from the hole[2] resolution W_{hole}, using the following expression,

$$W_{mes}^2 = W_{res}^2 + W_{hole}^2 \tag{3.10}$$

where,

- W_{res} is the CATS detector position resolution,
- W_{mes} is the measured resolution,
- $W_{hole} = 2\sqrt{2\ln 2}\sigma_{hole}$ is defined as the hole resolution,

[2] The hole will induce a uniform distribution of length L (= 1 mm). The variance $\sigma_{uni.}^2$ of a uniform distribution of length L is given by:

$$\sigma_{uni.}^2 = E(x^2) - E(x)^2 = \frac{1}{L}\int_0^L x^2 dx - \frac{1}{L^2}(\int_0^L x dx)^2 = \frac{L^2}{12}$$

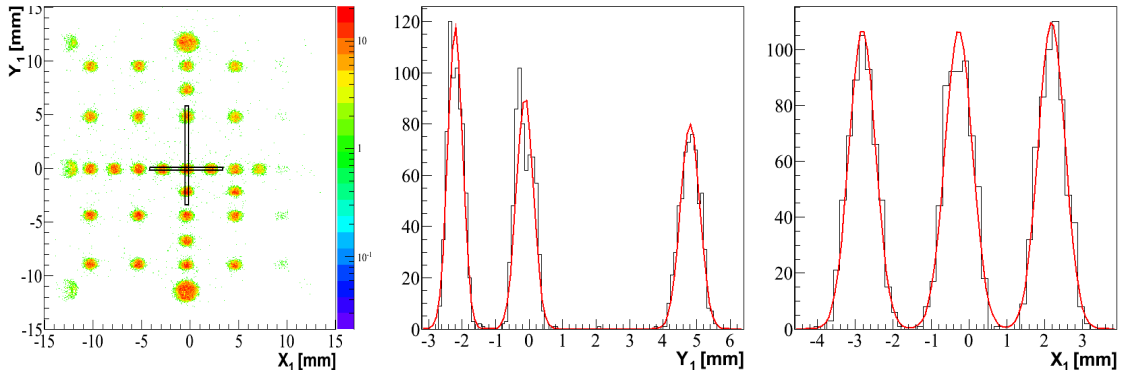

(a) (b) (c)

Figure 3.6: *(a) The holes in the grid behind the CATS detectors are circular. A selection of events along the horizontal (vertical) diameter was made in order to calculate the resolution on X (Y) direction. (b,c) Position resolution in X and Y directions for CATS1 and CATS2, respectively.*

and σ_{hole} is the standard deviation related to the uniform distribution of the hole, given in terms of L by,

$$\sigma_{hole} = \sqrt{\frac{L^2}{12}}$$

The finite position resolutions on the CATS detectors induces an uncertainty on the incident angle. For an ion parallel to $Z-axis$ and by using the small-angle approximation ($\delta\theta_{max} \sim 0.1°$), the maximum angular deviation $\delta\theta_{max}$ can be calculated as,

$$\delta\theta_{max} \approx \tan(\delta\theta_{max}) = \frac{W_{res}}{C1C2} \tag{3.11}$$

where, $C1C2 = 400$ mm is the distance between the two CATS detectors. Table 3.3 recapitulates the different resolutions in position and angle in X and Y directions.

Resolutions	H_{CATS1}	H_{CATS2}	$\delta\theta_{max}$
X	0.65 mm	0.65 mm	0.10°
Y	0.4 mm	0.4 mm	0.06°

Table 3.3: *Position and angular resolutions of CATS detectors in X and Y directions. Both CATS detectors are considered to have equal resolutions.*

3.2 Light charged particle detectors : MUST2 et S1

To determine the energy and the time of the incident charged particles in the detectors MUST2 and S1 in physical units, it is necessary to establish a correspondence between

the electronic channels and the physical information. To determine the energy measured by the DSSD or the Si(Li), we have used a 3-alpha source for which the emission energies are known accurately.

3.2.1 Double-sided silicon-strip detectors : Energy Calibration

The MUST2 and S1 detectors are described in sections 2.5. The DSSD is calibrated in energy using alpha sources placed inside the reaction chamber. The same calibration procedure was applied to both MUST2 and S1. The detectors were calibrated before and after each experiment of the physics campaign.

A 3-α source (^{239}Pu - ^{241}Am - ^{244}Cm) was used to calibrate the DSSDs for MUST2 and S1. This source contains radioactive isotopes that decay by emitting α particles with several discrete energies. Its most intense energy peaks are summarized in table 3.4. During

Radioisotope	$T_{1/2}$ (years)	E_α [MeV]	I_α [%]
^{239}Pu	$2.411(3)\,10^4$	5156.59(14) 5144.3(8) 5105.55(8)	70.77(14) 17.11(14) 11.94(7)
^{241}Am	$4.326(6)\,10^2$	5485.56(12) 5442.80(13) 5388	84.8(5) 13.1(3) 1.66(2)
^{244}Cm	$1.81(1)\,10^1$	5804.77(5) 5762.64(3)	76.90(10) 23.10(10)

Table 3.4: *Most intense energies of the $3-\alpha$ source used in the calibration of MUST2 and S1 detectors. I_α is the intensity of radiation relative to each isotope.*

the calibration procedure we noticed the poor reproductibility of the target-holder position. A careful study of the hit patterns of the alpha source on the detectors has revealed shifts of the target-holder position with respect to its supposed position for the 4 sets of calibration runs. Differences up to 3 mm have been deduced from the α-source data. The hit patterns presented in figure 3.7 show the effect of the α-source position on the number of hits received by each X and Y strip. It is possible to determine the exact position of the alpha source by fitting the corresponding hit pattern for each detector. The newly calculated α-source positions are taken into account for the rest of the calibration procedure.

Each strip (or pad) of MUST2 and S1 detectors must be individually calibrated since it has its own electronics chain and thus its own gain and pedestal.

The MUFEE cards described in the previous chapter send the analogic signal to the MUVI card which allows them to code the energy on 16384 channels. The charge seen by Y strips (energy, time) are coded between 0 and 8192 channels and those seen by X strips

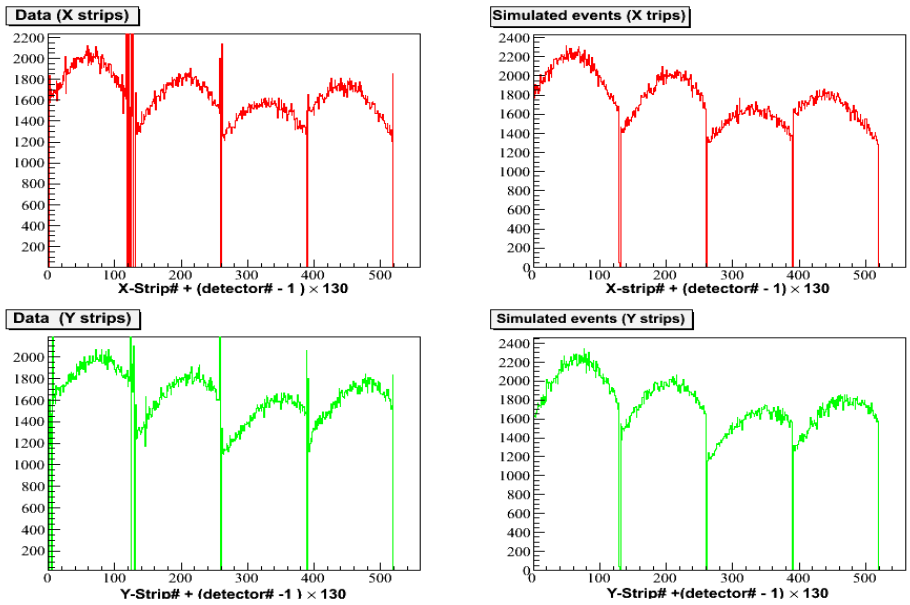

Figure 3.7: *α source energies versus front-side strip number in MUST2 telescopes. Measured data are given in the left-hand side panels and simulated data in the right-hand side panels. Top(bottom) panels correspond to X(Y) strips. In each panel we present data corresponding to the four MUST2 telescopes starting by Telescope 1.*

between 8192 and 16384[3]. When a MUST2 Module is hit, signals of all the strips are coded. Reading-out all these signals implicate a long dead-time that can be avoided by suppressing the pedestals using a functionnality of MUST2 MUVI cards, as follows. These pedestal positions are first determined and stored in a file by using a code implemented on the MUVI cards. The stored positions are used to align all pedestals on channel 8192. Then all data lying in a given channel range between 8160 and 8223 (in our experiment) are suppressed.

The calibration procedure takes into account the pedestal position and the 0.4 µm aluminum dead layer covering the detectors. The three most intense alpha peaks (*cf.* table 3.4) in the energy spectra of each strip are fitted with gaussian functions taking into account the neighboring less-intense peaks in order to determine their precise centroids and widths. Once the peak locations for each channel has been determined their corresponding energies are calculated taking into account the energy losses of alpha particles in the aluminum dead layer. For every strip we assume a linear relationship between the channel number from the ADCs and the energy of the alpha particle deposited in the detector,

$$E_i = g_i|channels_i - 8192| + E_{0i}$$

where g_i and E_{0i} are the gain and the energy offset, respectively. For each strip, the g_i and E_{0i} are first determined from the positions and calculated energies of the three main α energies. The mean value of energy offset must be close to zero for each side of

[3]Zero Y-strip energies are coded on channel 8192 and larger energies in smaller channels (inverse coding).

the detector since all pedestals are aligned to channel 8192 as mentioned before. This was not the case during this first calibration where the calculated mean of energy offset showed a ≈ 100 keV shift with respect to zero energy. This shift was attributed to an underestimated thickness of the dead layer.

The dead layers are calculated by minimizing the difference between the calculated pedestal and the physical pedestal (0 MeV) for several dead layer thicknesses. A linear response of the detectors and the associated electronics was again assumed. Geometrical aspects (target position, impact position on strip) were taken into account in the procedure.

The obtained values for each side of the DSSD detectors, calculated from energies on the X strips, are summarized in table 3.5 and are compared to those calculated in [Giro 11] for the same detectors and using the same data. We notice a difference between the two sets of values up to 13%. This difference corresponds to ≈ 16 keV in the calculated energy loss for a 5 MeV alpha particle. It is due mostly to the use of different energy loss tables[4]. It is noteworthy that the thicknesses obtained by this method are systematically larger

DSSD	front side (µm) in this work	front side (µm) in [Giro 11]	difference (%)
T1	0.60	0.52	13.3
T2	0.60	0.54	10.0
T3	0.61	0.54	11.5
T4	0.58	0.51	12.0
S1	0.69	0.64	7.3

Table 3.5: *Dead layer equivalent to Aluminum thickness for the DSSD in MUST2 telescopes and the S1 detector. A systematic overestimation of the dead layers in the present work with respect to [Giro 11] is due to the use of different energy-loss tables [Zieg 77].*

than those given by the manufacturer Micron (0.4µm of Aluminum). The manufacturing of the detector by doping process induces the diffusion of Si from the strips and thus leads to increase the equivalent dead layer of Aluminum on the surface of the detector. The energy resolution (FWHM) for MUST2, adding all strips in the four detectors is 31 keV (see figure 3.8). A plot of energy versus strip for the four detectors is shown in figure 3.9a. A similar energy resolution of 30.9 keV is achieved for S1.

The energy alignement plot for S1 detector is shown in figure 3.9b. However, several pads were lost during the mounting of this detector namely 33, 34, 51, 52, 53 on the front-side of the detector and pads number 1, 14, 15, 16 on the back-side. Moreover, the pad number 13 next to the inoperational pads induced high-background noise. All the events related to these pads were not treated in the offline analysis. It was not possible to explain the noise visible in figure 3.9b at the energy range between 3 and 5 MeV. These events correspond to about 1.4 % of the whole run hence their effect is negligible. We can also

[4] In [Giro 11] the energy loss tables were extracted from LISE++ code, in this work we have used tables from SRIM.

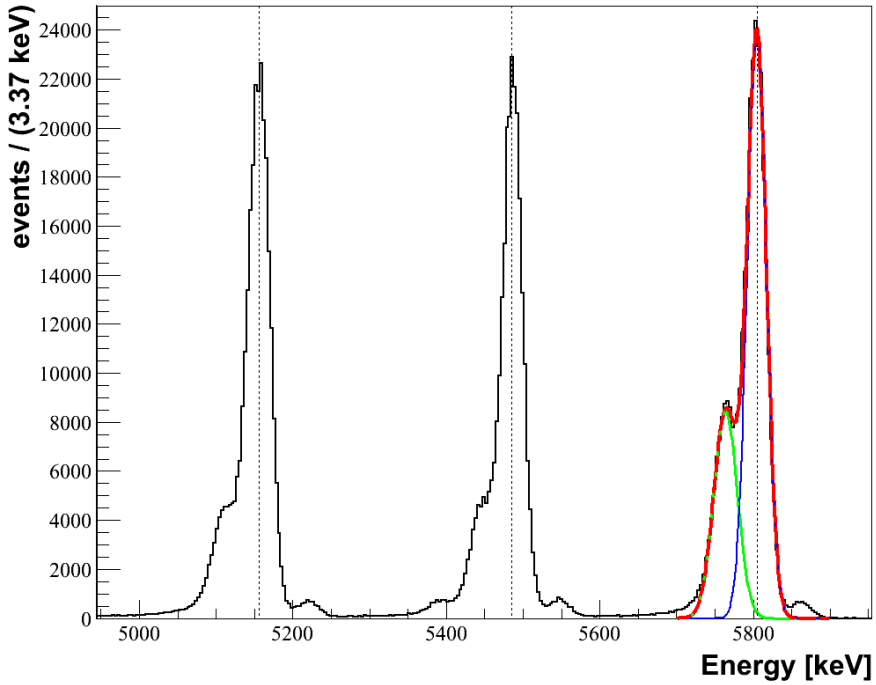

Figure 3.8: *The calibrated α-source spectrum fitted with gaussians taking into account the neighboring peaks.*

see a low counting rate from strip 33 to 48 (corresponding to the pads 1, 2, 15 and 16) where only one pad (2) out of four is working properly, and low counting from strip 1 to 16 (corresponding to the pads 11, 12, 13 and 14) where one pad (14) is inoperational.

3.2.2 Energy reconstruction

An emitted particle in the reaction will undergo energy losses and straggling in the target and in the detector dead layers before it will be detected by the DSSD. It can also trigger two strips when the particle crosses the interstrip zone. In this case the energy is divided between the contiguous strips. Table 3.6 summarizes multiplicities measured for a standard run.

A plot of the energy deposit on neighbouring X-strips (front-side) for multiplicity $2X$ events is shown in figure 3.10 for a calibration run with α source. The three lines correspond to interstrip events. The sum of energies on both strips restores the full energy of alpha particles. In the data analysis, events having a multiplicity > 1 are not considered. The particle energies are corrected for the energy losses in the Aluminum dead-layer covering the detector using tables from SRIM code and taking into account the effective thickness due to the incident angle of the particle. A similar correction was

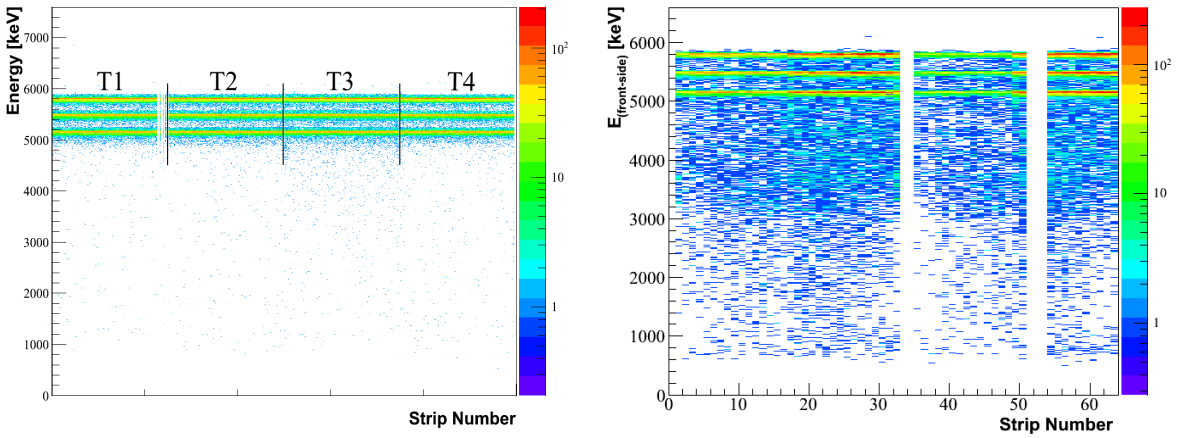

(a) (b)

Figure 3.9: *α-source energy versus front-side strip number in the DSSD of MUST2 (a) and S1 (b), respectively. One can see several strips missing in T1 and in S1.*

Telescope	Multiplicity 1X - 1Y	Multiplicity 2X - 1Y	Multiplicity 1X - 2Y	Multiplicity 2X - 2Y	Other
T1	81.9 %	7.5 %	7.9 %	1.7 %	0.8 %
T2	84.3 %	5.8 %	8.2 %	1.3 %	0.3 %
T3	85.8 %	5.1 %	7.4 %	1.0 %	0.56 %
S1	51.3 %	6 %	1.6 %	1.17 %	39.8 %

Table 3.6: *Hit multiplicities seen by each telescope. X and Y represent multiplicity on front-side and back-side of the DSSD, respectively. Contiguity of strips is required for events having multiplicity= 2.*

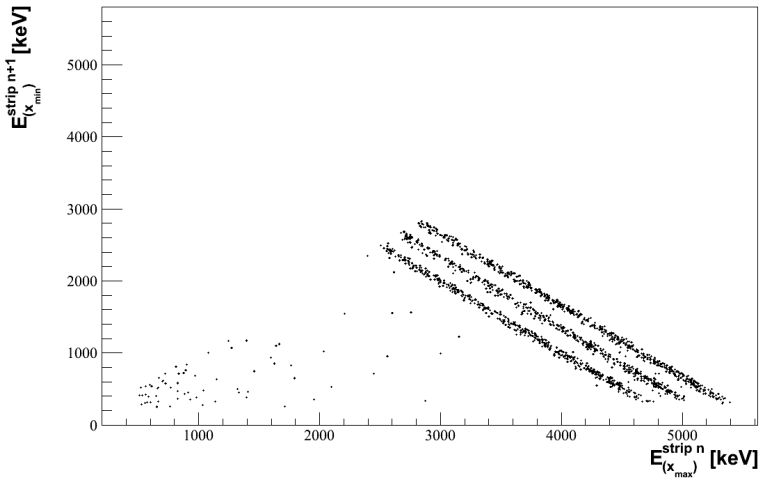

Figure 3.10: *Plot of the minimum deposited energy ($E^{n\pm1}_{x_{min}}$) versus the maximum deposited energy ($E^{n}_{x_{max}}$) on neighboring strips $n \pm 1$ and n, respectively. A multiplicity = 2 is required. For more explanation see text.*

applied for the energy loss inside the target. Since no parameter in the experiment can provide the depth of the reaction location in the target, we consider that all reactions take place in the target central plane.

3.2.3 Particle identification

The particles stopped in the first stage of MUST2 and S1 detectors can be identified using the ToF technique. The kinetic energy T of a particle is proportional to its mass M and to the square of its velocity v,

$$T \propto Mv^2 \tag{3.12}$$

The DSSD provides a measurement of the kinetic energy and since the distance traveled by particles is roughly the same, a measurement of the ToF between CATS and the DSSD is linearly related to the velocity of the particle. Plotting the energy against the ToF will give a set of hyperbolas that will determine the mass of the particle. Figure 3.11 shows the ToF *vs* energy spectrum for the particles detected in a DSSD. The proton hyperbola can be identifed by the maximum energy deposited in the DSSD, roughly equal to 6 MeV corresponding to the 300 µm thickness of the DSSD. The protons having greater energies will punch through the DSSD layer and will form the horizontal retrogression. The punch-through energy in a 300 µm of Si is given in table 3.7. In the same way we can identify the α-particle hyperbola, where the maximum deposited energy is $\approx$ 25 MeV.

Si thickness	p	d	t	^3He	^4He
300 µm	6.14	8.14	9.57	21.83	24.55
500 µm	8.28	11.03	13	29.38	33.09

Table 3.7: *Maximum energy loss in* MeV *of light-charged particles in* 300 *and* 500 µm *of Silicon*

The insert of figure 3.11 shows the same graph gated by the condition of detecting a heavy residue in the plastic scintillator placed at zero degrees with respect to the beam direction. Only the lines corresponding to protons and alphas remain (essentially), which makes the gate on the protons easier to set. The same spectrum is shown in figure 3.12 corresponding to S1. For both types of detectors, we can clearly distinguish the lines corresponding to the protons and alphas. On the contrary the lines for deuterons and tritons are not clearly separated. As can be seen in the insert of figure 3.12, requesting the heavy residue in coincidence tend to suppress the deuteron and triton contributions.

3.2.4 Time resolution

During the experiment, the internal time-of-flight provided by the MUST2 ASIC could not be exploited due to connectics problems. Instead, external TAC modules were used

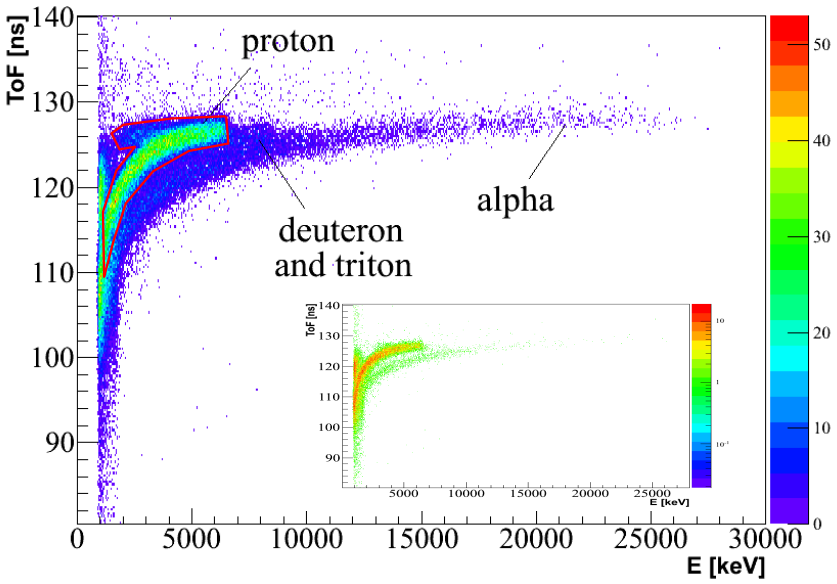

Figure 3.11: *Particle identification by $E-ToF$ technique in MUST2 first stage. The insert shows the $E-ToF$ spectrum when Ni isotops are requested in the plastic detector.*

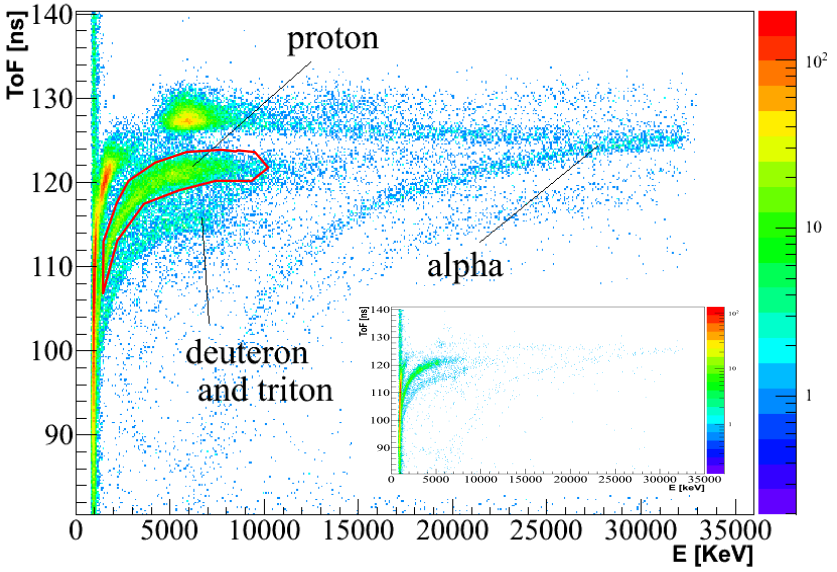

Figure 3.12: *Particle identification by $E-ToF$ technique in S1 detector. Proton, deuteron and alpha particles can be clearly identified by their maximum deposited energies in S1. The insert shows the $E-ToF$ spectrum when Ni isotops are requested in the plastic detector..*

to measure the time-of-flight of the detected particles. The time resolution (δt) was calculated for protons having 3 and 5 MeV after deconvolution from the δt_{CATS}(0.37 ns) timing response deduced earlier and were found to be equal to 1.57 ns and 1.43 ns, respectively. In the absence of correction from the time jitters, due to hit position on strip dependance and beam time-of-flight spread, these values do not correspond to the intrinsic resolution.

3.2.5 Silicium-Lithium Crystals : Energy Calibration

Calibration of Si(Li)-Jülich

Three of the four telescopes were equipped with Silicium-Lithium Crystals (Si(Li)) from the Jülich center. Calibration measurements were performed before installation of DSSD stage for the three telescopes equipped with Si(Li) using 3α source. The calibration of Si(Li) is of major importance since the kinematic line corresponding to the ground state lies mostly above 6 MeV.

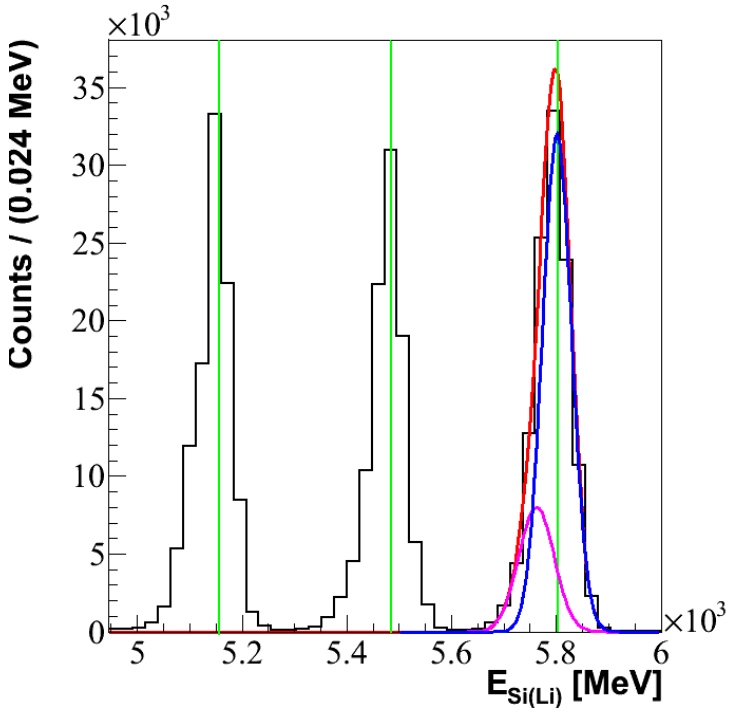

Figure 3.13: *Energy calibration of Si(Li). Spectrum for the 3-α source run after calibration with all pads added. The green vertical lines give the position of the 3 most intense energies of the used α source. We notice that the energy resolution is insufficient to resolve the less intense peaks.*

As in the case of the DSSDs, each pad is calibrated individually with the three most intense alpha peaks delivered by the α-source taking into account the pedestal positions, the dead layers and the neighboring less-intense peaks as shown in figure 3.13. A linear

relationship is also assumed between the channel number and the energy of the alpha particle deposited in the detector.

The dead layers of the Si(Li) crystals summarized in table 3.8 are obtained from [Giro 11] during another run of the campaign. They are determined in a similar way as for the DSSD. The energy resolution (FWHM) is 66 keV, which is two times greater than the first stage energy resoulution, all pads superposed. It is noteworthy to mention that the thickness of all dead layers of the detector (Boron implantation and ≈ 0.3 µm of Al) is given by the manufacturer to be equivalent to 1 µm of Si for all Si(Li) crystals. The thicknesses reported in table 3.8 are slightly lower than the value given by the manufacturer. The reason for this discrepancy may come from the manufacturing process. We have taken into account the values of table 3.8 in the offline analysis.

Si(Li)	crystal 1 (µm)	crystal 2 (µm)
T1	0.50	0.65
T2	1.00	0.50
T3	0.65	0.65

Table 3.8: *Silicon dead layer equivalent thicknesses for Si(Li) crystals in MUST2 telescopes.*

Calibration of Si(Li)-Orsay

One of the four MUST2 telescopes was equipped with a Si(Li) crystal from the detector department at IPN-Orsay. For the Si(Li) of this telescope we used standard analogic electronics (not by the MUFEE cards). Malfunctions of the detector were observed during the experiment. The observed statistics was much lower than for other telescopes and the $\Delta E - E$ identification curves were also anomalous. The data from this telescope are therefore not used in this analysis.

3.2.6 Energy reconstruction

Particles punching through the DSSD layer and detected in the Si(Li) crystal undergo energy losses in the aluminum back-layer of the DSSD and the Silicon dead layers on the surface of the Si(Li). Residual energies measured by the crystal are corrected in the same way as above taking into account the additional dead layers *i.e.* the back-window of the DSSD and the front window of the Si(Li). The back-window dead layers of the DSSD are assumed to be equal to those of the front-window given previously in table 3.5.

Particles passing between the two Si(Li) crystals, or grazing the borders of the DSSD will deposit less energy in the second stage of MUST2. Consequently their original energy can not be fully reconstructed, and leads to events lying below the real kinematic line. A Geometrical matching between the first and the second stage of MUST2 eliminates these

events. The matching is also important for events where the triggered pad in second stage does not correspond to the position of the triggered strips in the DSSD. Finally, the multiplicity of detected events is given in table 3.9. Events having a multiplicity > 1 are not considered.

Telescope	1 pad	2 pads	Other
T1	89.4 %	5.2 %	5.4 %
T2	95.3 %	4.3 %	0.3 %
T3	94.8 %	5.0 %	0.2 %

Table 3.9: *Multiplicity seen by the different telescopes in the Si(Li) stage.*

3.2.7 Particle identification

The particles crossing the DSSD and stopped in the Si(Li) are identified using the $\Delta E - E$ technique. According to Bethe and Bloch formula, the energy loss of a charged particle in a thin layer of material is proportional to the ratio,

$$\Delta E \propto \frac{AZ^2}{E} \tag{3.13}$$

where A, Z and E are the mass, the atomic number and the kinetic energy of the particle. Plotting $\Delta E\, vs\, E$ leads to a family of hyperbolas corresponding to the different values AZ^2 thus identifying firmly the detected particle. In our case the DSSD plays the role of a thin layer detector and will provide a measurement of ΔE while the Si(Li) will give the residual energy E. Figure 3.14 shows the result of performing identification by $\Delta E - E$ technique on the data in the hydrogen-isotopes region.

The mass lines corresponding to protons, deuterons and tritons are clearly well separated and the protons are selected unambiguously. Nonetheless, after the selection of heavy residues with the plastic detector placed at zero degrees the identified particles consist mainly of protons (see insert).

3.3 Identification of heavy residues

We saw in Chapter 2 that the ^{68}Ni beam was rather pure $\approx$ 85.8 %. The ionization chamber and the plastic scintillator were used to identify the heavy fragments from the reaction. However, the performance of the ionization chamber was not optimized for the identification of fragments with nominal intensity, *i.e.* $\approx 10^5$ *pps* and suffered from an important pile up rate.

Nevertheless, we performed a control run with low intensity to check the composition of the secondary beam. The energy loss in the ionization chamber (ΔE) versus the time-

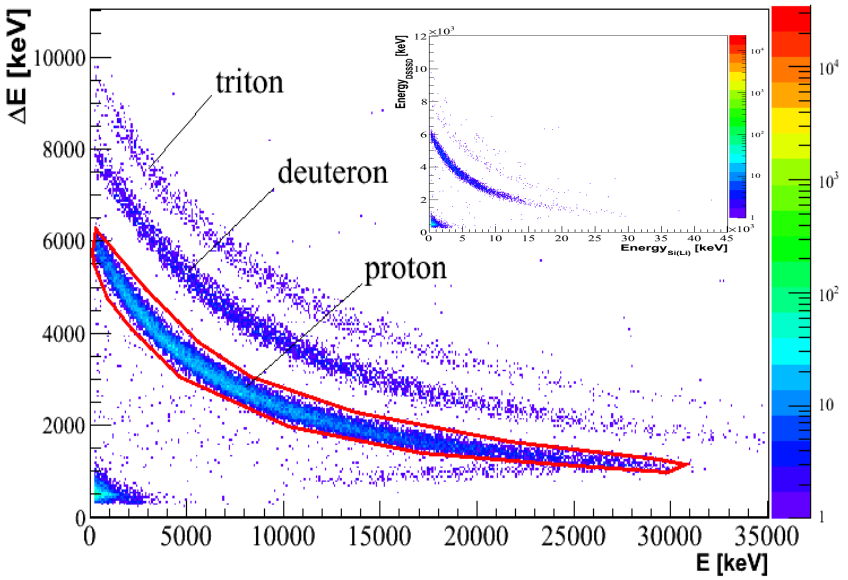

Figure 3.14: *Plot of E_{DSSD} vs E zoomed on the region of hydrogene isotopes. The three lines corresponding to protons, deuterons, and tritons are clearly separated. The insert shows the same spectrum when Ni isotops are requested in the plastic detector.*

of-flight between the microchannel plate[5] detector of LISE and the plastic scintillator is shown in figure 3.15a. The most intense spot was identified as ^{68}Ni representing 85.8 % of the beam intensity. The leftmost spot was identified as ^{70}Zn, the main contaminant, representing 8 % of the beam. The spot between ^{68}Ni and ^{70}Zn and the spot on the far right represent 2 and 3.8 % of the beam intensity, respectively. These spots were not identified.

The selection of ^{68}Ni is made by correlating the energy E in the plastic versus the time-of-flight CATS2-plastic as shown in figure 3.15b. During the experiment the plastic was damaged by the deposited energy of the beam and the efficiency of light transmission and collection has decreased which explains the migration of the spots downward in energy. The contour we have used takes into account the pile up events for energies in arbitrary units between 16.10^3 and 8.10^3 and those having less energy due to the plastic degradation.

3.4 Calculated parameters

In this section we will present the full reconstruction of a two-body reaction, and the calculations leading to the angle of emission of the light recoil and the excitation energy of

[5]Placed in chamber D4 of LISE between the second and the third magnetic dipoles see figure 2.5.

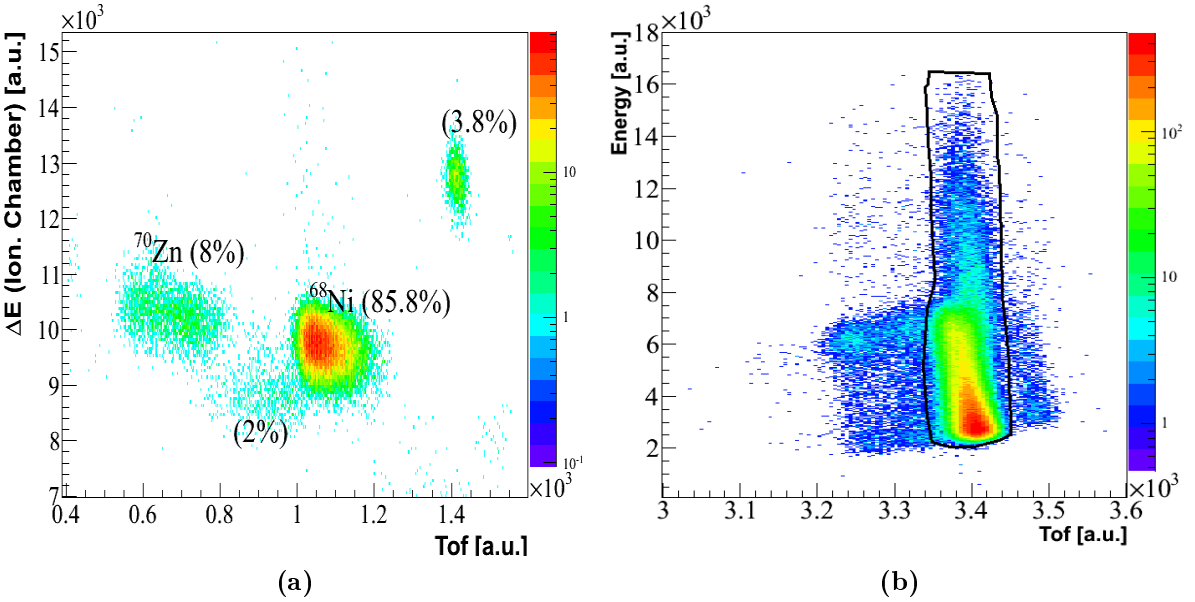

(a) (b)

Figure 3.15: *(a) Energy loss in the ionization chamber versus the time-of-flight in a low-intensity run. (b) Energy deposited in the plastic detector versus the time-of-flight (CATS2-plastic). The selection of ^{68}Ni is shown by the black contour.*

the heavy residue, using the beam-trackers CATS, and the light-charged particle detectors MUST2 and S1.

Before hitting the target the beam particle is detected by CATS1 and CATS2. These detectors provide two points $C_1 = (x_1, y_1, z_1)$ and $C_2 = (x_2, y_2, z_2)$ of the trajectory of the incident ion. Figure 3.16 shows the different positions of the beam trackers with respect to the target.

3.4.1 Reconstruction of event on target

In order to reconstruct the location of reaction in the plane of the target $C_t = (x_t, y_t, z_t)$, we first calculate the system of equations (Δ) of the ion trajectory in space. The direction vector $\overrightarrow{C_1C_2}$ is given by,

$$\overrightarrow{C_1C_2} = (x_2 - x_1, y_2 - y_1, z_2 - z_1) = (a, b, c). \tag{3.14}$$

Using the direction vector and a point C_1 we reconstruct Δ as,

$$\Delta \ : \ \begin{cases} x = a.m + x_1 \\ y = b.m + y_1 \\ z = c.m + z_1 \end{cases} \tag{3.15}$$

where the variables x,y and z represents any point on this trajectory. Knowing the position of the target z_t on the $z-axis$, the reaction location is calculated as the point of

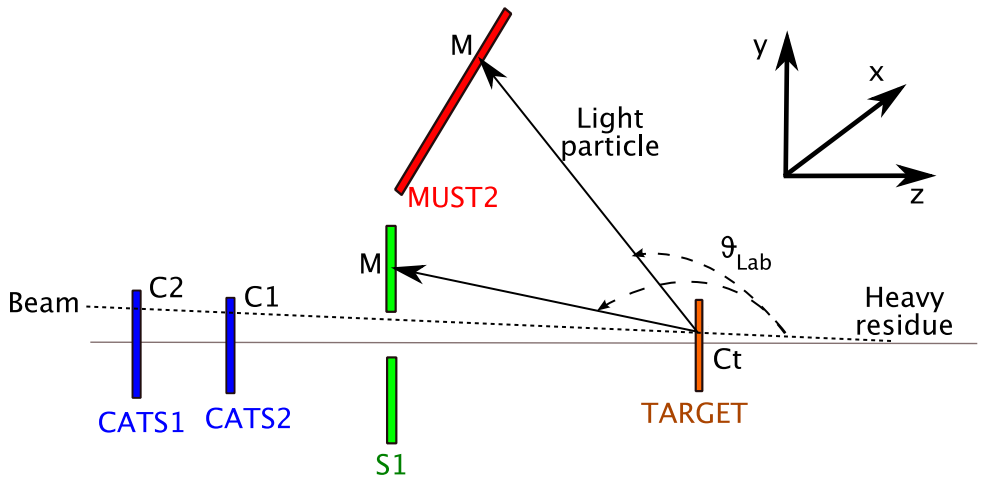

Figure 3.16: *A scheme of the setup showing how the angle of emission θ_{Lab} is calculated knowing the position of the beam in the beam trackers (C_1, C_2), the position of the target and the proton position (M) on MUST2 or S1 detectors.*

intersection between Δ and the plane $z = z_t$ as shown in figure 3.16. Solving this equation gives the m parameter,

$$z = z_t \Rightarrow m = \frac{z - z_1}{c} \tag{3.16}$$

which in turn leads to the reaction position with respect to x and y axis,

$$x_t = a\frac{z - z_1}{c} + x_1 \qquad y_t = b\frac{z - z_1}{c} + y_1 \tag{3.17}$$

The calculated point $C_t = (x_t, y_t, z_t)$ is the vertex of the angle of emission formed by $(\overrightarrow{C_1C_t}, \overrightarrow{C_tM})$. Next we will show how we calculate the point M on MUST2 and S1.

3.4.2 Reconstruction of event on MUST2 and S1

MUST2 and S1 detectors provide the location of a hit in terms of strip numbers. Since these detectors have different geometries, the hit location is calculated in two different ways. The position is first calculated in the local system of the detector, then it is transformed in the laboratory system.

MUST2 : The four corners of each MUST2 detector were measured by the geometer with respect to the target. We define these points in space as A, B, C and D. The strips numbering (from 1 to 128) starts from A as shown in figure 3.17a. The points A, B and D are used to establish an orthogonal-system $(\overrightarrow{w_x}, \overrightarrow{w_y})$ in the plane of a MUST2 detector, where :

$$\overrightarrow{w_x} = \frac{\overrightarrow{AD}}{128} \quad and \quad \overrightarrow{w_y} = \frac{\overrightarrow{AB}}{128} \tag{3.18}$$

Both of these vectors carry the information of the orientation of a MUST2 detector in space and the width of a strip of type x or y. Let S_x and S_y be the hitted strips. The hit

location with respect to A (the origin of the local system of the detector) is calculated as,

$$\overrightarrow{x_{local}} = (S_x - 0.5)\overrightarrow{w_x} \qquad \overrightarrow{y_{local}} = (S_y - 0.5)\overrightarrow{w_y}. \tag{3.19}$$

Finally, the trajectory of the detected proton is calculated as $\overrightarrow{C_tM}$ (*cf.* figure 3.16), where :

$$\overrightarrow{C_tM} = \overrightarrow{C_tA} + \overrightarrow{x_{local}} + \overrightarrow{y_{local}} \tag{3.20}$$

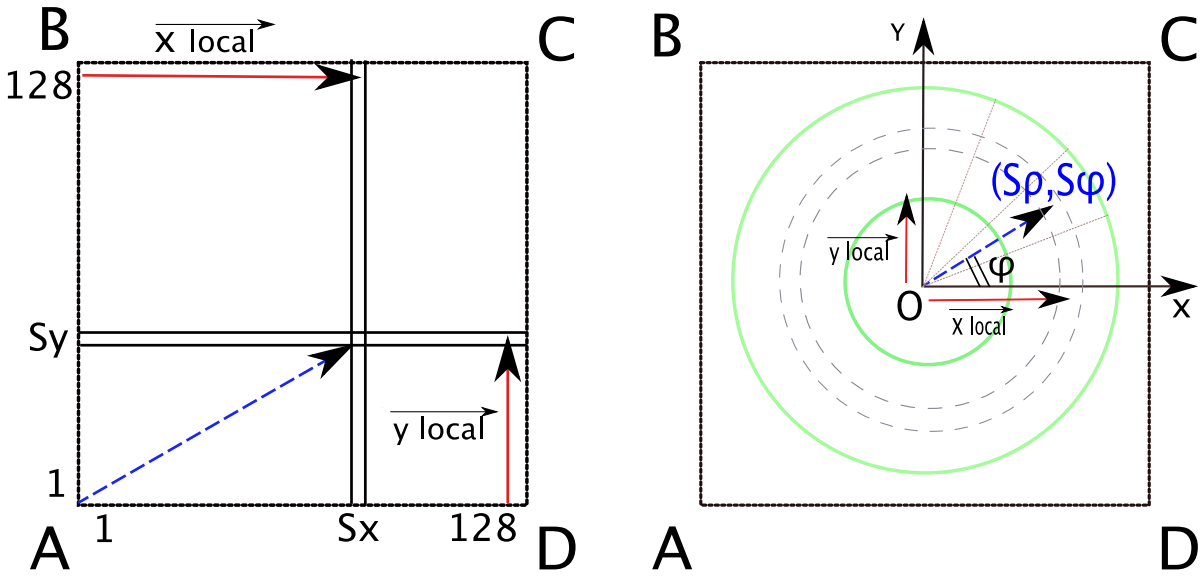

(a) **(b)**

Figure 3.17: *Reconstruction of the hit position with respect to the local sytem of MUST2 (a) and S1 (b) detectors.*

S1 : The annular detector S1 was fixed on a squared frame. The position of the four corners of the frame were measured by the geometer. The center of S1, O, is calculated as the barycenter of the four corners A, B, C and D (*cf.* figure 3.17b). The point O is considered as the origin of the local system of S1 $(O, \overrightarrow{u_x}, \overrightarrow{u_y})$. Radial and angular pitch of S1 were given by Micron [Micr 10],

$$w_\rho = 1.5 \text{ mm} \qquad w_\phi = 22.5°.$$

Let S_ρ and S_ϕ be the hitted strips[6] by a detected particle. We calculate the position in polar coordinates ρ_{local} and ϕ_{local} with respect to the origin O,

$$\rho_{local} = (S_\rho - 0.5)w_\rho \qquad \phi_{local} = (S_\phi - 0.5)w_\phi. \tag{3.21}$$

[6]The numbering of strips in S1 is originally dictated by the electronic connections, this was taken into account in order to get S_ρ and S_ϕ.

The hit position (M) in the local system is calculated using the following expressions :

$$\overrightarrow{x_{local}} = [\rho_{local}.cos(\phi_{local})]\overrightarrow{u_x} \qquad \overrightarrow{y_{local}} = [\rho_{local}.sin(\phi_{local}]\overrightarrow{u_y} \tag{3.22}$$

Finally, the same procedure is applied, as in the case of MUST2, to calculate the trajectory of the detected proton, where,

$$\overrightarrow{C_tM} = \overrightarrow{C_tO} + \overrightarrow{x_{local}} + \overrightarrow{y_{local}} \tag{3.23}$$

Having the location of the reaction on the target C_t and the hit-position M on MUST2 or S1, we can calculate the angle of emission θ_{Lab} using the expression,

$$cos^{-1}[cos(\theta_{Lab})] = cos^{-1}\left\{\frac{\overrightarrow{C_1C_t}\cdot\overrightarrow{C_tM}}{\|\overrightarrow{C_1C_t}\|\ \|\overrightarrow{C_tM}\|}\right\} \tag{3.24}$$

3.4.3 Excitation energy

In this section we show how we calculate the excitation energy of the heavy-residue in the $d(^{68}Ni, p)^{69}Ni$ reaction. Figure 3.18 depicts a two-body reaction in inverse kinematics, where the different particles are defined as,

1. Particle (1): the incident ^{68}Ni,
2. Particle (2): the deuteron in CD_2 target,
3. Particle (3): the heavy-residue ^{69}Ni,
4. Particle (4): the recoiling proton.

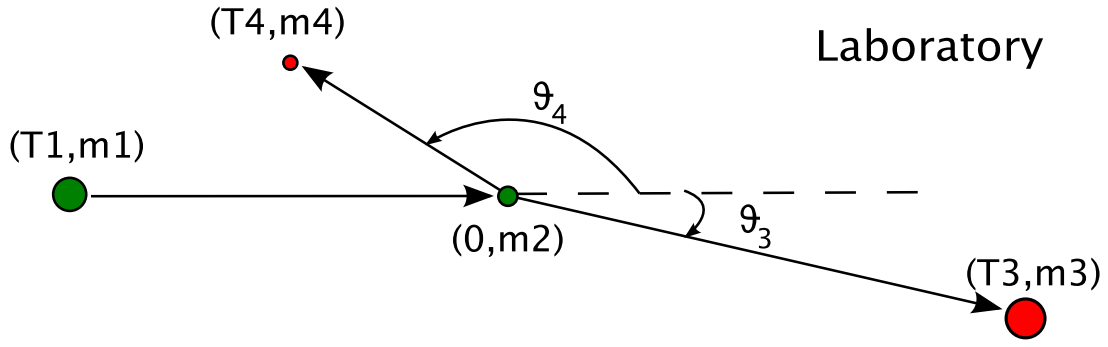

Figure 3.18: *Scheme of a reaction in inverse kinematics in the Laboratory system of reference. The masses m1, m2, m3 and m4 correspond to the beam, target, heavy residue and light recoil emitted in the backward angles, respectively.*

We define T_i, p_i, m_i, and $E_i = T_i + m_i = \sqrt{p_i^2 + m_i^2}$ as the kinetic energy, linear momentum, mass and total energy of particle (i), respectively. The excitation energy is

calculated using the conservation laws under the missing mass method. All particles involved in this reaction are in their ground state except ^{69}Ni that could be in an excited state. In this case the excitation energy E_3^{exc} is calculated using,

$$E_3^{exc} = m_3 - m_3^0 \tag{3.25}$$

where m_3^0 is the mass of ^{69}Ni it its ground state. Starting with the conservation law of linear-momentum we have,

$$\overrightarrow{p_1} + \overrightarrow{p_2} = \overrightarrow{p_3} + \overrightarrow{p_4} \tag{3.26}$$

Since the deuteron is at rest, $\overrightarrow{p_2} = \overrightarrow{0}$ and p_3 is calculated in terms of $p_{1,4}$ as,

$$p_3^2 = p_1^2 + p_4^2 - 2p_1p_4cos(\theta_4) \tag{3.27}$$

The experiment provides T_1, T_4 and θ_4 of the incident ion and the proton which are used to calculate the linear momenta p_1 and p_4 using the following equation,

$$p_i^2 = T_i^2 + 2\,T_i\,m_i \tag{3.28}$$

The energy conservation law gives,

$$E_1 + E_2 = E_3 + E_4 \Rightarrow E_3 = E_4 - E_1 - E_2 \tag{3.29}$$

By replacing $E_{1,2,4}$ by $(T_{1,2,4} + m_{1,2,4})$ and E_3 by $\sqrt{p_3^2 + m_3^2}$ in the above equation leads to,

$$m_3^2 = [(T_1 + m_1 + m_2) - (T_4 + m_4)]^2 - p_3^2 \tag{3.30}$$

Knowing p_3^2 from 3.27, we calculate m_3^2 and we deduce E_3^{exc} from equation 3.25.

3.5 Differential cross sections

Two main informations can be obtained from the differential cross sections. The shape of the angular distribution depends on the transferred angular momentum, and thus it can be used to determine the latter value. Another important information is the spectroscopic factor which is deduced from the experimental differential cross section using a normalization procedure described in chapter 4.

The differential cross section of the $^{68}Ni(d,p)$ reaction, measured in the laboratory system, is given by the following expression,

$$\frac{d\sigma}{d\Omega_{Lab}}(\theta_{Lab}) = \frac{N_{det}(\theta_{Lab})}{N_{Beam}N_{Target}\Delta\Omega(\theta_{Lab})} \tag{3.31}$$

where,

1. $N_{det}(\theta_{Lab})$ represents the emitted particles, at an angle (θ_{lab}), detected by MUST2 and S1. Since these detectors cover only a fraction of the solid angle at backward angles, a correction factor $\varepsilon_{MUST2,S1}(\theta_{Lab}) = \varepsilon_{geom}(\theta_{Lab})$ must be introduced into the above expression,

2. N_{Beam} is the number of ^{68}Ni in the beam impinging on the target and detected by the beam trackers CATS and the plastic scintillator,

3. N_{Target} is the number of deuterons per cm^2 in the target and is calculated by the following expression :

$$N_{Target} = \frac{2eN_{avogadro}}{M_{Carbon} + 2M_{Deuteron}} \tag{3.32}$$

where :

(a) e is the target thickness in g/cm^2,

(b) M_{Carbon} and $M_{Deuteron}$ are the molar masses of Carbon and Deuteron, respectively, in g/mol,

4. $\Delta\Omega(\theta_{Lab})$ is the solid angle at angle θ_{Lab} and is equal to $2\pi sin(\theta_{Lab})\Delta\theta_{Lab}$.

Finally, the detection system may be totally unefficient and particles passing through any detector are not detected. This corresponds to the electronics deadtime. It will be represented by the parameter $\varepsilon_{DeadTime}$ which is defined as the percentage of time during which the system cannot accept an event.

Including all the effects, the differential cross section expression 3.31 becomes,

$$\frac{d\sigma}{d\Omega_{Lab}}(\theta_{Lab}) = \frac{N_{det}(\theta_{Lab})\,(1 + \varepsilon_{DeadTime})}{N_{Beam}\,N_{Target}\,\Delta\Omega(\theta_{Lab})\,\varepsilon_{geom}}. \tag{3.33}$$

The differential cross section is calculated in the laboratory system and must be expressed in the center-of-mass system (CM) in order to be compared to the calculated cross sections. The conversion is done using the following relation,

$$\frac{d\sigma}{d\Omega_{CM}}(\theta_{CM}) = J(\theta_{Lab})\frac{d\sigma}{d\Omega_{Lab}}(\theta_{Lab}) \tag{3.34}$$

where :

1. θ_{CM} is the angle of emission in CM,

2. $J(\theta_{Lab})$ the Jacobian as a function of θ_{Lab}.

The Jacobian is a purely kinematic term. Using the same notation as in section 3.4.3, where θ_4 is represented by θ_{Lab}, the Jacobian is expressed in terms of θ_{Lab} as [Mich 64],

$$J(\theta_{Lab}) = [\Gamma^2(cos(\theta_{Lab}) - K) + sin^2(\theta_{Lab})]^{1/2} \cdot \Gamma(1 - Kcos(\theta_{Lab})$$

where,

$$K = \frac{B}{\beta_4}$$

and

$$\Gamma = \frac{1}{\sqrt{1-B^2}}$$

β_4 and B are calculated directly using the known masses and measured energies as :

$$\beta_4 = \sqrt{1 - \frac{m_4^2}{m_4^2 + T_4^2}},$$

and

$$B = \frac{p_1 + p_2}{E_1 + E_2} = \frac{p_1}{T_1 + m_1 + m_2}$$

3.6 Geometrical efficiency and angular ranges

Special care is devoted to the selection of angular ranges. The charged-particle detectors (MUST2 and S1) do not cover all the backward angles with the same geometrical efficiency $\varepsilon_{geom}(\Delta\theta)$. The latter is used as a correction factor for the detected number of events.

$\varepsilon_{geom}(\Delta\theta)$ depends on the geometry of light-charged particle detectors and the energy range considered especially for events detected in MUST2. In this case, the hits corresponding to the spacing between the two Si(Li) crystals or even between two interpads of the same crystal are not considered during the analysis(see section 3.2.6) and they are removed in the calculation of the geometrical efficiency.

Another parameter which must be taken into account is the position of the defective strips (pads) that have not been operational during the experiment. In the case of S1 detector 4 out of 16 sectors in total were lost during the mounting of the detectors. Table 3.10 summarizes the numbers of defective strips (pads) during the experiment.

Detector	DSSD	Si(Li)
T1	X(12), X(116-127) / Y(5)	pad(6)
T2	X(12) / Y(16)	
T3	X(12) / Y(-)	
T4	X(all) / Y(all)	pad(all)
S1	T(33-34), T(51-53) / P(1), P(13-16)	-

Table 3.10: *Defective strips (pads) during E507 experiment.*

The geometrical efficiency of the detection system is estimated by a Monte-Carlo simulation developped in this work and explained in Appendix A. The simulation takes into account the positions of the MUST2 and S1 detectors in space and simulates an isotropic emission of a particle source located at the target position. The geometrical efficiency ($\varepsilon_{geom}(\theta_{Lab})$) for a given angle θ_{Lab} was calculated as,

$$\varepsilon_{geom}(\theta_{Lab}) = \frac{N_{det}^{simu}(\theta_{Lab})}{N_{tot}^{simu}(\theta_{Lab})} \tag{3.35}$$

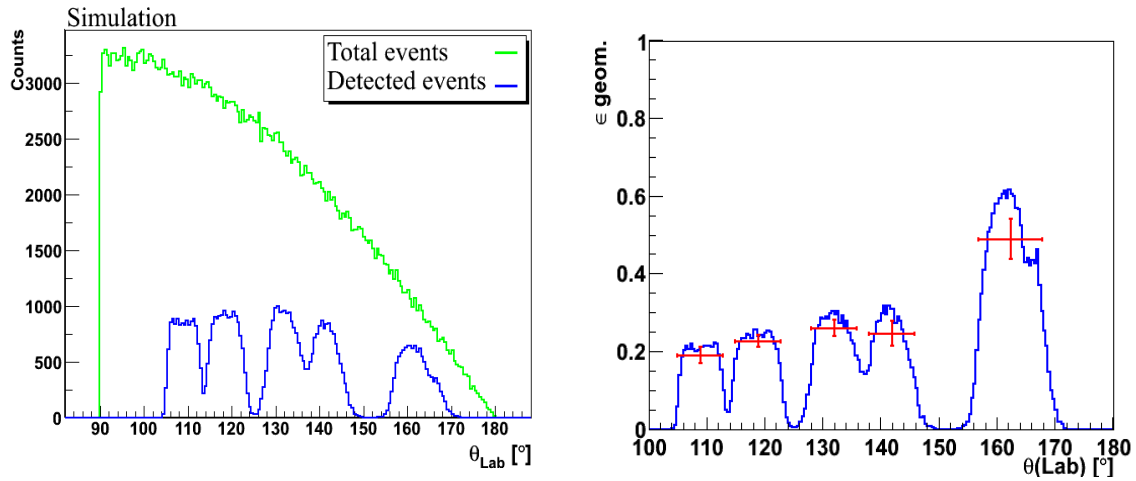

(a) (b)

Figure 3.19: *The histograms are obtained from simulated data. (a) The green line shows the total emitted particles, from an isotropic source in the laboratory-reference system placed at the target position. The histogram in blue represents only the detected particles by the detection system placed in the backward angles.(b) Histogram showing the ratio of detected events over total number of events for each bin. The ratio gives the geometrical efficiency of the detection system. The horizontal bars in the red crosses correspond to the angular ranges used in the analysis while the vertical bars represent the error on the calculated efficiency.*

where, $N_{det}^{simu}(\theta_{Lab})$ is the number of events hitting a working strip (pad) and $N_{tot}^{simu}(\theta_{Lab})$ is the total number of events emitted by the source. The result is given in figure 3.19. Five angular ranges are adopted and the $\varepsilon_{geom}(\theta_{Lab})$ value is averaged in each angular range $\Delta\theta = \theta_2 - \theta_1$,

$$\varepsilon_{geom}(\Delta\theta_{Lab}) = \frac{\int_{\theta_1}^{\theta_2} \varepsilon_{geom}(\theta_{Lab}) d\theta_{Lab}}{\int_{\theta_1}^{\theta_2} d\theta_{Lab}} \tag{3.36}$$

Finally, the number of particles detected in the real data is corrected accordingly to the following expression,

$$N_{tot}^{data}(\Delta\theta_{Lab}) = \frac{N_{det}^{data}(\Delta\theta_{Lab})}{\varepsilon_{geom}(\Delta\theta_{Lab})} \tag{3.37}$$

We have shown in this chapter how the data from experiment $E507$ are analyzed and how we calculate all the parameters of interest. The next chapter will be devoted to the extraction of excitation-energy spectra for the $d(^{68}Ni, p)$ reaction and the associated differential cross-sections will be presented and analyzed. The obtained results will be compared to shell-model calculations.

Chapter 4

Study of ^{69}Ni via (d,p) reaction

In this chapter, the structure of the ^{69}Ni nucleus is studied via the one-neutron transfer reaction

$$^{68}Ni + d \rightarrow p +^{69} Ni. \tag{4.1}$$

As discussed earlier the transfer of one neutron will select naturally the neutron single-particle orbitals to be populated in ^{69}Ni. The energy of these levels can be deduced from the energy and the emission angle of the light recoil particle, the proton, and their angular momentum from an analysis of the corresponding differential cross-section.

In the first section, the different gates used to select the reaction of interest are recalled and the excitation energy spectra are shown. The contribution of background reactions are evaluated in order to be subtracted leading to the final excitation energy spectrum presented in the second section. The third section is devoted to the analysis of the excitation energy spectra. The identification of the observed states and the extraction of their angular momentum and spectroscopic factor on the basis of DWBA analysis are presented in the fourth section. In the last section we discuss the discovered states in ^{69}Ni and their interpretation within the shell-model approach.

4.1 Event Selection and excitation energy spectra

The excitation energy spectrum was obtained using the "missing mass" method described in section 3.4.3. The ungated (no filter on any parameter) kinematical plot and the associated excitation energy spectrum is given in figure 4.1. The cutoff near 22 MeV corresponds mainly to an energy threshold due to the limited geometry of the detection system. The counts at negative excitation energies are due to other reactions treated with the kinematics of the reaction of interest $d(^{68}Ni, p)$ in the analysis code. The two broad peaks at $E_{Exc} \approx 16$ and 18 MeV correspond to recoil products (protons and others) and all other sources of noise in the detectors corresponding to deposited energies less than 1.5 MeV. We can already see a peak at 0 MeV corresponding to the ^{69}Ni ground state emerging from the reaction background . In order to extract a clean excitation energy spectrum related to the reaction of interest, several gates were made. The main gates are:

1. the CD_2 area impinged by the beam,
2. the proton identification in the light-charged particle detectors placed in the backward angles using $\Delta E - E$ and $ToF - E$ techniques,

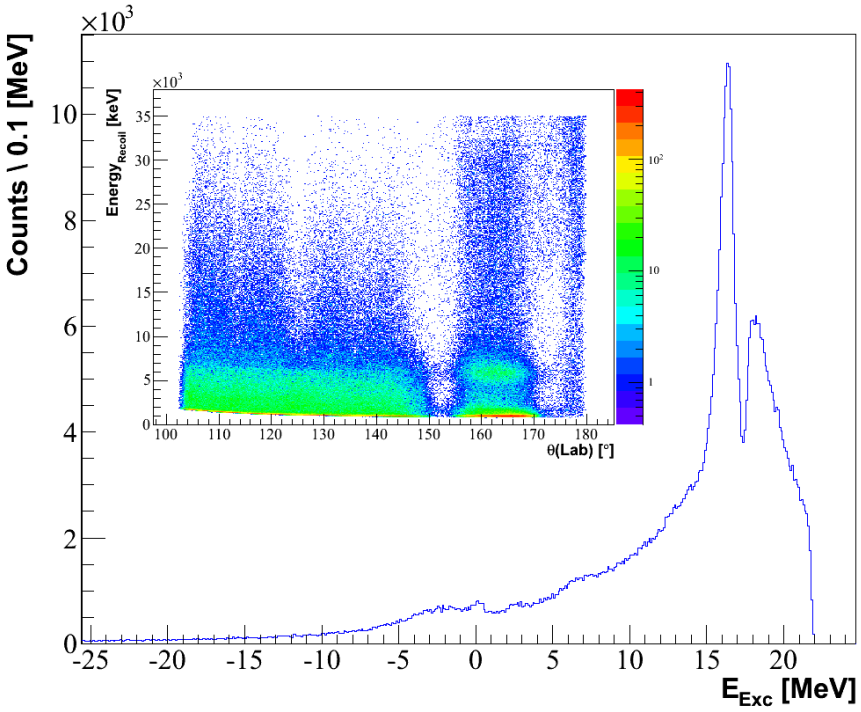

Figure 4.1: *Excitation energy spectrum without any selection. In the insert, the kinematical plot (Energy vs θ) of the recoil particle.*

3. the Ni isotopes identified in the plastic scintillator using the $ToF - E$ technique.

Figure 4.2 shows the kinematic plot after applying the aformentioned selections. The plot is significantly cleaned with respect to the insert in figure 4.1. One can see clearly two kinematic lines corresponding to the ground state and a first excited state around 2.5 MeV (figure 4.2 (b)).

Figure 4.3 shows the excitation energy spectrum as a function of the different selections presented above. In frame (a) we have applied only the selection on the beam spot on target. The general trend of the spectrum did not change relative to figure 4.1, nevertheless, we notice a significant lowering ($\approx 66\%$) of the statistics.

The same spectrum is shown in frame (b) after applying only the selection on the heavy residue. Counts at negative excitation energies are strongly reduced. The ground state is more pronounced and a slight bump at an excitation energy around 2.5 MeV is visible. However, the two peaks around 16 and 18 MeV due to recoil particles having energies less than 1.5 MeV persist.

In frame (c) the excitation spectrum gated by protons in MUST2 and S1 detectors is shown. The aforementioned two peaks are completly removed. The ground-state and an excited state of ^{69}Ni are clearly visible. However, the proton gate is unable to reduce the background responsible of the negative excitation energies due to other reactions. The spectra (a), (b) and (c) demonstrate the necessity of having the three selections

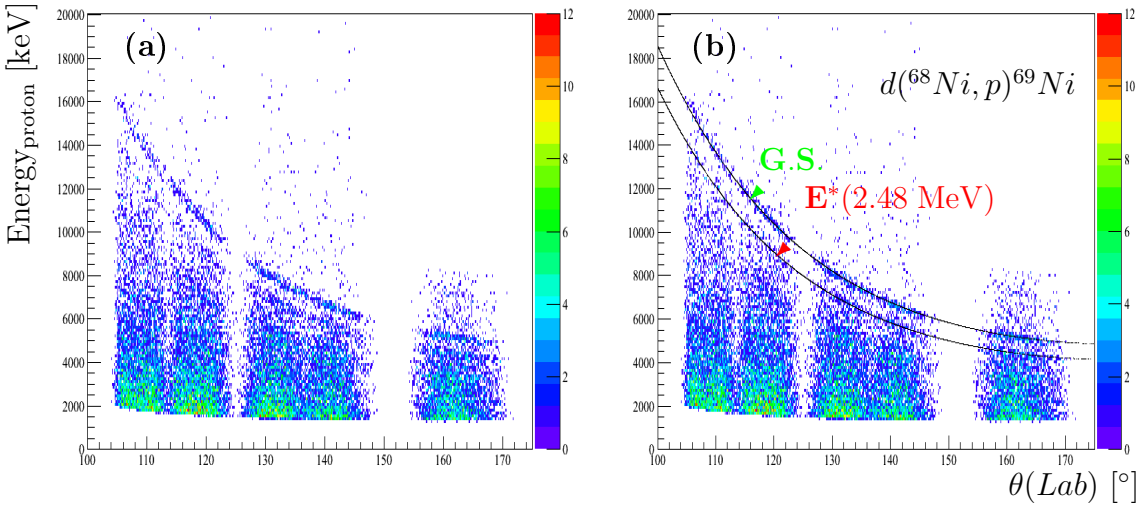

Figure 4.2: *(a) Kinematic plot after selecting the beam spot on the target, the protons in the silicon detectors and the Ni isotopes in the plastic scintillator. Two kinematic lines corresponding of the reaction of interest $d(^{68}Ni,p)^{69}Ni$ are clearly discernible. (b) The same kinematic plot after superimposing the calculated kinematic lines of the ground state (G.S.) and an excited state at $E^* = 2.48$ MeV (cf. section 4.3).*

simultaneously. Frame (d) shows the excitation energy spectrum with the three gates combined. As expected, the ground state and an excited state at 2.5 MeV are well pronounced. Moreover, structures emerge as a shoulder and a bump at about 4 MeV and $6-7$ MeV, respectively. The neutron separation energy (S_n) is marked by a dashed line at 4.59 MeV. Above this energy a background contribution from deuteron breakup is expected. We have also marked the separation energies of two neutrons (S_{2n}) and one proton (S_p) at 12.38 MeV and 15.36 MeV, respectively. Clearly a high density of states is visible for excitation energies above S_n. We can also notice the persistence of the negative excited energies, mainly due to the Carbon background.

The data were analyzed in six angular ranges, chosen accordingly to the geometrical efficiency of the detection system (see section 3.6). In the next section, we will show how reaction backgrounds, *i.e.* Carbon background and deuteron breakup, are subtracted from the excitation energy spectrum in order to extract spectroscopic informations up to 8 MeV.

4.2 Background reactions

The background, up to excitation energies of about 8 MeV, comes mainly from two origins that will be treated separately in the following paragraphs.

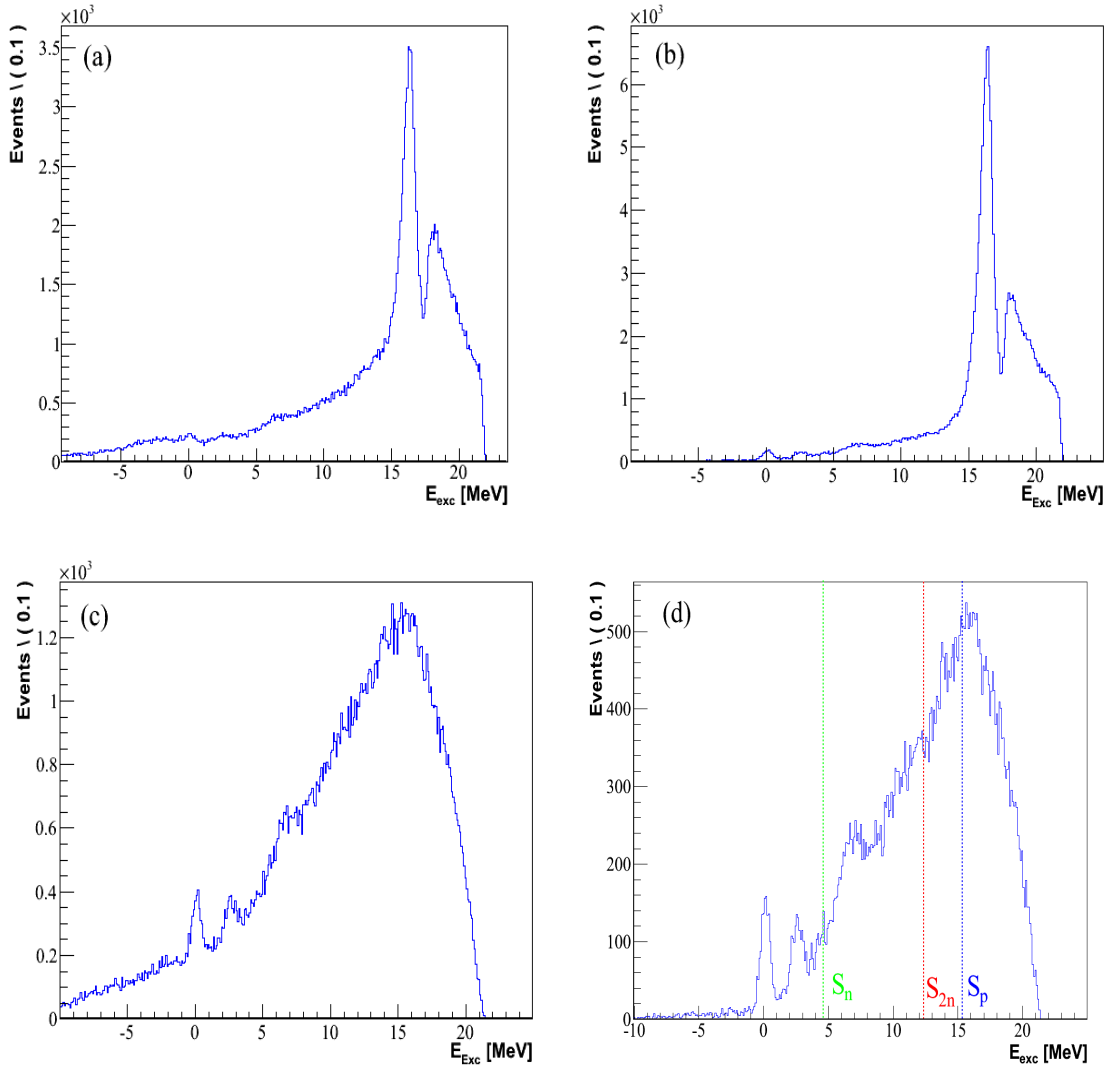

Figure 4.3: *Excitation energy spectrum gated with the selection of: (a) the beam spot on the target, (b) ^{68}Ni in the plastic scintillator, (c) protons in MUST2 and S1, (d) the three aforementioned selections combined.*

4.2.1 Carbon background

In order to estimate the background due to Carbon in the target, the CD_2 target (2.6 mg/cm^2) is replaced by a pure C target of 2 mg/cm^2. The resulting data are analyzed with the same procedure as the data from the CD_2 target. Their related excitation energy spectrum provides the spectrum of the Carbon background component that can be normalized and subtracted from the excitation energy spectrum from the CD_2 target. Unfortunately, the Carbon background can not be rigorously determined due to poor statistics. Alternative methods are used to overcome this difficulty. The first method consists in fitting the negative part of the excitation energy spectrum by a linear function. The extension of the fitted line to the positive energy part would give an estimation of the Carbon background component. The disadvantage of this method is that the estimated background increases continuously with increasing excitation energy while even with poor counting rate we can observe that the Carbon background is peaked around 15 MeV before decreasing down to zero around 22 MeV (see figure 4.4).

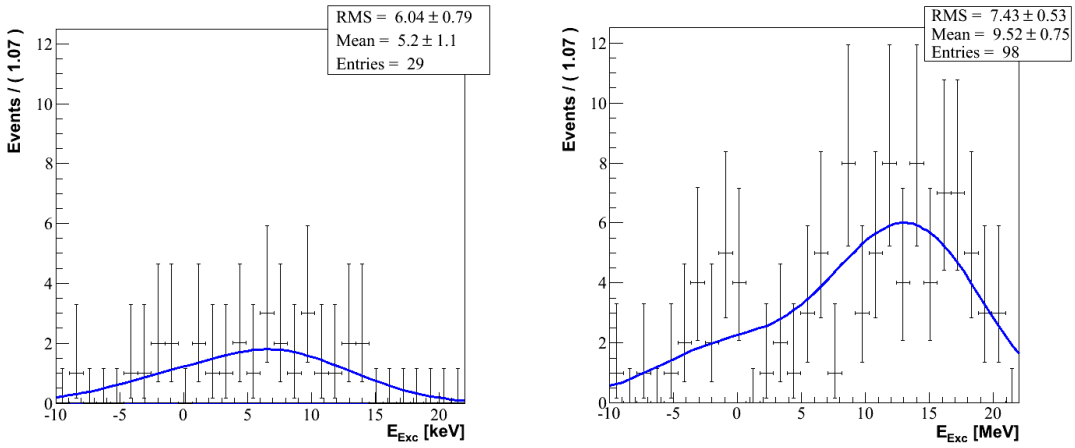

(a) (b)

Figure 4.4: *Probability density function associated to the low-statistics Carbon-background run of E507 in S1 detector (a) and MUST2 detector(b)*

The second method is *kernel density estimation* [Parz 62] which is a non-parametric way of estimating the probability density function of a random variable. The result on the Carbon background spectrum is illustrated in figure 4.4. This method is found in the C++ library "ROOFIT" [Verk 03] from data-analysis framework ROOT. It is adapted to extract a probability density function from a low-statistics histogram. Figure 4.5 depicts the two different methods. Both methods are roughly equivalent for excitation energies less than 5 MeV. At higher excitation energies the straight line underestimates the background up to $\approx$ 16 MeV.

The reactions on Carbon could explain the background in the excitation energy spectrum up to 4.59 MeV, the neutron separation energy (S_n). At higher excitation energies

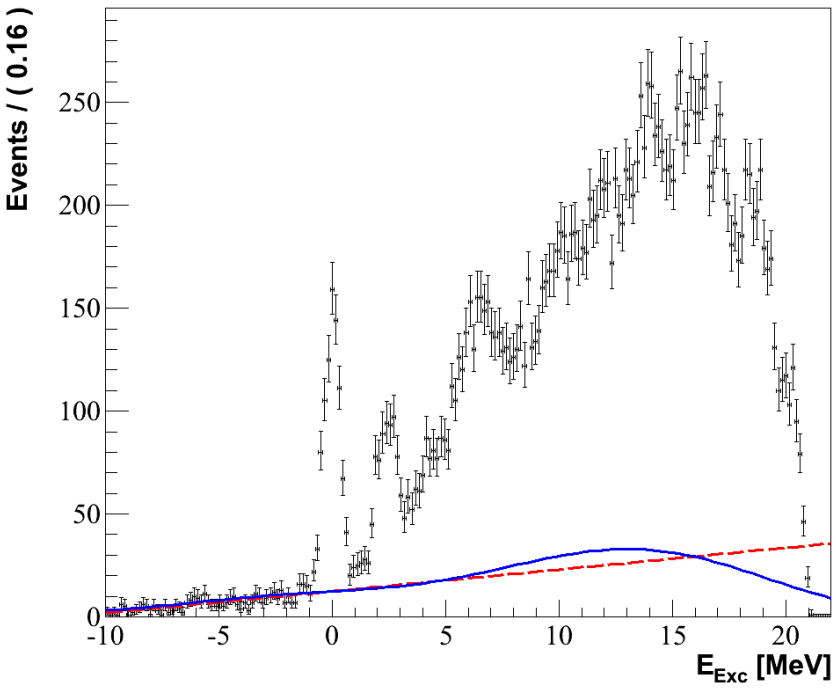

Figure 4.5: *Carbon background contribution to the excitation energy spectrum. Straight line fitted in the* -10 *to* -1 MeV *negative excitation energy range and extrapolated to the positive energies to estimate the Carbon background empiricaly (dashed red line). Probability density function associated to the low-statistics Carbon-background run of E507 experiment (blue line).*

another source of contamination, the deuteron break-up, contributes to the background in the excitation energy spectrum.

4.2.2 Deuteron break-up

Deuteron is a weakly bound nucleus which easily undergo break-up. In our case the considered break-up reaction is given by

$$^{68}Ni + d \rightarrow ^{68}Ni + p + n \tag{4.2}$$

The proton from this reaction can then be detected in MUST2 and S1 and its associated spectrum would interfer with the reaction of interest. We did not have access to the energy distribution of these protons due to the deuteron break-up, as was the case for the fragments due to reactions on Carbon nuclei in the CD_2 target. An alternative method had to be used to estimate its contribution to the excitation energy spectrum.

In contrast with the reaction of interest, this reaction leads to three particles in the exit channel and for a complete description of its kinematics we make use of phase-space calculations. In such calculations every degree of freedom or parameter of the system (such as the number of products, their masses and their momenta) is represented as an axis of a multidimensional space, and all possible states are regarded as unique point.

However, this type of calculations is rather difficult to solve analytically if not impossible. Nevertheless an estimation of the proton background produced by this reaction is possible using numerical methods of Monte-Carlo type.

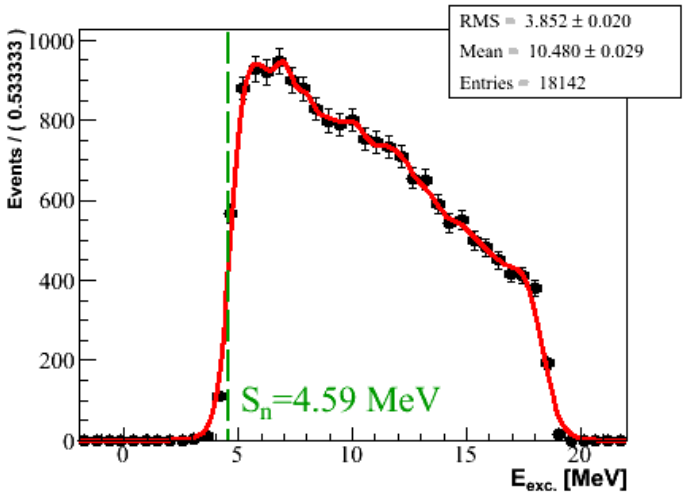

Figure 4.6: *Simulated excitation energy spectrum of the detected protons from deuteron break-up. The spectrum starts slightly before the neutron separation energy due to the detector resolutions.*

A special class in ROOT analysis frame work "TGenPhaseSpace" is intended to do phase-space calculations. After fixing the number of particles and their masses, this class generates a combination of three quadri-vectors corresponding to the three fixed masses and satisfying the conservation laws of energy and momentum determined by the input channel. The proton quadrivectors are then injected in the simulation and the *detected* protons are stored and then analyzed identically to real data. With this procedure the simulated background includes the response function of the experimental setup such as energy resolution and detection efficiency. The spectrum in figure 4.6 shows the result of these calculations. The contribution of the deuteron break-up to the total reaction background starts slightly above 4 MeV, which is consistent with the neutron separation energy which in our case is equal to 4.59 MeV. A non-parametric distribution based on kernel density estimation is used to estimate this background (red line in figure 4.6).

4.3 Energy levels and resolution

The total excitation energy spectrum presented in section 4.1 shows a pronounced ground state and some structures below and above S_n (=4.59 MeV). excitation energy spectra are analyzed for several angular ranges chosen accordingly to the geometrical efficiency of the detection system as mentioned in section 3.6.

The angular range in the most backward angles ($156°-170°$) covered by the S1 detector is taken as reference for several reasons:

- The excitation energy is less sensitive to the angular resolution. As can be seen in figure 2.1, the kinematical curves flatten at backward angles so that the extracted

excitation energy depends essentially on the proton energy and is less subject to incorrect scattering-angle reconstruction.

- The contribution of the deuteron break-up is minimum,
- The transfer cross sections are at their maximum and excited energies around S_n are more pronounced.

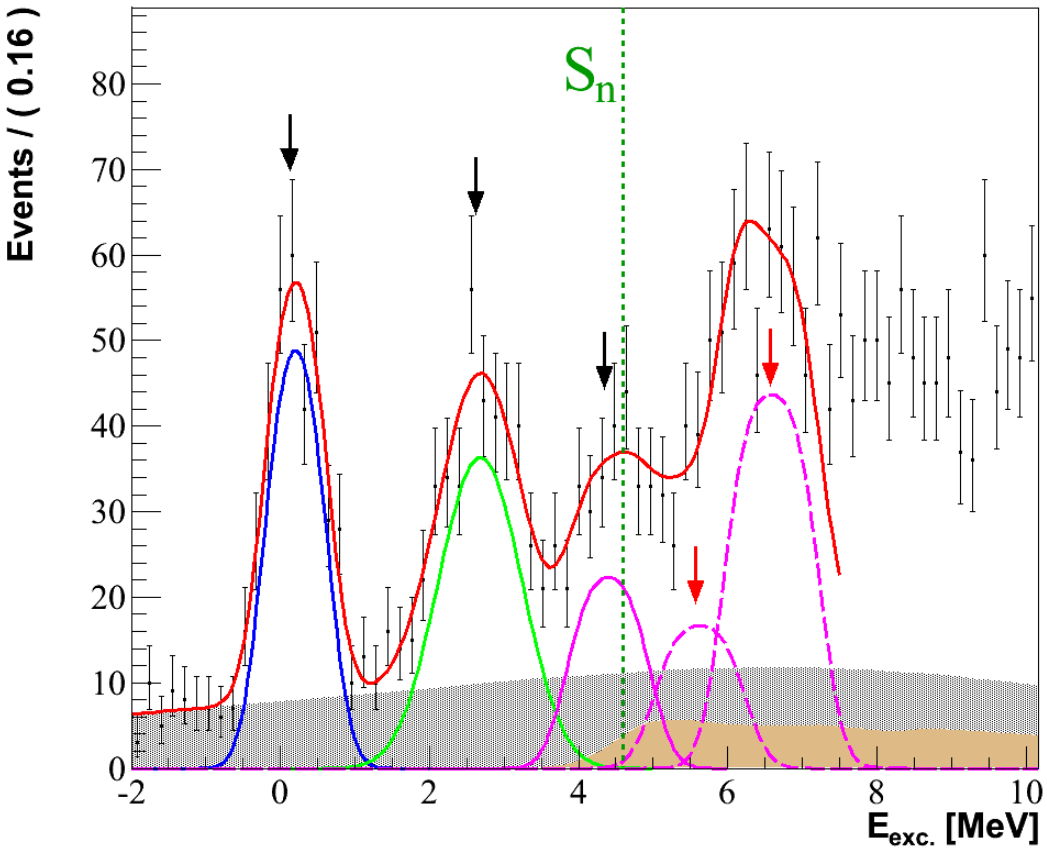

Figure 4.7: *The excitation energy spectrum seen by the S1 detector and corresponding to the angular range* $[156° - 170°]$ *taken as the energy reference. Bound (unbound) states are marked by black (red) arrows. The green dashed line marks the neutron separation energy* (S_n).

The excitation energy spectrum corresponding to this angular range is shown in the left frame of figure 4.7. Three energy levels including the ground state are clearly visible and marked by black arrows. We can also distinguish several states above the neutron separation energy (marked with a green dashed-line). The broad structure around $6 - 7$ MeV is tentatively attributed to a doublet of resonances. We note that at these excitation energies, single particle state can be quite broad due to coupling to core (^{68}Ni in our case) excitations [Gale 88]. At higher excitation energy the larger density of states makes obviously the decomposition more difficult.

Figure 4.7 shows the result of the fit up to 8 MeV. The fit provides the peak centroids used later in the DWBA analysis. The fit parameters for this angular range are adjusted under the following conditions:

- The fit is made with ROOFIT using the Maximum Likelihood algorithm since it is more suitable for low-statistics spectrum fitting,

- The Carbon background is normalized on the negative part taking into account simultaneously the fit for the ground state ($[-2$ MeV $- +1$ MeV$]$) of the excitation energy spectrum.

- Bound states are fitted by the convolution of a gaussian (G) and a window function (W) (*cf.* solid line in the left frame of figure 4.8.) :

$$G * W = \frac{1}{\sigma\sqrt{2\pi}} \int_{-R}^{+R} \exp\left(-\frac{(x-t)^2}{2\sigma^2}\right) \mathrm{d}t \tag{4.3}$$

$$= \frac{1}{2}\left[erf\left(\frac{x+R-\mu}{\sigma\sqrt{2}}\right) - erf\left(\frac{x-R-\mu}{\sigma\sqrt{2}}\right)\right] \tag{4.4}$$

  This function is characterized by three parameters: mean (μ), width (σ) and a rectangular width (R) due to the window function. A fourth parameter is the number of counts in the fitted peak of the excitation-energy spectrum. The gaussian width σ takes into account the resolution of the detection system. The target was relatively thick as mentioned earlier, and the window function was introduced to take into account the dispersion in proton energy due to the target thickness. The width of the energy window is obtained from a GEANT4 simulation of the detection system made by our collaborators at IPN-Orsay [Giro 11]. The gaussian parameters in the $G * W$ function are released (free parameters) during the fit of the ground state and the first excited state leading to 7 free parameters (3 parameters $\times$ 2 states $+$ one parameter corresponding to the Carbon background).

- Unbound states are fitted by an $G * W$ function, determined as above, convoluted with a Breit-Wigner (BW) distribution describing a resonance. Compared to the $G * W$ distribution the resulting distribution $G * W * BW$ (*cf.* solid line in the right frame of figure 4.8) has one additional parameter describing the width of the resonance.

- In contrast with the states at low energy, unbound states are sensitive to the deuteron break-up. In order to reduce the number of parameters their gaussian width is set equal to that of the ground state. Centroids, amplitude and the FWHM of the Breit-Wigner (Γ_{BW}) are set free during the fit. However, the fit with the last parameter is not conclusive due to the low statistics and the overlaping of the different states. The first fit gave $\Gamma_{BW} = 0$ most of the time. Thereafter this parameter has been manually set to zero leading to 6 free parameters (two parameter $\times$ 3 states).

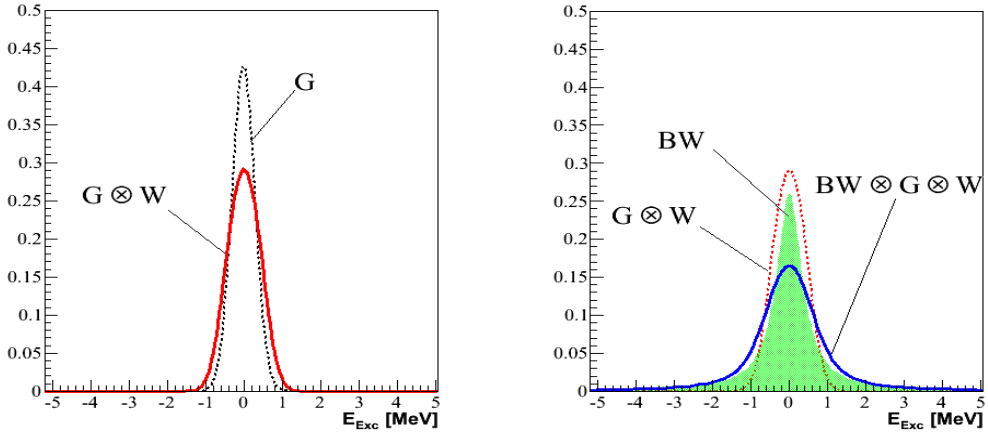

Figure 4.8: *Different distributions commonly used to fit bound states (left panel) and unbound states (right panel). "G", "W" and "BW" represents a Gaussian, a window and a Breit-Wigner distributions, respectively.*

- The angular range lying in the most backward angles in the CM $[105° - 113°]$ was used to normalize the Deuteron break-up (*cf.* figure 4.9). The number of events in the other angular ranges were calculated after supposing an isotropic emission in the CM.

In total 13 parameters for the $156° - 170°$ angular range have been used for the fit. The excitation energy spectrum is fitted and the extracted peak centroids and FWHM are summarised in table 4.1. The peak centroid corresponding to the G.S. (*cf.* next section) has an offset of 201 keV. This offset (E_0) was subtracted to the energies provided by the fit.

Energy [MeV]	FWHM [MeV]	Energy - E_0 [MeV]
0.203(27) (E_0)	1.032(42)	**0.000(27)**
2.681(49)	1.474(100)	**2.478(49)**
4.398(91)	1.257(34)	**4.195(91)**
5.630(190)	1.346(32)	**5.427(190)**
6.594(46)	1.401(31)	**6.391(46)**

Table 4.1: *The first two columns present the energy levels and their corresponding FWHM found by fitting the excitation energy spectrum corresponding to the reference angular range. The third column gives the energies corrected by E_0 (see text).*

The fit of the excitation energy spectra for each angular range are shown in figure 4.9. They are fitted with the same protocole after fixing the centroids of the second excited state and the unbound states. Due to the low transfer cross-section and limited statistics no contribution from the states at 5.88 and 6.39 MeV could be extracted in the $[106°-112°]$ angular range, which corresponds to the largest CM angles. Also, in the $[138° - 143°]$

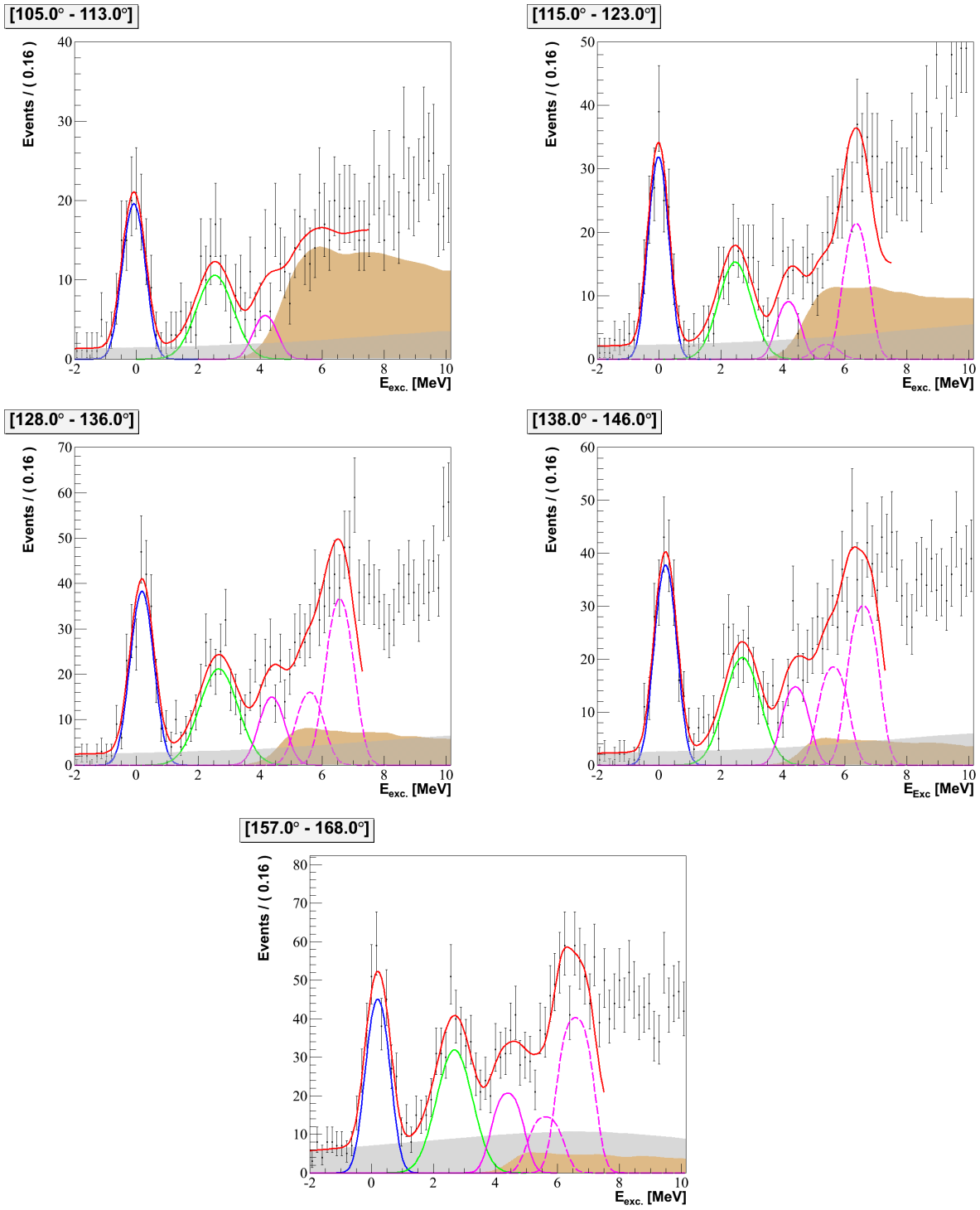

Figure 4.9: *Analysis of excitation energy spectra for the ^{69}Ni for five laboratory angular ranges. For details about the fitting procedure see text.*

angular range the fit did not provide a contribution for the state at 5.43 MeV and the resulting curve is in moderate agreement with the data.

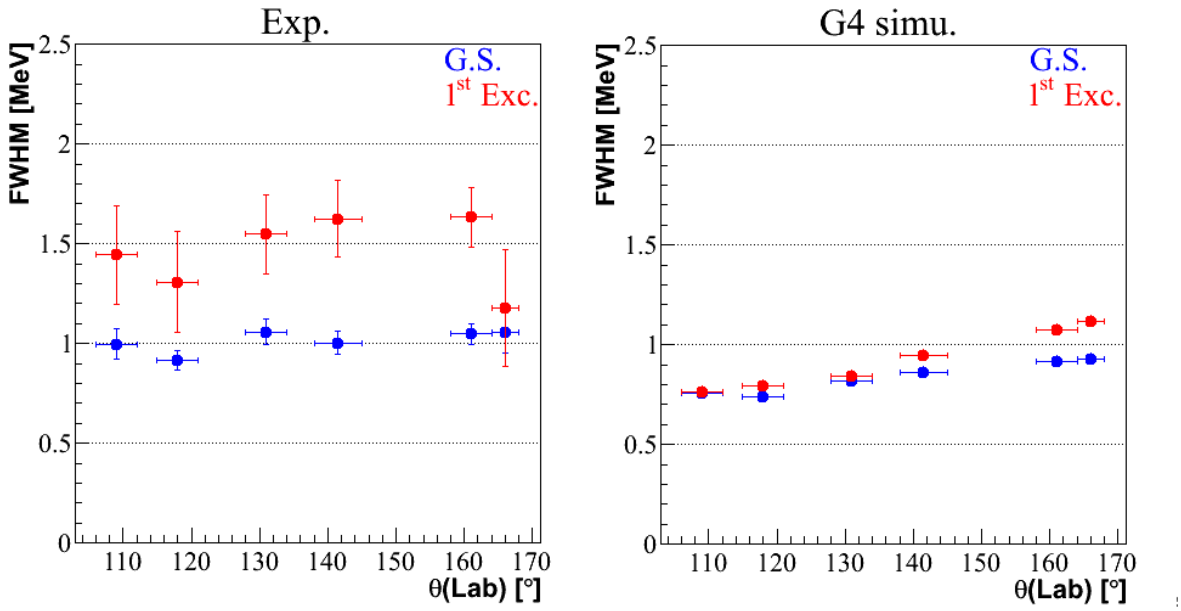

Figure 4.10: *FWHM of the ground state (green) and of the first excited state (red) with respect to the different angular ranges (left panel). Except for the angular range around* 166° *the width of the first excited state is found to be* ≈ 1.5 *times the width coresponding to the ground state. This effect is not reproduced by the simulated FWHM shown on the right panel.*

The FWHM of the ground state is roughly equal to 1 MeV. However, the FWHM of the first excited state is found to be ≈ 1.5 times larger as shown in figure 4.10 (left panel). This result is obtained for all the angular ranges except the one corresponding to $[164° - 168°]$ which has the lowest statistics. However, as can be seen in figure 4.10 (right panel) simulations clearly show that the expected FWHM of an excited state at 2.5 MeV is close to that corresponding to the ground state. It suggests that the first excited state is composed of a doublet of states close in energy and amplitude.

4.4 DWBA analysis

The use of a reaction model is mandatory to extract the nuclear structure information from the differential cross-sections. For the present analysis, we have used the standard one-step DWBA model described in Appendix C. In the DWBA approximation, the distorted waves are generated from optical potentials reproducing the elastic scattering cross-section for the entrance and exit channels.

4.4.1 Model for the optical potentials

The optical models provide the wave functions associated to a colliding pair of nuclei. The optical potential can be obtained in a phenomenological approach, where a suitable analytical form for the potential is adopted. Its depth and geometry parameters are determined by means of parameter adjustement to best fit available experimental data. Woods-Saxon potential form is widely used in DWBA calculations to model the optical potential and the literature contains many successful parametrizations.

The complete potential can be written as,

$$U(r) = V_C(r_C) - V_V f(r, r_V, a_V) - i\left(W_V f(r, r_V, a_V) - 4W_S \frac{d}{dr} f(r, r_S, a_S)\right) - V_{SO}\,\overrightarrow{\sigma}\cdot\overrightarrow{l}\left(\frac{\hbar}{M_\pi c}\right)^2 \frac{1}{r}\frac{d}{dr} f(r, r_{SO}, a_{SO}) \quad (4.5)$$

with $f(r, r_i, a_i)$ describing a Woods-Saxon potential,

$$f(r, r_i, a_i) = \frac{1}{1 + \exp\left(\dfrac{r - r_i A^{\frac{1}{3}}}{a_i}\right)} \quad (4.6)$$

Twelve parameters are needed to *model* the interaction describing the elastic scattering. $V_C(r_C)$ is the Coulomb potential of a uniformly charged sphere of radius $R_C = r_C A^{1/3}$. V_V is the volume potential depth, r_V is its radius and a_V its diffuseness. Two other imaginary potentials are also added: W_V, r_V and a_V are the depth, radius and the diffuseness of the absorption volume potential, respectively. The same goes for W_S, a_S and r_S representing the parameters of the absorption surface potential. Finally, a term of spin-orbit coupling is added to the potential, whose parameters are V_{SO}, A_{SO} and r_{SO}. The spin-orbit potential is multiplied by the square of the pion Compton wavelength $\left(\frac{\hbar}{M_\pi c}\right)^2 = 2.00\ \mathrm{f^2m}$, a conventional normalization factor, where M_π is the mass of the pion.

The potentials parameters are supposed to vary slowly and smoothly through the nuclear chart. Potential depths, radius and diffuseness for nuclei studied for the first time can thus be calculated according to these available parametrizations from the literature taking into account the mass number, the charge and the bombarding energies of the interacting nuclei. It is noteworthy to mention that the values of the radius r_C and diffuseness a_C of the Coulomb potential vary very little in the transfer case (typical values are $r_C = 1.25$ fm and $a_C = 0.65$ fm).

In order to constrain the optical potentials parameters, the measurement of elastic scattering differential cross-sections may be useful. In principle, the optical model parameters used to describe the transfer must reproduce the differential cross-section of the elastic channel providing a good test to validate the used optical-potential parameters.

In this experiment we only measured the transfer reaction, thus we are not able to validate the optical model parameters by the differential cross-section trend of the elastic

channel. However, DWBA calculations are performed with several optical potentials, from different parametrization in the literature, in order to evaluate their influence on the results. It is noteworthy to mention that the currently available parametrizations are adjusted on a set of elastic scattering data for a large number of nuclei close to stability. We will briefly present the optical potentials used in this work for the entrance channel $^{68}Ni + d$ and for the exit channel $^{69}Ni + p$.

For each channel, two different parametrizations were used and their combination provided 4 sets of potentials used to achieve the DWBA calculations and compare them with experimental data.

4.4.1.1 Entrance channel potentials

Potential E1: Daehnick *et al.* [Daeh 80] obtained a parametrization of the elastic scattering of deuterons at energies ranging from 12 to 90 MeV on nuclei of masses comprized between $A = 27$ and $A = 238$ covering our experimental conditions[1]. Their search for global settings for optical potentials is based on a set of 4000 data points (reaction cross sections, differential cross-sections and vector polarization).

The deduced potential, built to reproduce the elastic scattering of deuteron, does not consider the effects of deuteron break-up. This can be of importance in our study hence we use a second parametrization of the optical potential for the entrance channel that takes into account the deuteron break-up.

Potential E2: It was demonstrated that standard DWBA is unable to provide a satisfactory description of the data for many (d,p) and (p,d) reactions for incident energies around 20 MeV and higher [John 70]. A prescription was proposed in order to account for deuteron break-up in the entrance channel. The adiabatic prescription [John 70, Harv 71] is designed to describe approximately the elastic wave plus the components in which the deuteron has been broken up with the neutron and the proton continuing to move together[2] with little relative momentum. These components would also contribute to the transfer reaction [Satc 83] and in some cases its important contribution must be taken into account. The prescription consists in replacing the deuteron optical potential V_{pn} by $\widetilde{V}_{pn}$,

$$\widetilde{V}_{pn} = \frac{\langle \phi_d | V_{pn}[V_n + V_p] | \phi_d \rangle}{\langle \phi_d | V_{pn} | \phi_d \rangle} \tag{4.7}$$

where,

- ϕ_d is the wave function for the deuteron ground state.
- V_n (V_p) is the neutron-target (proton-target) optical potential at one-half the deuteron energy.

[1] The reaction studied in this work is equivalent in direct kinematics to a deuteron bombarding energy around 24 MeV/u impinged on a target of ^{69}Ni.

[2] The proton and neutron are still bound together within a ^3S state

We use the nucleon-nucleus optical-model potential parametrization given by Varner *et al.* [Varn 91] and presented in the following paragraphs. Apart from modifying the potential parameters (depth, diffuseness and radius), the ingredients of an adiabatic calculation are the same as for standard DWBA calculation. However, the potentials can no longer reproduce the elastic cross sections.

4.4.1.2 Exit channel potential

For the description of the interaction of the outgoing proton with ^{69}Ni we have used one parametrization (S) described in the following paragraph.

Potential S: This parametrization used in the exit channel was made by Koning and Delaroche [Koni 03]. It is based on extensive experimental data sets including average resonance parameters, total and non-elastic cross sections, elastic-scattering angular distributions and analyzing powers. The parameters where adjusted to fit data covering a large nucleus mass range ($24 \leqslant A \leqslant 209$) and a large proton laboratory-energy range (1 keV to 200 MeV).

4.4.2 Extraction of angular momenta and spectroscopic factors

The DWBA differential cross-sections are calculated using the DWUCK4 code [Kunz 74] and the aforementioned parametrizations. The shape of the calculated distributions provides the transferred angular momentum by comparing it to the experimental cross-section. The experimental spectroscopic factor is obtained by a χ^2 adjustement of the calculated distribution on the data. The χ^2 is defined as,

$$\chi^2 = \frac{\sum_{i=1}^{N} \left[\frac{\Sigma_i^{exp} - (C^2S) \times \Sigma_i^{DWBA}}{\Delta(\Sigma_i^{exp})} \right]^2}{N-1} \tag{4.8}$$

where,

- $\Sigma_{i,}^{exp} = \frac{d\sigma_i^{exp}}{d\Omega_{CM}}$ is the measured cross section in the CM reference frame,
- $\Delta(\Sigma_i^{exp}) = \delta\left(\frac{d\sigma_i^{exp}}{d\Omega_{CM}}\right)$ is the corresponding uncertainty,
- $\Sigma_i^{DWBA} = \frac{d\sigma_i^{DWBA}}{d\Omega_{CM}}$ is the calculated cross section on the basis of DWBA,
- C^2S is the spectroscopic factor[3],
- and N is the total number of experimental points.

[3] In the rest of this chapter we will refer to the spectroscopic factor by "SF".

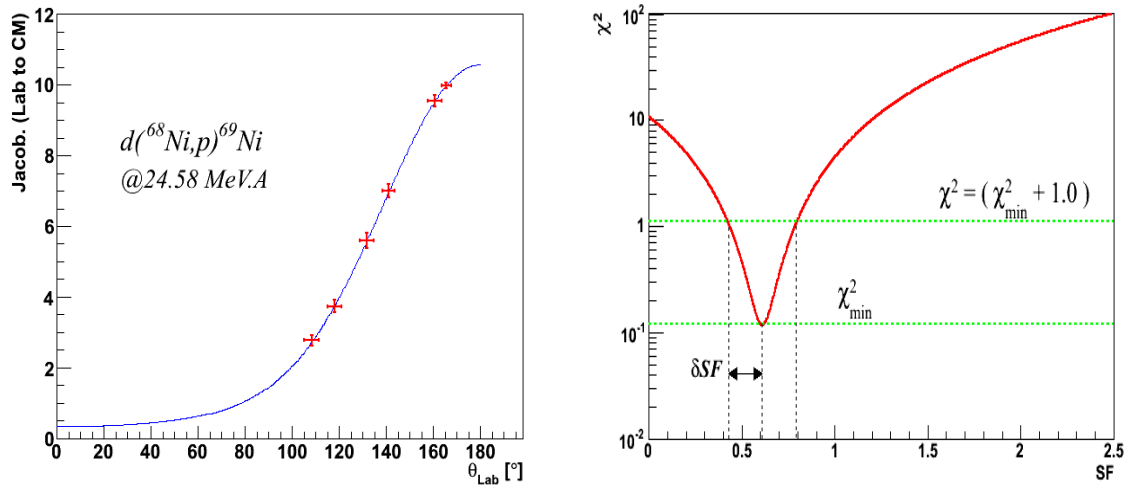

(a) (b)

Figure 4.11: *The left panel shows the Jacobian curve used to transform the experimental cross-sections measured in the laboratory to the CM reference system. The red crosses represent the considered angular ranges (horizontal bars) and the error on the Jacobien (vertical bars). The right panel shows a typical variation of the χ^2 with respect to the spectroscopic factor obtained by normalization of the calculated DWBA distributions to the experimental data.*

For the calculation of the experimental errors we combine equations 3.31 and 3.34 used to determine the differential cross-section in the laboratory reference frame and the transformation to the center of mass frame, respectively. We have,

$$\frac{d\sigma}{d\Omega_{CM}}(\theta_{CM}) = J(\theta_{Lab})\frac{N_{det}(\theta_{Lab})}{N_{Beam}N_{Target}\Delta\Omega(\theta_{Lab})} \tag{4.9}$$

The uncertainty $\delta\sigma^{exp}_{CM}$ was calculated by error propagation from the estimated uncertainties on the different parameters explained in the following list.

- For the number of detected protons N_{det}, we consider the statistical error given by $\frac{\sqrt{N_{det}}}{N_{det}}$,
- for the number of incident particles N_{Beam}, the statistical error is given by $\frac{\sqrt{N_{Beam}}}{N_{Beam}}$, which is negligible here.
- Besides the error on the CD_2 target thickness, Polyethylene targets are hygroscopic and thus deuteron-hydrogen ratio is subject to changes. No measurement of this ratio has been performed, thus an error of 10% was estimated on the (2.6 mg/cm^2) target.
- the error on the proton emission angle is threefold:

1. the position resolution of the beam trackers leads to an uncertainty of 0.1° calculated in chapter 3,
2. the proton straggling in the CD_2 target leads to an uncertainty of 0.3° estimated by the simulation using SRIM energy loss tables,
3. the detection system (geometry, strip width) leads to an uncertainty of $\leqslant 0.38°$ in S1 and reduces with increasing laboratory angles,

finally, the overall error on angle is given by $\sqrt{(0.1°)^2 + (0.3°)^2 + (0.38°)^2} \approx 0.5°$

Besides the listed errors, the related errors on solid angle, geometrical efficiencies and Jacobian were also taken into account.

The curve 4.11b shows a typical variation of χ^2 value with respect to SF. The extracted SF corresponds to the minimum χ^2_{min} value. The upper and lower boundaries of SF ($SF \pm \delta SF$) are defined as the values corresponding to $\chi^2 = \chi^2_{min} + 1$ as shown in the figure 4.11b. δSF will be called the experimental error corresponding to the error due to the normalization procedure on the experimental error bars.

4.4.2.1 Ground state

For the first observed state (0 MeV) we consider the following transferred angular momenta $l = 0$, $l = 1$, $l = 2$ and $l = 4$ corresponding to $3s_{1/2}$, $2p_{1/2}$, $2d_{5/2}$ and $1g_{9/2}$ states in ^{69}Ni, respectively. The horizontal and vertical error bars correspond to the angular range in CM angles and the total experimental error described earlier, respectively. Figure 4.12 shows the comparison of experimental and calculated differential cross-sections for two combinations of optical potentials. The angular momentum transferred to this state is determined unambiguously as $l = 4$ which corresponds to the population of the $1g_{9/2}$ orbital in ^{69}Ni.

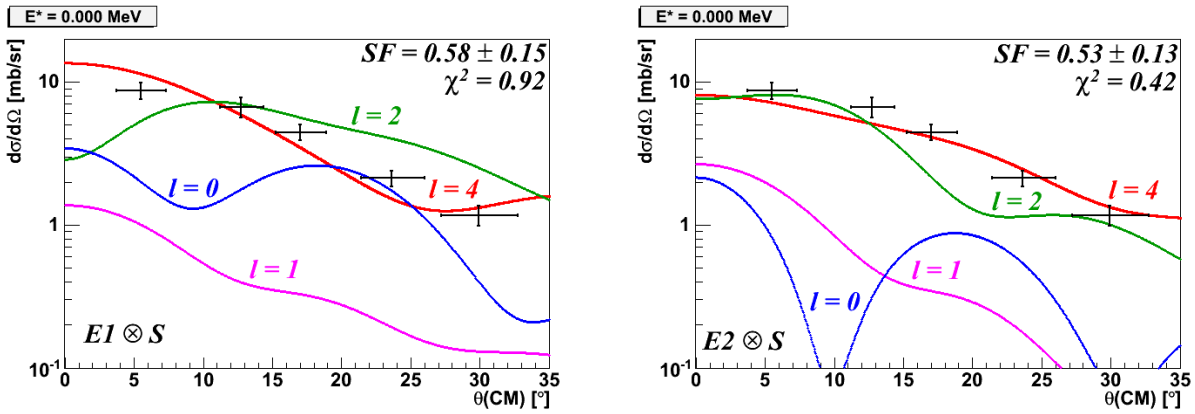

Figure 4.12: *Proton angular distribution for the ground state and comparison with DWBA calculations for two combinations of optical potentials referred as $E1(2) \otimes S$ (see text). The same spectroscopic factor obtained for $l = 4$ is applied for $l = 0$, $l = 1$ and $l = 2$ distributions.*

We note that the trend of the $l = 0,\ 1,\ 2$ distribution changes with the choice of the entrance potential. Depending on the optical potential combination the spectroscopic factor value undergoes a variation of 10% (see table 4.2 in section 4.4.3). Visually and according to the χ^2 values, the experimental distribution is better reproduced when using the adiabatic potential (E2) for the entrance channel. This confirms the importance of taking into account the deuteron break-up in the entrance channel. The adiabatic potential will be retained for the rest of the analysis.

4.4.2.2 First measured excited state

The first excited state at 2.48 MeV, favourably populated in our experiment, has never been observed before in previous studies. In order to determine its angular momentum we consider the same transferred angular momenta ($l = 0,\ 1,\ 2,\ 4$) as for the ground state using the adiabatic potential for the entrance channel. By comparing the calculated cross sections to the experimental points a transferred angular momentum of $l = 4$ is clearly excluded in favor of an $l = 2$ transfer (see figure 4.13). An $l = 0$, or 1 transfer is un-

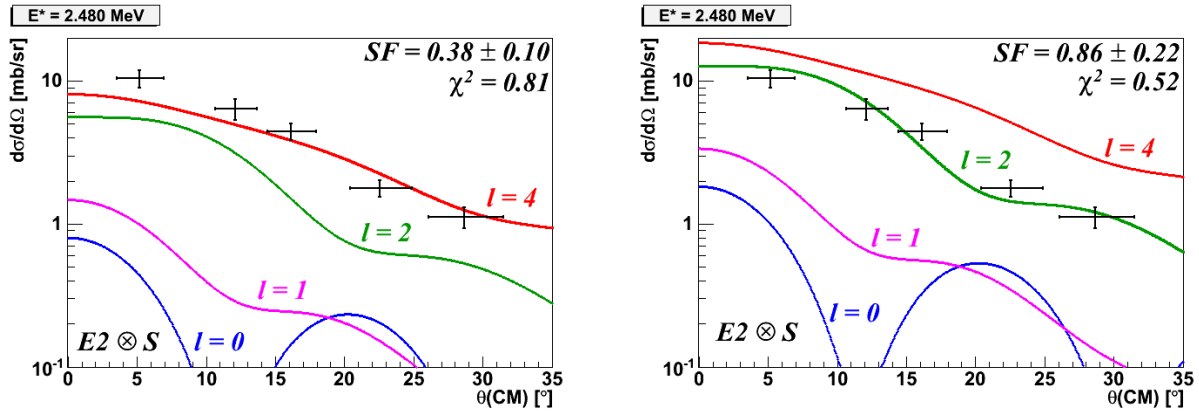

Figure 4.13: *Proton angular distribution for the first excited state (*2.48 MeV*) and comparison with ADWA calculations for an $l = 4$ (left panel) and $l = 2$ (right panel) transfers.*

favoured due to the large momentum mismatch at the present beam energy ~ 24 MeV/u. According to shell-model calculations (discussed later) the identified state corresponds to the $2d_{5/2}$ orbital in ^{69}Ni we are searching for. As mentioned previously, we have strong indication that the observed peak corresponds to a doublet of states.

The first excited state is adjusted by two states close in energy at 2.05 MeV and 2.74 MeV, respectively (see figure 4.14, top left panel). The width of each component is fixed according to the GEANT4 simulation (window width) and the width of the ground state (gaussian width) in the same prescription as given in section 4.3. According to the χ^2 value, the proton angular distribution of the first component at 2.05 MeV is compatible with an $l = 2$ transfer (figure 4.14, bottom left panel). In the case of the second component at 2.74 MeV, shown in the bottom right panel of figure 4.14, the proton angular distribution is compatible with an $l = 4$ transfer ($\chi^2 = 0.39$) without reproducing the

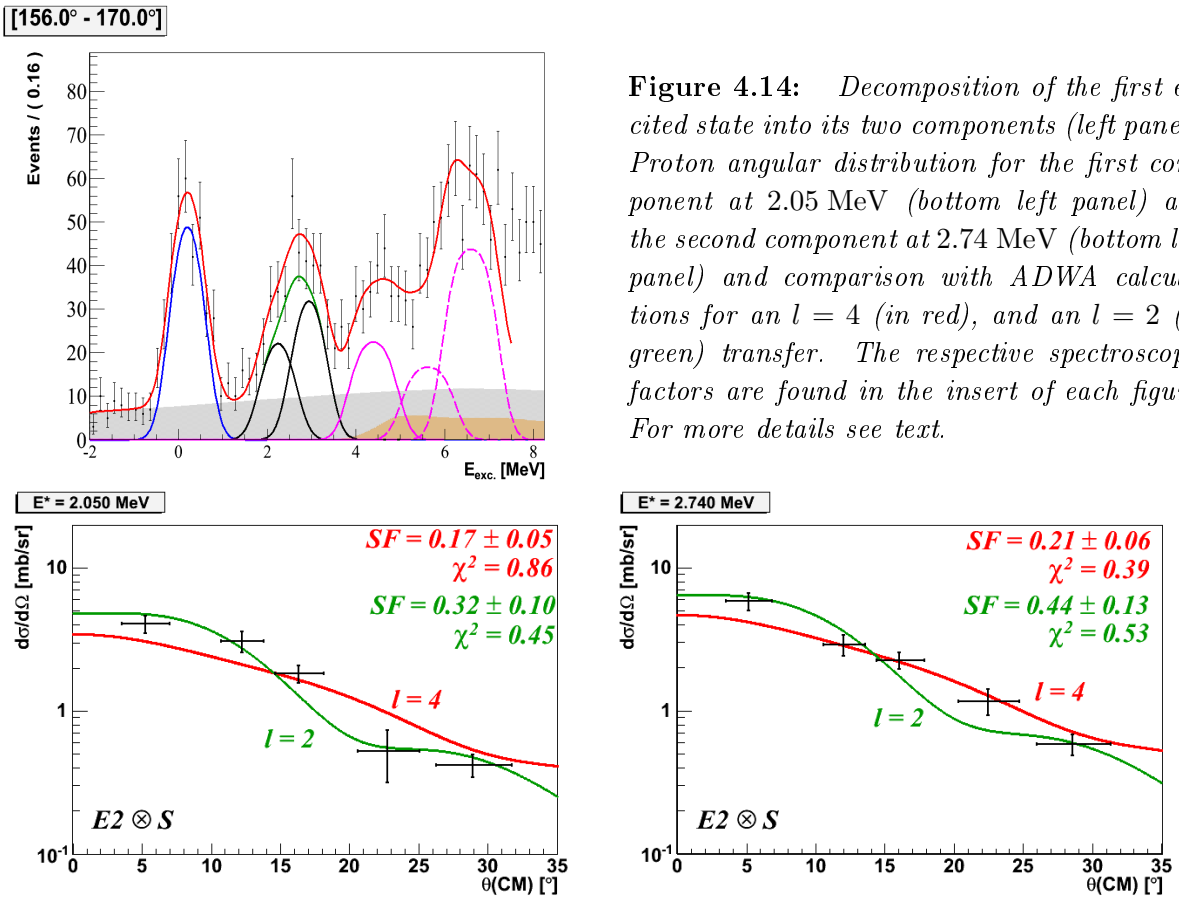

Figure 4.14: *Decomposition of the first excited state into its two components (left panel). Proton angular distribution for the first component at* 2.05 MeV *(bottom left panel) and the second component at* 2.74 MeV *(bottom left panel) and comparison with ADWA calculations for an $l = 4$ (in red), and an $l = 2$ (in green) transfer. The respective spectroscopic factors are found in the insert of each figure. For more details see text.*

point lying in the most forward angles (CM). On the other hand, the experimental points are also compatible with an $l = 2$ transfer with a close χ^2 value ($\chi^2 = 0.39$) and fits the most forward experimental point (in CM). The latter observation leads us to consider the second component as an $l = 2$ transfer.

4.4.2.3 Second measured excited state

Figure 4.15 shows the calculated DWBA differential cross-sections for a neutron transfer to the orbitals $2p_{1/2}$, $1g_{9/2}$, $2d_{5/2}$, $1g_{7/2}$, $3s_{1/2}$, $2d_{3/2}$ and $1h_{11/2}$. In this calculation we use the adiabatic potential combination ($E2 \otimes S$). The deuteron energy corresponds to the beam energy in direct kinematics and the excitation energy is fixed at 4.190 MeV. The calculated angular distributions corresponding to an $l = 0$ and $l = 1$ are smaller by at least one order of magnitude than the other distributions due to momentum mismatch as mentioned above. The data points for CM angles in $[10°; 20°]$ and $[30°; 40°]$ angular ranges are crucial to distinguish amongst the different distributions.

For the second excited state at 4.190 MeV we have considered $l = 2$ and 4 transferred angular momenta corresponding to the $2d_{3/2}$ or $2d_{5/2}$ and $1g_{7/2}$, respectively.

In figure 4.16 we show the ADWA analysis of the second excited state. The experimental distribution is best reproduced for a transferred angular momentum of $l = 2$ and

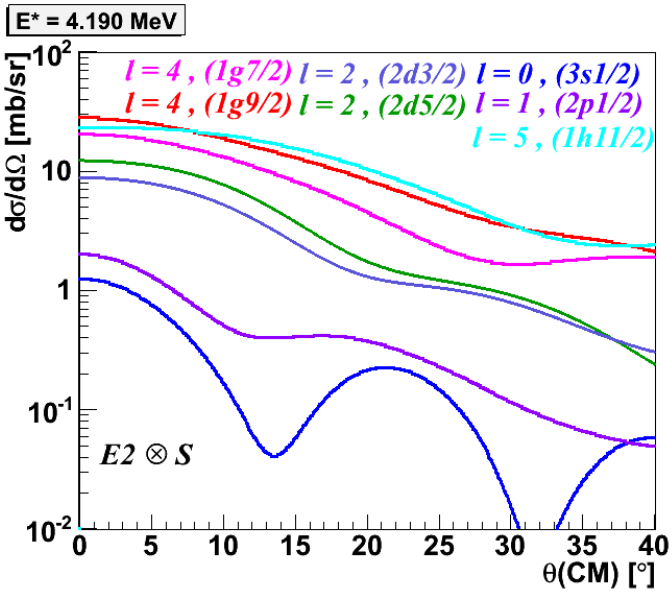

Figure 4.15: *Calculated DWBA differential cross-sections for the energy level at* 4.190 MeV *for several transferred angular momenta using the* $E2 \otimes S2$ *potential combination. The spectroscopic factor is normalized to unity.*

$l = 4$. According to the χ^2 value, an $l = 2$ (4) transfers corresponding to the population of the $2d_{5/2}$ ($1g_{7/2}$) orbitals seem to fit the experimental cross-sections with $\chi^2 = 0.42$ ($\chi^2 = 0.44$). The fit with an $l = 2$ transfer corresponding to the population of the $2d_{3/2}$ orbital had greater χ^2 ($\chi^2 = 0.98$) and is not considered here.

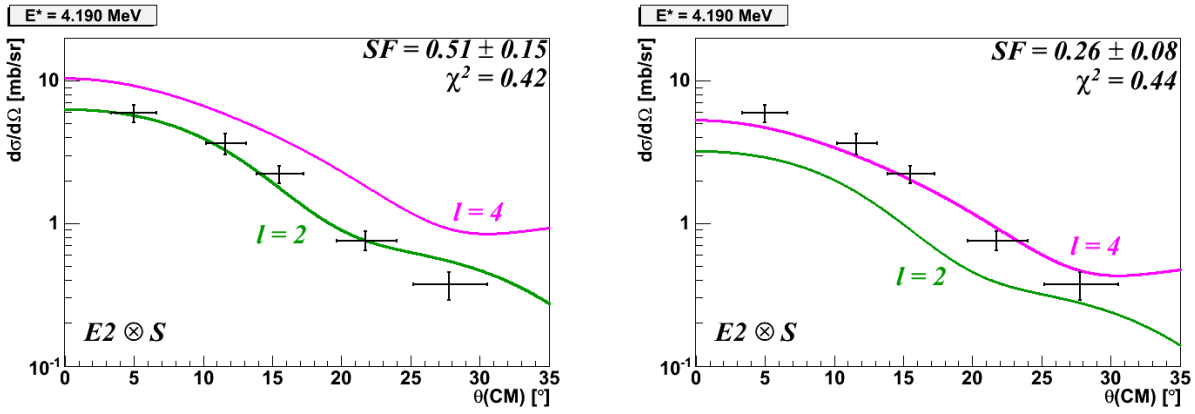

Figure 4.16: *Proton angular distribution for the second excited state (*4.19 MeV*) and comparison with ADWA calculations. The left panel show the fit with* $l = 2$ *(*$2d_{5/2}$*) distribution (in green). The right panel shows the fit with* $l = 4$ *(*$1g_{7/2}$*) distribution (in red). Curves not fitted to the data are normalized with the spectroscopic factors in the insert.*

4.4.2.4 Unbound excited states

The two unbound states considered in the following discussion are placed at 5.43 MeV and 6.39 MeV excitation energy. For these states, the data points of their experimental distributions corresponding to $\sim 30°$ in CM ($[105° - 113°]$ in laboratory) is subject of considerable uncertainty. As shown in the fit of the excitation energy spectra in figure 4.9,

the energy levels above 4.190 MeV are substantially affected by the deuteron break-up. In this angular range the transfer is disadvantaged in favor of the deuteron break-up and no peak structure is observed (*cf.* figure 4.9). As a result the corresponding data point is missing and not considered during the ADWA analysis. The same applies for the data point $\sim 21°$ in CM ($[115° - 123°]$ in laboratory) for the first resonnance (at 5.43 MeV) where the peak area is clearly underestimated by one order of magnitude due to the dominance of the deuteron break-up in this angular ranges and the low statistics in general.

Although the number of experimental data points is reduced to three (four) out of five for the first (second) resonnance, an attempt to extract the angular momentum and the spectroscopic factor for these energy levels is made. Moreover, the extraction of the angular momentum suffers of ambiguities due to the relatively weak sensitivity of the shape of the calculated angular distribution with the transferred l (see figure 4.15). This sensitivity even decreases with increasing excitation energy.

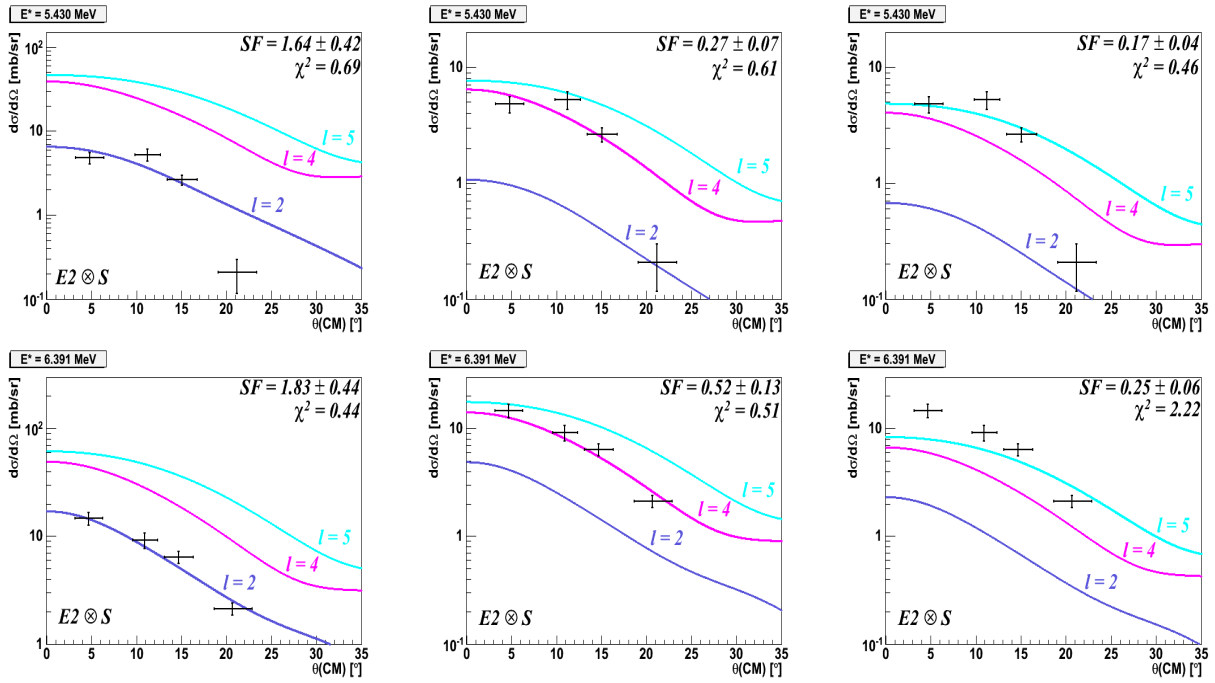

Figure 4.17: *Proton angular distribution for the first resonance at* 5.43 MeV *(first raw) and at the second resonnance* 6.39 MeV *(second raw) compared to ADWA calculations. The data point below* 1 mb/sr *in the first raw is not considered in the fit. Curves not fitted to the data are normalized with the spectroscopic factors in the insert.*

For the first resonance at 5.43 MeV we consider the following transferred angular momenta $l = 2,\ 4$ and 5. The experimental distribution seems to be consistent with an $l = 5$ corresponding to $1h_{11/2}$ being favored according to the χ^2 value. For the second resonance at 6.39 MeV we consider the same angular momenta for the ADWA analysis. In this case the experimental distribution seems to be consistent with an $l = 2$ or $l = 4$ distribution as shown in figure 4.17 with $l = 2$ being favored according to the χ^2 value.

4.4.3 Spectroscopic factors

The angular-momentum assignments and the spectroscopic factors are summarized in table 4.2. The last column shows the values of the spectroscopic factors for the combination $E2 \otimes S$ adopted in this analysis followed by the experimental error due to the normalization procedure (experimental error).

Energy [MeV]	l	J^π	SF $(E2 \otimes S)$	χ^2
0.00	4	$9/2^+$	0.53 ± 0.13	0.42
2.48	2	$5/2^+$	0.86 ± 0.22	0.52
$\rightarrow$ 2.05	2	$5/2^+$	0.32 ± 0.10	0.45
$\rightarrow$ 2.74	(2)	$5/2^+$	0.44 ± 0.13	0.53
4.19	(2)	$5/2^+$	0.51 ± 0.15	0.42
4.19	(4)	$7/2^+$	0.26 ± 0.08	0.44
5.43	(4)	$7/2^+$	0.27 ± 0.07	0.61
5.43	(5)	$11/2^-$	0.17 ± 0.04	0.46
6.39	(4)	$7/2^+$	0.52 ± 0.13	0.51

Table 4.2: *Extracted spectroscopic factors for the populated states in ^{69}Ni. The last column corresponds to the value of the spectroscopic factor followed by the normalization error on the experimental points (experimental error).*

The ground state is assigned an angular momentum of $l = 4$ corresponding to the occupation of the $1g_{9/2}$ orbital with a spectroscopic factor 0.53 ± 0.13. The first excited state at 2.48 MeV was unambiguously identified as an $l = 2$ angular-momentum transfer corresponding to the $2d_{5/2}$ orbital we are searching for, with a spectroscopic factor $SF = 0.86 \pm 0.22$. We recall that data give evidence that the state in question is a doublet of $l = 2$ states close in energy with a sum of spectroscopic factors of similar amplitude $\sum SF = 0.76 \pm 0.23$.

For the second excited state at 4.19 MeV and the last two unbound states at 5.43 MeV and 6.39 MeV the corresponding experimental data points were affected by the deuteron break-up background. Concerning the bound state at 4.19 MeV both $l = 2$ and $l = 4$ assignments are possible. The assignment of $l = 2$ corresponding to the population of $2d_{5/2}$ orbital would violate the sum rule ($\sum SF = 1.27 \pm 0.38(exp)$). However, the experimental error associated to the normalization of the experimental cross section is of the order of $\sim 30\%$. Thus, the assignment of $l = 2$ $(2d_{5/2})$ is reasonable if we take into account the associated errors. Due to the very close χ^2 values in the case of $l = 2$ $(2d_{5/2})$ and $l = 4$ $(1g_{7/2})$ both assignments are equally probable, the SF in the latter case is $0.26 \pm 0.08(exp)$.

The ADWA analysis was done only on three points for the first resonnace and four points for the second resonnace, thus the assignment of angular momenta to these states are questionable. However, according to the χ^2 value for the first resonance, the experimental cross-sections are better reproduced with a $l = 2$ distribution. In this case the associated spectroscopic factor is very large ($SF = 1.64$) and not respecting the sum rule even if we take into account the associated errors ($0.42(exp)$). An assignment of $l = 4$ is acceptable where $SF = 0.27 \pm 0.07(exp)$. We privilege a contribution (at least partial) of $l \geqslant 4$ orbitals since the SF, assuming $l = 2$, are large while strong strength fragmentation is expected at such high excitation energies. For the state at $E_{exc} = 6.39$ MeV, an $l = 2$

transfer is ruled out for the same reason as in the case of the first resonance while an $l = 5$ transfer is clearly not compatible with experimental points with a relatively high value of $\chi^2 = 2.22$. Finally, an $l = 4$ assignment provides a reasonable fit of the data with a $SF = 0.53 \pm 0.13$.

4.5 Shell-model calculations

4.5.1 Valence space

The theoretical calculations were performed by the NuTheo group in Strasbourg using the shell-model formalism on a core of ^{48}Ca and a large valence space which includes the pf-shell for protons and $1f_{5/2}$, $2p_{1/2}$, $2p_{3/2}$, $1g_{9/2}$, $2d_{5/2}$ orbitals for neutrons (see figure 4.18).

The effective interaction used here starts with the same sets of two-body matrix elements as the LNPS interaction [Lenz 10], in which further monopole corrections were introduced in order to constrain the proton-gap evolution from ^{68}Ni to ^{78}Ni deduced in [Siej 10].

From the shell-model point of view these calculations are very demanding due to the large valence space considered. Therefore, the number of particles that can be excited in the valence space are limited or "truncated". For these calculations the truncation is $t = 8$, which means that a maximum of 8 nucleons, with respect to Z=28 and N=40 closures, are allowed to be excited to the rest of the valence space. This truncation is sufficient to assess the single-particle degrees of freedom we are interested in.

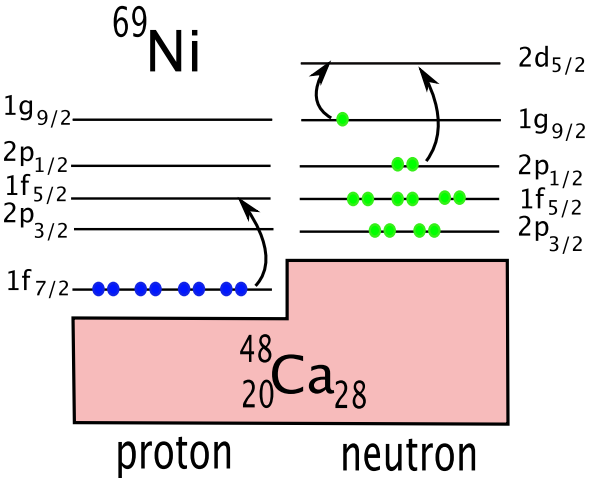

Figure 4.18: *Decomposition of ^{69}Ni into a core of ^{48}Ca and a valence space comprizing pf-shell and $1f_{5/2}$, $2p_{1/2}$, $2p_{3/2}$, $1g_{9/2}$, $2d_{5/2}$ orbitals for neutrons. Only 8 nucleons with respect to ^{68}Ni core can be excited (see text).*

4.5.2 Comparison with large-scale shell-model calculations

The distribution of the nuclear strength for an orbital informs us about the fragmentation of this orbital at different energies and its associated strength. The distribution

function of the strength calculated from the shell model described above can be seen in the right panel of figure 4.19, for three different energy gaps between the $1g_{9/2}$ and the $2d_{5/2}$ effective single-particle energies. It shows the major contribution of the energy levels associated with the $1g_{9/2}$ and $2d_{5/2}$ neutron orbitals. The dominant energy level corresponding to the population of the $1g_{9/2}$ orbital lies at 0 MeV (in red). Concerning the $2d_{5/2}$ orbital, the calculation shows two 5/2+ states of sizeable spectroscopic factors at low energies (*cf.* table 4.3, spectroscopic factors in bold text). The distribution function of the orbitals observed experimentally at higher excitation energies are not calculated since their respective orbitals are not included in the valence space given above and thus the discussion will be restricted only to the ground state and the first excited state observed in this experiment.

The calculated shell-model states with their energies and spectroscopic factors are listed in table 4.3. The energy states with spectroscopic factors less than 0.01 are not included. A more exhaustive list of the predicted levels and their associated spectroscopic factors is given in Appendix D.

Shell Model calculations	Gap $N = 50$ $(1g_{9/2} - 2d_{5/2})$					
	1.5 [MeV]		2.5 [MeV]		3.5 [MeV]	
	Energy	SF	Energy	SF	Energy	SF
$1g_{9/2}$	0.00	**0.89**	0.00	**0.86**	0.00	**0.93**
	5.23	0.01	5.55	0.02	5.58	0.03
	5.69	0.01			7.41	0.01
$2d_{5/2}$	1.49	**0.79**	2.12	**0.46**	2.09	**0.05**
	1.92	**0.09**	2.50	**0.43**	2.92	**0.80**
	5.80	0.03	6.19	0.05	3.63	0.03
	7.06	0.02	7.22	0.02	6.10	0.07
					7.57	0.03

Table 4.3: *Calculated shell-model energies and their associated spectroscopic factors for the neutron $1g_{9/2}$ and $2d_{5/2}$ orbitals in ^{69}Ni for three gaps. The details of calculations are given in section 4.5.1.*

The presence of a well pronounced ground state corresponding to the neutron $1g_{9/2}$ orbital is well reproduced by the shell-model calculations. The spectroscopic factor associated to this state is rather large ($SF_{SM} \sim 0.90$) and lies well above the value found experimentally ($SF = 0.53 \pm 0.13$) at 1σ. In principle such difference could be explained from a Shell-Model point of view by the absence of higher orbitals in the calculations as mentioned above. From an experimental point of view, one must not underestimate the experimental errors, especially, the one related to the contamination of the CD_2 target by Hydrogen atoms as mentionned before. Finally systematic errors related to the choice of the parametrized potentials used in the DWBA and ADWA could lead to an error of 30% of the estimated spectroscopic factors and must also be taken into account. The calculations predict also other fragments of this orbital at higher energies with very small spectroscopic factor $\leqslant 0.03$.

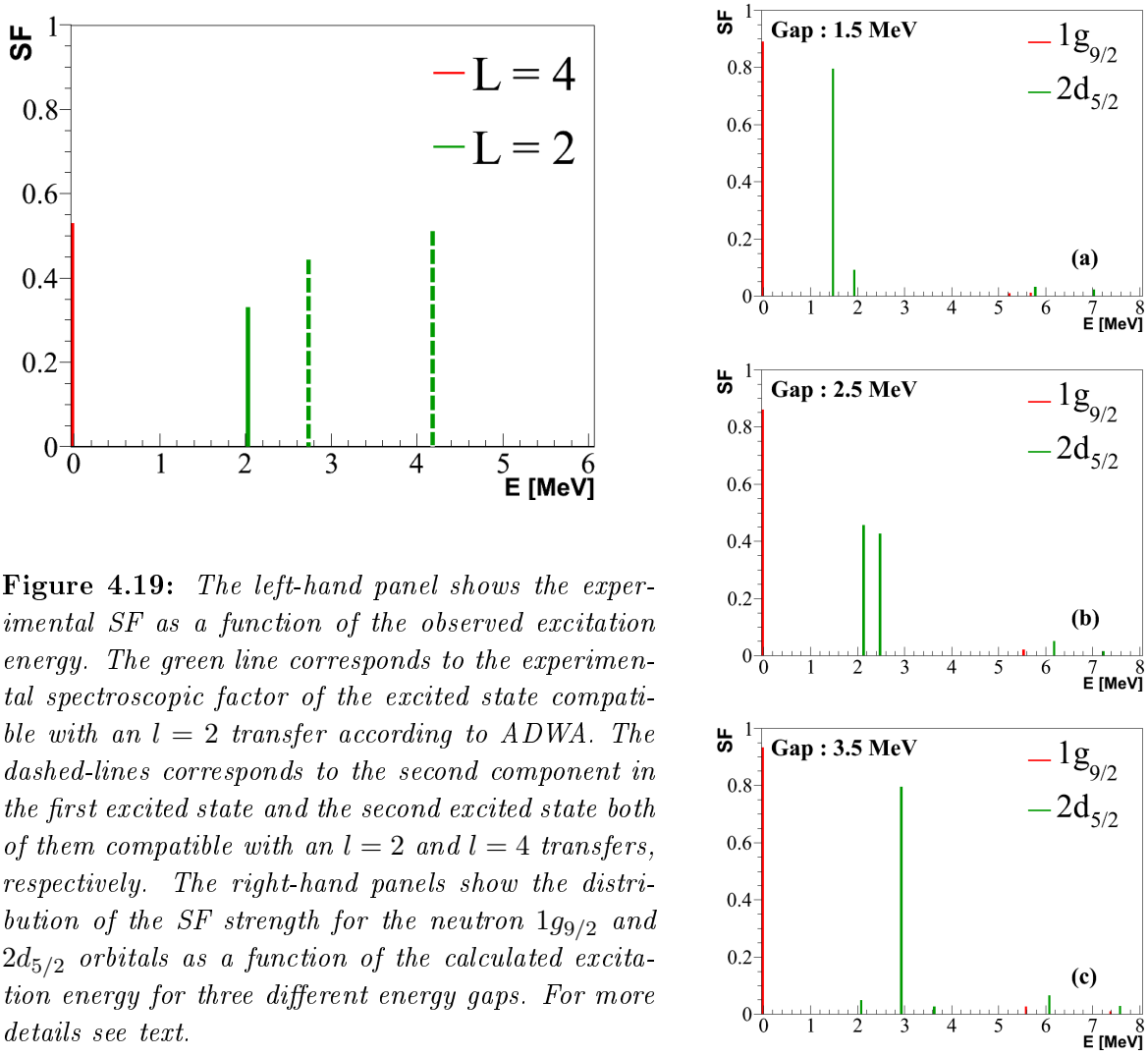

Figure 4.19: *The left-hand panel shows the experimental SF as a function of the observed excitation energy. The green line corresponds to the experimental spectroscopic factor of the excited state compatible with an $l = 2$ transfer according to ADWA. The dashed-lines corresponds to the second component in the first excited state and the second excited state both of them compatible with an $l = 2$ and $l = 4$ transfers, respectively. The right-hand panels show the distribution of the SF strength for the neutron $1g_{9/2}$ and $2d_{5/2}$ orbitals as a function of the calculated excitation energy for three different energy gaps. For more details see text.*

For the $2d_{5/2}$ orbital, the calculations predict the presence of two low-lying states close in energy which confirms our hypothesis that the first excited state observed experimentally is very likely a doublet of 5/2+ states. The mean of the predicted states, weighted by their respective spectroscopic factor (1.53 MeV) has been lowered relatively to the neutron $1g_{9/2}$ orbital in order to favor the onset of deformation observed experimentally in the neutron-rich Fe and Cr isotopes around $N = 40$ [Ljun 10] due to the proximity of quadrupole partner $1g_{9/2}$ and $2d_{5/2}$ orbitals. As a consequence, the $2d_{5/2}$ neutron orbital should also be low in ^{69}Ni. Indeed, this work shows that it is considerably low even if, at 2.48 MeV excitation energy, it lies $\sim$ 1 MeV higher than the predicted energy. This is explained by the fact that in the shell-model calculations the single-particle energy of the $2d_{5/2}$ orbital has to be excessively lowered in order to compensate for the absence of the other neutron orbitals of the *gds*-shell missing in the valence space, in particular the $3s_{1/2}$ and $1g_{7/2}$ orbitals, which bring additionnal $\Delta l = 2$ correlations (in the case of $2d_{5/2} - 3s_{1/2}$). The total strength of the two 5/2+ states (for a gap of 2.5 MeV) given by the sum of their spectroscopic factor (0.89) is in very good agreement with the experimental spectroscopic factor (0.86 ± 0.25).

It can be noticed in table 4.3 that the predicted $2d_{5/2}$ state at 1.49 MeV contains $\approx 90\%$ of the total strength assigned to the doublet. The large width of the first excited state experimentally observed (see section 4.3) could not be explained with such an asymetric composition of the strength as predicted by the calculations. It is more likely due to a doublet of states having similar spectroscopic factors.

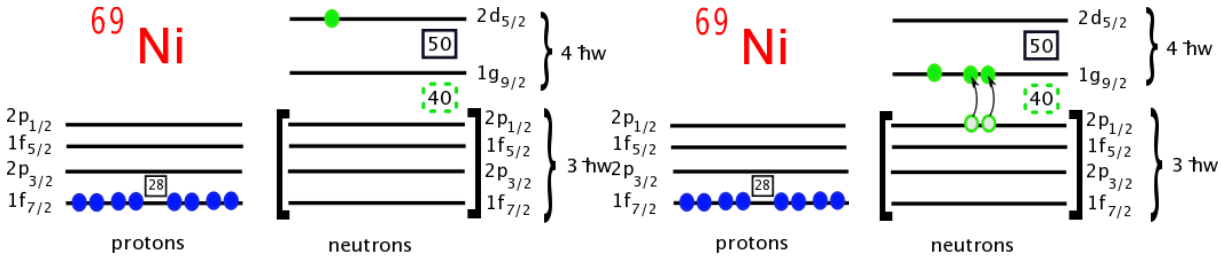

Figure 4.20: *Two competing configuration of the ^{69}Ni according to large scale Shell-Model calculations. Both configurations are coupled to a total spin of $J^\pi = 5/2^+$. The position of the $2d_{5/2}$ neutron orbital with respect to the $1g_{9/2}$ neutron orbital favors one or the other configuration and influences the SF balance of the 5/2+ doublet predicted earlier with Shell-Model calculations.*

It is noteworthy to mention that a shift towards higher energies of the $2d_{5/2}$ single-particle energy influences the strength function, favouring a rather equal strength distribution between the two states in the doublet, in a way consistent with the experimental data. In the central panel on the right of figure 4.19 we show the same calculations after shifting the single-particle energy of the $2d_{5/2}$ towards higher energies by 1 MeV. In this case the calculated strengths reproduce better our hypothesis for the first excited state. Moreover the weighted centroid of the $2d_{5/2}$ doublet (2.3 MeV) is in better agreement with the experimental results. Moreover, by shifting the SPE of the $2d_{5/2}$ by 2 MeV(gap 3.5 MeV) the strength distribution of the spectroscopic factor is again asymmetric giving more strength to the second component at higher energy.

The changing of the spectroscopic factor balance between the 5/2+ states in a regular way could be explained in a simplistic manner by considering the two main competing configurations observed in the shell-model calculations represented in figure 4.20. The configuration on the left panel, denoted ϕ_1, corresponds to the occupation of the $2d_{5/2}$ orbital by the valence neutron. The second configuration in figure 4.20 corresponds to the excitation of a neutron pair into the $1g_{9/2}$ orbital leading to the occupation of the latter orbital by three neutrons coupled to a $J^\pi = 5/2^+$. It will be denoted ϕ_2. The mixing of all possible configurations ϕ_i including ϕ_1 and ϕ_2 produces all the observed 5/2+ states in the calculation and in particular the 5/2+ doublet with the highest spectroscopic factor observed in the right-hand panels of figure 4.19. In a simple approach the physical states with the highest spectroscopic factors (Ψ_{low} and Ψ_{high}) could be written as the linear combination of ϕ_1 and ϕ_2 as follows :

$$|\Psi_{low}\rangle = \alpha|\phi_1\rangle + \beta|\phi_2\rangle \tag{4.10a}$$

$$|\Psi_{high}\rangle = -\beta|\phi_1\rangle + \alpha|\phi_2\rangle \tag{4.10b}$$

In the case where the $2d_{5/2}$ orbital is close to the $1g_{9/2}$ orbital, ϕ_1 configuration is favoured ($\alpha > \beta$ in the system of equations 4.10) and the first component (Ψ_{low}) of the 5/2+ doublet

will be favoured in strength as shown in the panel (a) on the right of figure 4.19. In the other case where the $N = 50$ gap is large, the configuration ϕ_2 with three neutrons on the $1g_{9/2}$ orbital will be favoured ($\alpha < \beta$ in the system of equations 4.10) which explains the strength in panel (c) on the right of figure 4.19 caracterized by a high spectroscopic factor for the second component (Ψ_{high}) of the 5/2+ doublet.

The second excited state at 4.19 MeV is represented in the left panel of figure 4.19 by a green-dashed line. As discussed earlier (see section 4.4.2.2), this state is compatible with $l = 2$ and $l = 4$ transfer distributions. If it is identified to $2d_{5/2}$, the summed spectroscopic factor would be $SF = 1.27 \pm 0.38$, preserving the sum rule within error bars. However, the experimental cross section for this state is also well reproduced by the $1g_{7/2}$ DWBA distributions with a similar χ^2 value. This interpretation is more in agreement with the present shell-model calculations which do not predict a significant fragment of $2d_{5/2}$ strength above the doublet.

Figure 4.21 shows the level scheme of ^{69}Ni so far. We only add the states observed in this work determined unambiguously in experiment and reproduced in Shell-Model calculations. It is worth to mention that the energies of the new states are determined with a relatively low resolution due to low statistics in this experiment.

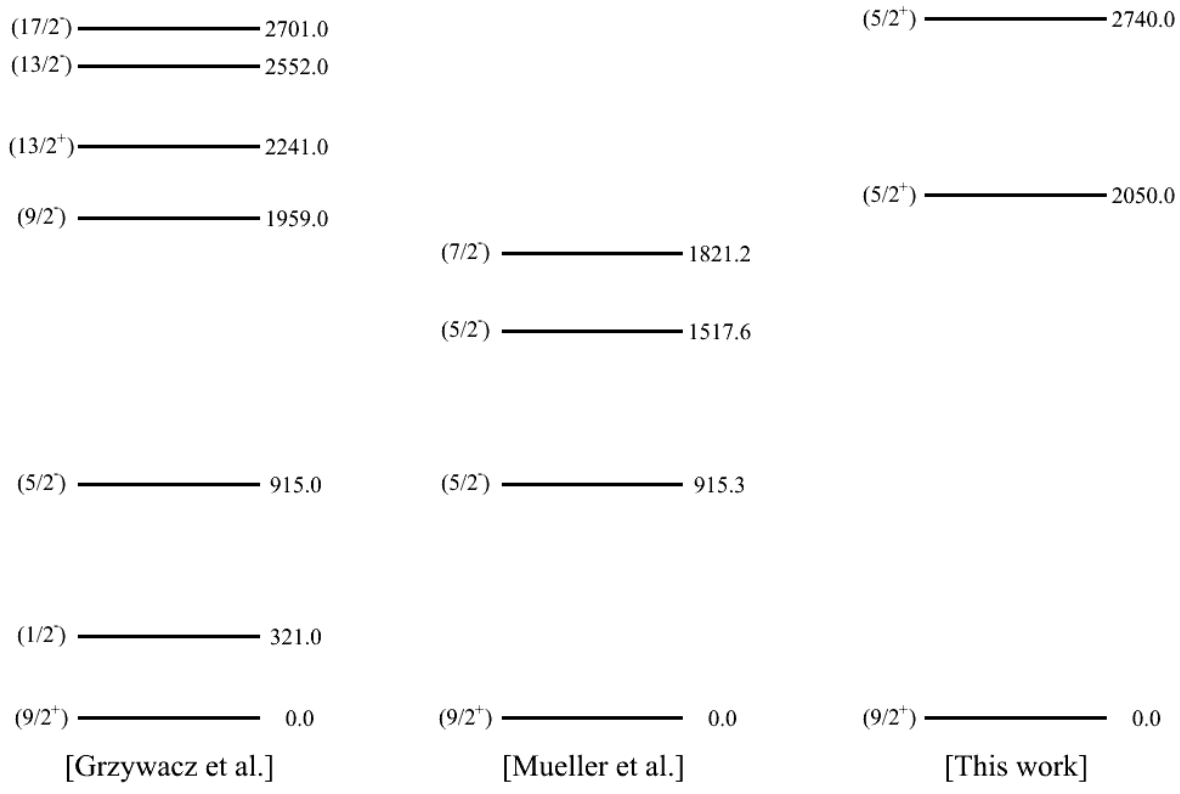

Figure 4.21: *Level scheme of ^{69}Ni observed in previous works of [Grzy 98, Muel 99] and in this work.*

The position of the $d_{5/2}$ neutron orbital established at low energy of 2.5 MeV confirms that this orbit plays a crucial role in the onset of deformation of nuclei around $N = 40$ and

that the mechanisms leading to the appearance of a sudden collectivity at $N = 20$ and $N = 40$ are indeed the same. Thus the present work can provide a precious benchmark for the position of the $2d_{5/2}$ orbital, up to now determined indirectly in the shell-model calculations. It establishes the correct valence space to be used in this region and rules out the validity of nuclear shell models in too restricted valence spaces.

It is also regarded as an important ingredient in the pathway towards the ^{78}Ni structure. Sieja's work has shown that the neutron $1g_{9/2} - 2d_{5/2}$ energy difference increases from ^{68}Ni to ^{78}Ni from 1.5 MeV to about 5 MeV [Siej 10]. Our measurement confirms the rather small energy difference between the neutron $1g_{9/2}$ and $2d_{5/2}$ orbitals (2.48 MeV) in ^{68}Ni. As a consequence, the $N = 50$ gap in ^{78}Ni will be even larger than 5 MeV following Sieja's predictions. On the proton side, due to the tensor force, the $Z = 28$ proton gap is weakened. The filling of the neutron $1g_{9/2}$ orbital pushes down the proton $1f_{5/2}$ below the proton $1p_{3/2}$ orbital [Fran 01] and pulls up the closed proton $1f_{7/2}$ orbital. The effect on the $1f_{5/2}$ orbital leads to the crossing of the proton $1f_{5/2}$ and $1p_{3/2}$ orbitals in ^{75}Cu [Flan 09]. The closing of the neutron $1g_{9/2}$ orbital however is not sufficient to reduce enough the $Z = 28$ gap which remains important in ^{78}Ni. In conclusion these results indicate that both $Z = 28$ and $N = 50$ are sizable and supports a doubly magic ^{78}Ni nucleus.

Chapter 5

Conclusion and perspectives

An experiment was performed in 2009 at GANIL in order to search for the neutron $2d_{5/2}$ orbital in ^{69}Ni. A ^{68}Ni beam was produced at 25.14 MeV/u by fragmentation of a primary beam of ^{70}Zn at an energy of 62.5 MeV/u on a production target made out of Be. Nuclei were selected using the In-Flight separation technique in the magnetic spectrometer LISE leading to a relatively highly pure ($\approx 85.8\%$) secondary ^{68}Ni beam. The latter impinged on a CD_2 target and the transfer reaction $d(^{68}Ni, p)$ was studied. Single-neutron transfer reactions are an efficient tool to determine the excitation energy, the angular momentum and the spectroscopic factor of low-lying single-particle states.

This study is of great interest in this mass region $N = 40$. An onset of deformation has been observed in neutron-rich Cr and Fe isotopes around $N = 40$. It has been explained in a shell-model approach [Caur 05, Ljun 10, Lenz 10] by two particle-two hole neutron excitations from the $2p_{1/2}$ orbital to the $1g_{9/2}$ with a low-lying $2d_{5/2}$. Besides understanding the shell evolution in this region the position in energy of the $2d_{5/2}$ in ^{69}Ni nuclei could be extrapolated to ^{78}Ni in order to predict the magicity of this nucleus lying at the intersection of well established magic numbers $N = 50$ and $Z = 28$.

The experimental setup was designed to the study of direct reactions in inverse kinematics. CATS, MUST2, S1 detectors and a plastic scintillator allowed the detection of light-charged particles and heavy residues in coincidence. The energy resolution of MUST2 (S1) and CATS-MUST2(S1) time-of-flight is good enough to identify the light recoils by $\Delta E - E$ and $E - ToF$ techniques. The excitation-energy spectrum of the heavy residues is calculated using the missing-mass method through the measurements of energy and position of light recoil particles in MUST2 and S1 detectors. The identification of heavy residues in the plastic scintillator is mandatory to select the reaction of interest.

The study of the transfer reaction $d(^{68}Ni, p)$ has improved our knowledge on low-lying states observed for the first time in ^{69}Ni. Five states have been identified and their energies fixed. Two of them lie above the neutron separation energy. The experimental differential cross section for each state is compared to theoretical one calculated with DWBA reaction model using an adiabatic entrance potential. The corresponding angular momentum and spectroscopic factor are extracted for each state by χ^2 minimization.

The first peak of the excitation-energy spectrum has been identified as the ground state of ^{69}Ni. The analysis determined the angular momentum of the neutron transfer as $l = 4$ with a spectroscopic factor of $SF = 0.53 \pm 0.13$. The states corresponding to the remaining strength were not populated in this experiment indicating a high fragmentation of this orbital in ^{69}Ni. According to shell-model calculations the strength of the $1g_{9/2}$ is

concentrated in the ground state and the remaining is highly fragmented at higher energies which is in agreement with the experimental results obtained in this work. However, the calculations predict a greater value of the spectroscopic factor at 0 MeV ($SF_{SM} = 0.86$).

The second peak corresponds to an excited state of ^{69}Ni at 2.48 MeV. An orbital momentum $l = 2$ is clearly attributed by DWBA analysis with a spectroscopic factor of 0.86 ± 0.22. It corresponds to the $2d_{5/2}$ orbital. It is noteworthy to mention that the peak width (FWHM) at this energy is 1.5 times broader than the ground state FWHM. This feature is not reproduced by a GEANT4 simulation, in which experimental resolutions, due to the detector resolutions and target thickness, are taken into account and thus it suggests that the state in question is a doublet. The DWBA analysis associated to the doublet gives 0.32 ± 0.10 and 0.44 ± 0.13 as spectroscopic factors for the first and second component lying at 2.05 MeV and 2.74 MeV, respectively. Shell-model calculations predict the presence of a doublet of states at low excitation energy which is in good agreement with the observed measurement. However, the strength distribution of the $2d_{5/2}$ doublet is highly asymetric and can not explain the observed FWHM of the first excited state. It was noticed that the strength composition between the two components of the predicted doublet is sensitive to the single-particle energy of the $2d_{5/2}$ orbital. A fair agreement between the calculations and the experimental results is obtained by increasing the single-particle energy of the $2d_{5/2}$ orbital by 1 MeV. Starting from a low-lying $2d_{5/2}$ orbital in ^{68}Ni, recent shell-model calculations [Siej 10] have predicted a doubly magic $N = 50$ in ^{78}Ni. Our results confirm

- the assumption of a low-lying $2d_{5/2}$ neutron orbital and its major role in the structure of the nuclei around $N = 40$ and
- that the mechanisms leading to the appearance of a sudden collectivity at $N = 20$ and $N = 40$ are the same.

It also establishes the correct valence space to be used in this region and rules out the validity of nuclear shell models in too restricted valence spaces.

The DWBA analysis of the third peak at 4.19 MeV shows that different l assignments are possible. An $l = 4$ assignment leads to a spectroscopic factor of 0.26 ± 0.08. On the other hand an $l = 2$ assignment leads to spectroscopic factors of 0.51 ± 0.15 if the state is due to the population of the $2d_{5/2}$ orbital. In the last case the sum of spectroscopic factors over the first and the second excited state violates the sum rule ($SF = 1.27 \pm 0.38$). However, an $l = 2$ assignment is still reasonable if we take into account the experimental errors. On the other hand, an $l = 4$ assignment is in better agreement with shell-model calculations since no significant fragment of the $2d_{5/2}$ orbital is predicted at energies above 2.5 MeV.

Above the neutron separation energy, two new peaks are analysed at 5.43 MeV and 6.39 MeV. The extraction of their angular momenta suffered from missing experimental points in their angular distribution and from the uncertainties on the deuteron break-up. The comparison with the calculated DWBA distribution was performed on three and four out of five experimental points, respectively. According to χ^2 minimization the state

at 5.43 MeV is likely to be $l = 5$ or 4 associated to the $1h_{11/2}$ and the $1g_{7/2}$ orbitals with a spectroscopic factor of 0.17 ± 0.04 and 0.27 ± 0.07, respectively. The last state at 6.39 MeV is reasonably reproduced by an $l = 4$ ($SF = 0.52 \pm 0.13$) transfer. The experimental conditions of these states can only lead to tentative assignments of angular momenta and spectroscopic factor values. In addition, assignments leading to a high spectroscopic factor (such as $l = 2$ in the case of the first unbound state) is not favoured since at high excitation energies the orbitals tend to have a strong strength fragmentation. Indication about the nature of these states from large-scale shell-model calculations is not possible as the valence space used in the $N = 4\hbar\omega$ shell is limited to the $2d_{5/2}$ orbital.

A quantitative estimation of the deuteron break-up is of great interest for the energy states lying above the neutron separation energy (S_n). The subtraction of this contribution to the excitation-energy spectrum might help to firmly determine the spectroscopic information of the energy states beyond (S_n) and would reveal new states at higher energies. Moreover, the analysis of particle-γ coincidences is also of great interest. The observation of γ-ray transitions between the new states established in this work and between these states and the ground state could help to build a precise ^{69}Ni level scheme and firmly establish the excitation energies of the new states observed.

Nevertheless, the excitation-energy spectra suffered from poor statistics. The experiment shows the limitation of the detection system in case of the study of higher energy states. The density of these states is rather high compared to the experimental resolution. Improved detection efficiency, energy resolution and increased exotic beam intensities are the key parameters for future progresses. Detectors such as GASPARD (a high-granularity silicon detector for the detection of charged particles) coupled to PARIS and/or AGATA (for γ-ray detection), currently in development, as well as future radioactive beam facilities (SPIRAL2) would certainly help to extend further our knowledge on the structure of exotic nuclei.

Appendix A

Simulation

In this appendix we present the simulation used to estimate the geometrical efficiency and the deuteron break-up. The detection system for the proton is done by two types of detectors MUST2 and S1. These detectors have different geometries, different strip and interstrip shapes and different positions in space. Their space configuration will influence directly two important geometrical quantities:

1. the covered dynamic range constraining the physics accessible to our experiment,
2. the efficiency of the detection system used to calculate the final differential cross sections.

Moreover these quantities may change during the campaign as a function of other parameters such as the target position, the beam profile on the target and most importantly, the position of non-operational strips. Under these circumstances the evaluation of the covered dynamic range and the efficiency of the detection system is not straight forward without a numerical simulation. For this reason a simulation of the experimental setup of Monte-Carlo type is developed under ROOT framework. It is adapted from the basic version of the simulation used in the PhD work of G. Burgunder [Burg 11].

In the present work the simulation is developped to take into account the thickness of the target, the second stage (Si(Li)) of MUST2, the interstrips, the dead layers and the resolution of the detectors. In the following sections we will describe the ingredients of the developped simulation and how we generate and treat simulated events.

A.1 Input

The principal ingredients of the simulation can be divided into three parts:

1. Geometry
   (a) The position of each detector,
   (b) The position of the target,
   (c) Beam profile on the target in X and Y directions.
2. Reaction inputs

(a) The interacting nuclei and their corresponding products,

(b) The excitation energy of each nucleus.

3. Detectors and target characteristics

(a) Target thickness and material (for energy loss calculations),

(b) Dead-layer thickness in detectors,

(c) Interstrip width,

(d) Detector resolution and energy threshold,

(e) Number and type of suppressed detectors or strips.

A.2 Event generation and treatment

The event generation consists of 6 steps:

1. A random generator provides the position of the reaction in the target in X, Y and Z directions.

2. Once the reaction position is defined, phase space calculations are used to produce any number of products. When the number of products is set to 2, the phase space calculations reduce to the simple 2-body kinematics.

3. The present step is used in case of important angular and energy straggling in the target[1]. In this case the SRIM code is used as a subroutine. SRIM takes as input the list of positions and directions of the particle of interest, say protons, generated in steps 1 and 2. The output of SRIM will provide the new positions and directions at the surface of the target.

4. Having the position and direction of the generated proton, a geometrical calculation provides the point of impact in the plane containing the detector. The hit is converted to the corresponding strip numbers. A new energy is calculated taking into account the energy loss in the dead layer and the resolution of the detector.

5. In this step, practical characteristics are associated to the event describing the *quality* of the hit. Such as the state of the strip fired, interstrip hit...

6. Finally all the event characteristics are saved using the same format as the one of the experimental raw data. This simulated data can be used to test the analysis code developed in this work.

[1] In the case where the straggling is irrelevant or negligeable a simpler version of the simulation, not including the present step, is used

A.3 Results

The simulated data are analysed in the same way as the raw data. The simulation give us more insight about the detection system, such as coverage in angle and efficiency. It has also help in the analysis phase, more precisely in the estimation of deuteron break-up.

The figures A.1 and A.3 show the different *"types"* of detected events. In this calculation the following parameters are considered:

1. a target of zero thickness,
2. a realistic beam profile,
3. an isotropic emission for each interaction point in the target,
4. hits on interstrip are rejected,
5. Two hit scenario are considered,
   (a) hit on detectors with out defective strip and no matching between different detectors stages (see figure A.1),
   (b) hit on detectors with defective strips tagged during the real data analysis and stage-matching requested (see figure A.3),.

The corresponding angular coverage is depicted in figures A.1, A.2, and A.3. The geometrical efficiency of the detection system is reduced by ~ 30 to ~ 50 % when defective strips and stage-matching are taken into account.

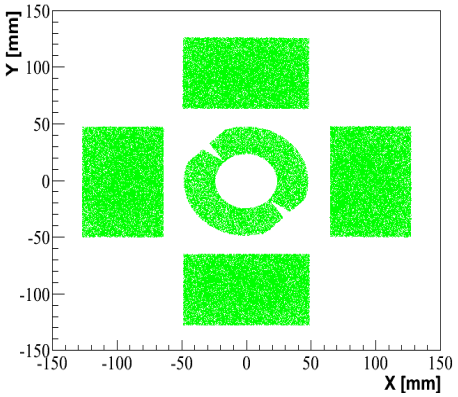

(a) *Hit-pattern on detectors without defective strip and no stage-matching requested*

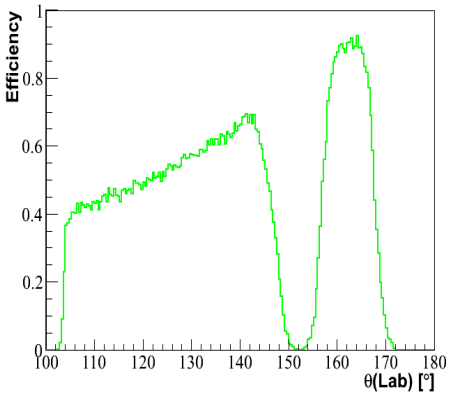

(b) *Associated efficiency*

Figure A.1: *Simulated hit patterns for protons and the corresponding detection efficiency versus angle. The effeciency reduces to zero (cf. figure A.1b) between the angular range covered by S1 and the one covered by the ensemble of MUST2 telescopes (around* 150°*).*

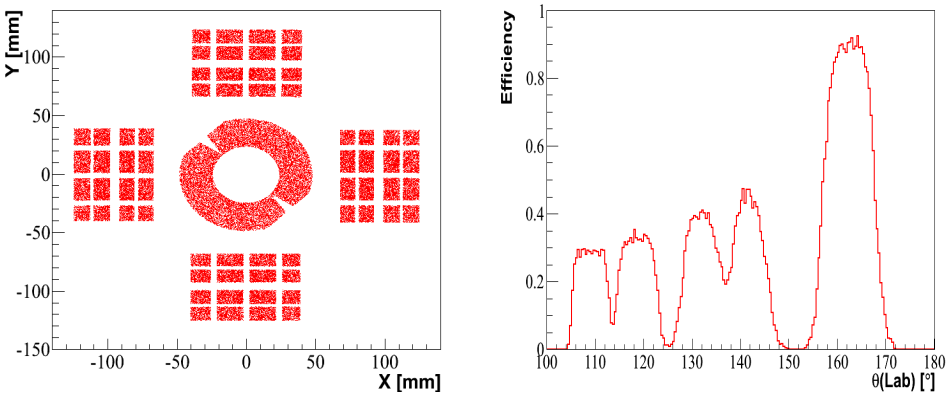

(a) *hit-pattern on detectors with no defective strip and stage-matching requested*

(b) *Associated efficiency*

Figure A.2: *Simulated hit patterns for protons and the corresponding detection efficiency versus angle.*

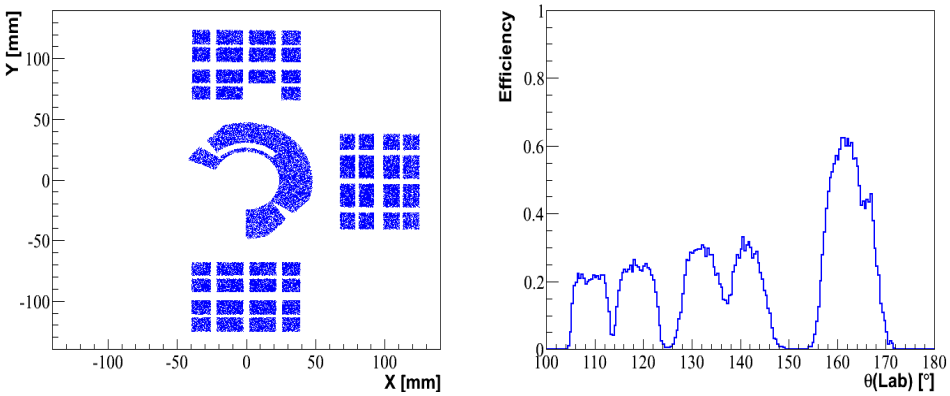

(a) *Hit-pattern on detectors with defective strips tagged during the real data analysis and stage-matching requested*

(b) *Associated efficiency*

Figure A.3: *Simulated hit patterns for protons and the corresponding detection efficiency versus angle.*

Appendix B

Electronic diagrams

In this appendix we present the electronic diagrams associated with the detectors used in our experiment. The abbreviations of each element are explained below:

- U2M (Universal Marker Module): used as a scaler to count the signals reaching each of its inputs,
- NIM/ECL: conversion module from NIM-signal to ECL-signal format,
- Quad coinc and DSCT coinc: coincidence module generating the logical "AND" of its inputs.
- Dual Gate Generator: a module providing a delay and generates a gate,
- FIFO (Fan In Fan Out): this module make several duplicates of the input signal,
- DS and Discri LTD: Threshold Discriminators,
- FCC8 and CFD: Constant Fraction Discriminators,
- DIV (Division Module): the input signal is transmitted once every N times, where N is configured depending on the detector,
- TAC (Time to Amplitude Converter): converts the time between a start and a stop-signal into amplitude,
- ADC (Amplitude to Digital Converter): converts an input analog signal to a digital signal,
- TDC (Time to Digital Converter): converts the time between a start and a stop-signal directly into a digital signal,
- Amp spect. (x) µs: a model used for pulse integration over (x) µs,
- Sampling: sampling module for the ionization chamber,
- RDV (Retard et Durée Variable): generates an ECL-gate whose pulse-width and delay are adjustable,
- Symbol || : Logic "OR",
- Symbol && : Logic "AND",
- Symbol % : Division (See DIV up the list).

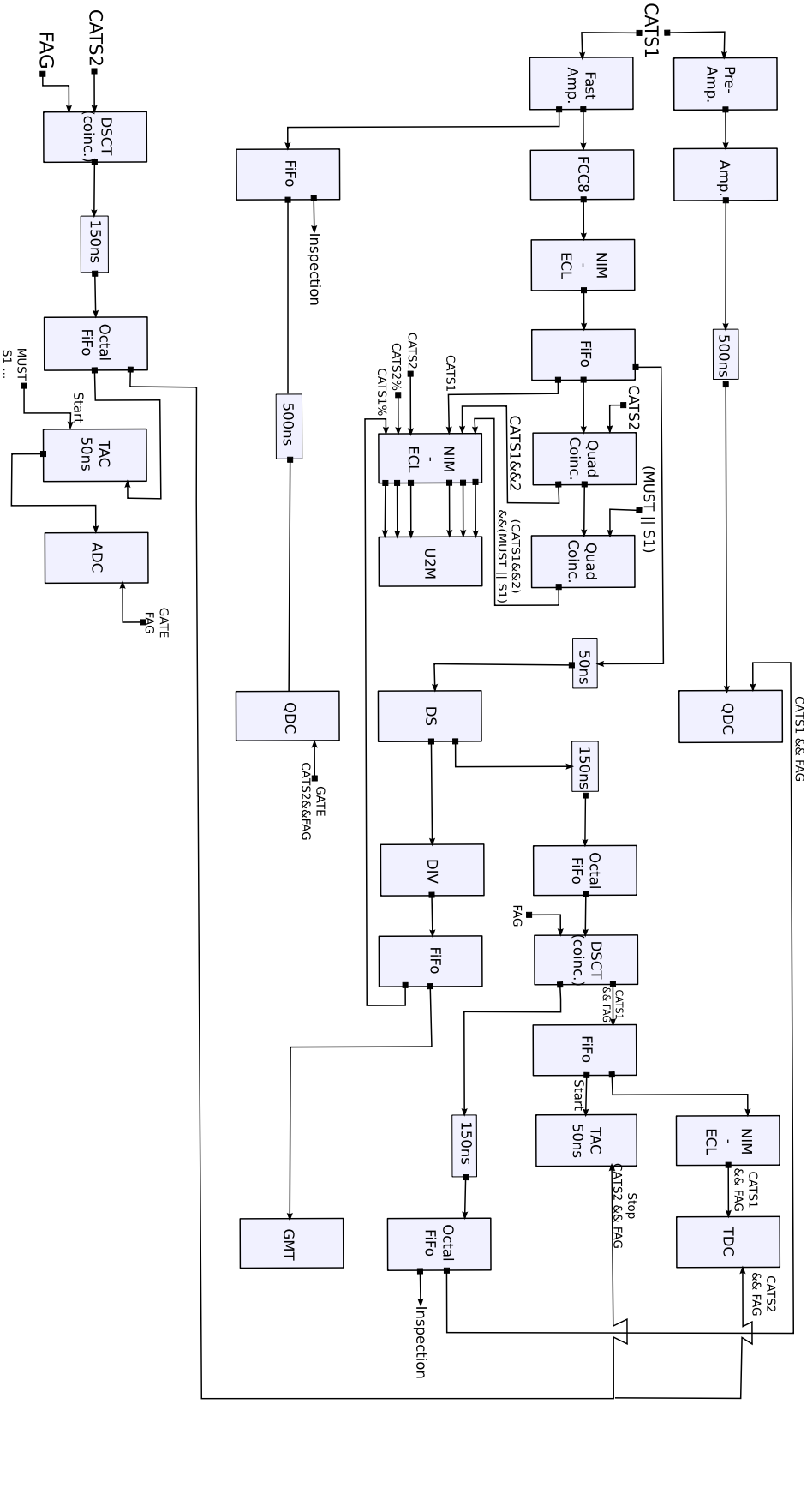

Figure B.1: *Electronic diagram of the time and charge signals of CATS1 and CATS2. The coincidence of the time signal from CATS1(CATS2) with the FAG is used as a start(stop) signal for TACs and TDCs and as gates for QDCs. The time signal of CATS2 is also used as a stop signal for all other detectors to measure time-of-flight. The use of TACs and TDCs is redundant but ensures a time measurement in case of failure. The charge signals from CATS1(CATS2) are authorized to trigger the acquisition once every 1000(3000) detected events.*

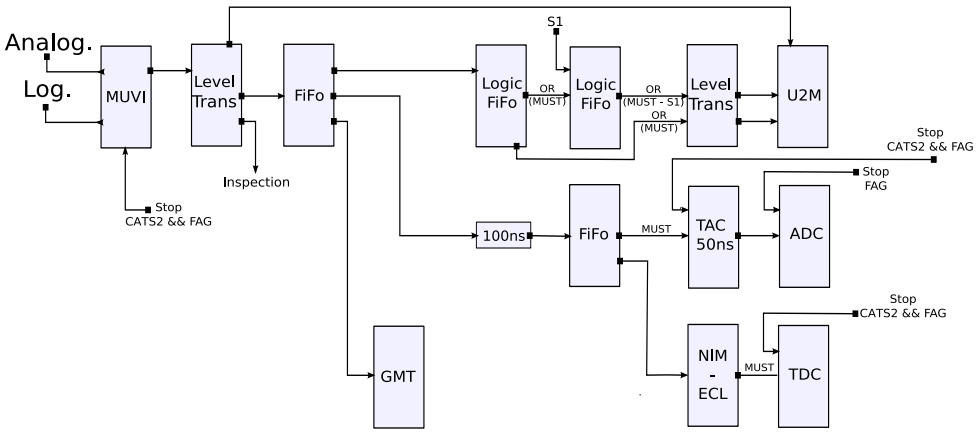

Figure B.2: *Electronic diagram of the MUVI card (light charged particule detectors). The diagrams related to MUST2 and S1 detectors are identical. The analogic signal is sent to the GMT in order to generate the FAG. It also serves as a start for the TDC/TAC in order to encode the time-of-flight between beam tracker and the light charged particle detectors. The signal MUST2 OR S1 is also formed and sent to scalers.*

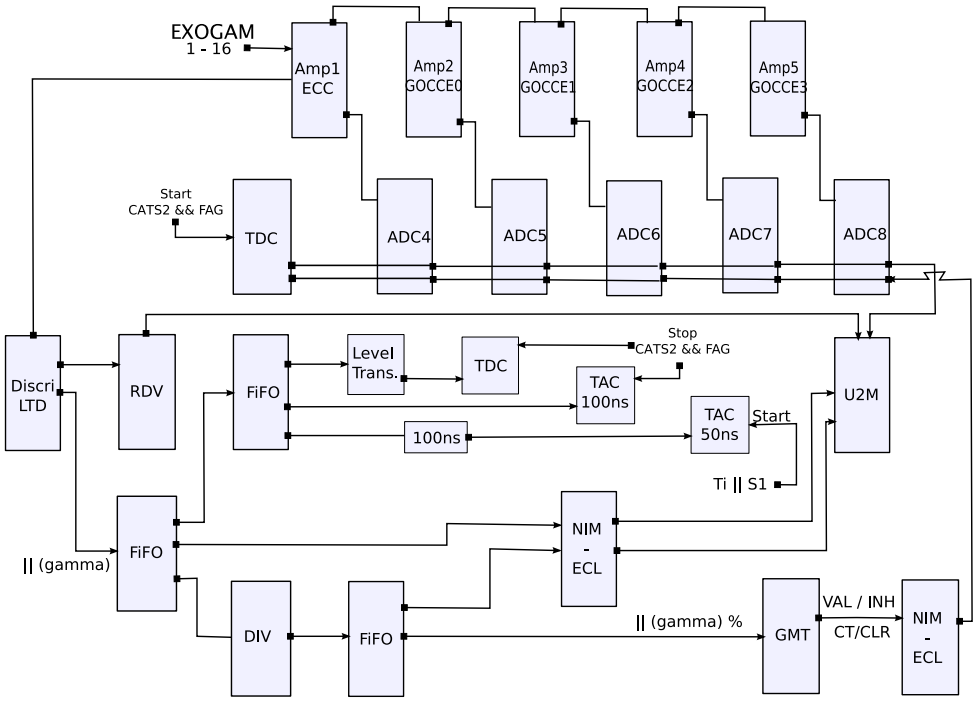

Figure B.3: *Electronic diagram of EXOGAM detectors. The pulse from the detectors serves as a stop signal to encode the time-of-flight with the beam tracker and MUST2-OR-S1, respectively. The signal OR-gamma is used as a start for TDC/TAC stopped by CATS2. The EXOGAM signal is sent to the GMT once every 200 detected events. OR-gamma and OR-gamma% are both sent to scalers.*

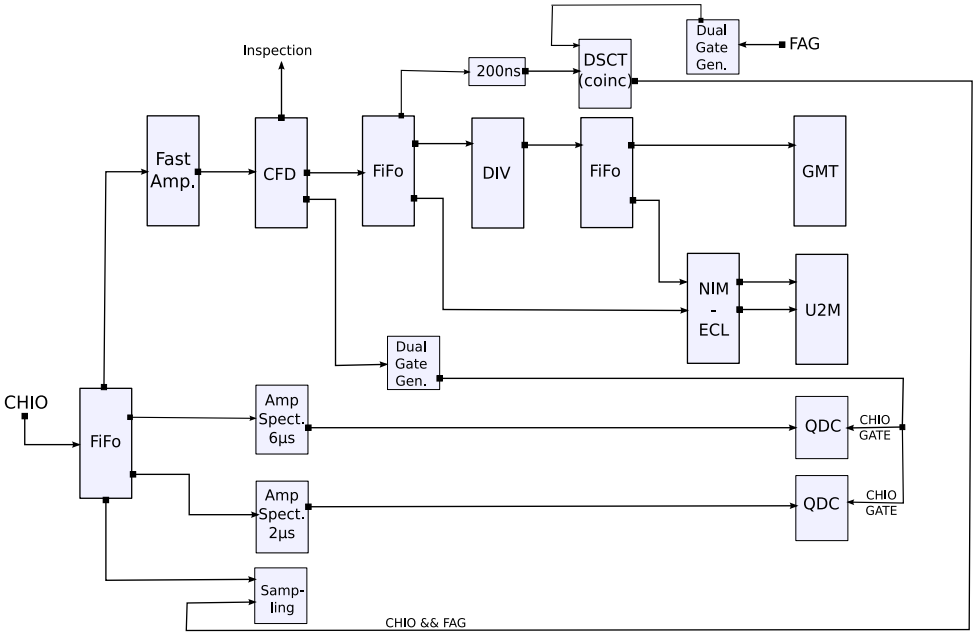

Figure B.4: *Electronic diagram associated to the ionization chamber. The time signal is used as a gate to encode the energy signal from the chamber deposited by the particle (QDC). The same signal in coincidence with FAG generates a gate to enable sampling. The time signal is also sent to the scalers (U2M) and to GMT after division.*

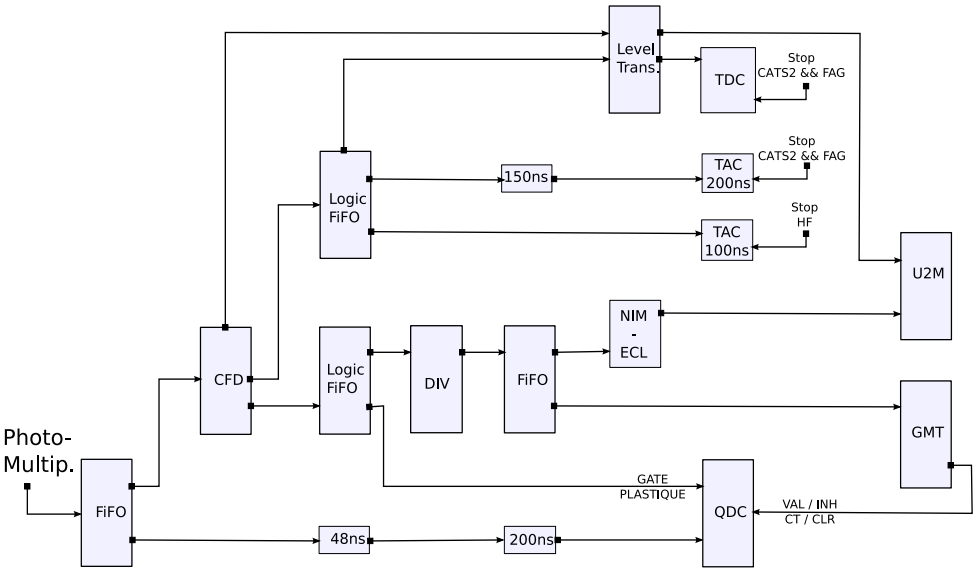

Figure B.5: *Electronic diagram associated to the plastic detector. The time signal is used as a gate to encode the energy signal from the photodiode deposited by the particle (QDC), and as a reference for measuring the time between CATS2(HF) providing the stop signal and the plastic (TAC/TDC). The same signal is also sent to the scalers (U2M) and used to generate the signal FAG (GMT) after division.*

Appendix C

Distorted Wave Born Approximation

In the present appendix the formalism involved in the microscopic description of nucleon-nucleus scattering based on Distorted-Wave Born Approximation (DWBA) will be briefly presented. In this approximation the incoming and outgoing particles are described by plane and spherical waves respectively, which get distorted by some average potential usually tuned to reproduce the elastic scattering. An in-depth description of the formalism can be found in references [Aust 70, Satc 83].

C.1 Elementary scattering theory

The type of reaction considered has the following form,

$$A + \underbrace{(b+x)}_{a} \rightarrow \underbrace{(A+x)}_{B} + b \tag{C.1}$$

where x represents the transferred particle(s). In the entrance channel (A+a) will be denoted by α and the exit channel $(b+B)$ by β. An incident beam of particles having mass m and velocity v_α can be associated to a plane wave ψ_{inc} in the center of mass (CM) coordinate system such as,

$$\psi_{inc} = N^{\frac{1}{2}} A_0 \exp(i\overrightarrow{k_\alpha} \cdot \overrightarrow{r_\alpha}) \tag{C.2}$$

where, N is the number of particules per area unit in the target which is considered as equal to unity while A_0 is related to the number of incident particles per area unit per time unit. The incident wave function describing the state of the system before the collision occurs becomes,

$$\psi_{inc} = A_0 exp(i\overrightarrow{k_\alpha} \cdot \overrightarrow{r_\alpha}) \tag{C.3}$$

After the collision the scattered particles will be associated with a scattered spherical wave function. At large distance from the target, the scattered wave tends to be of spherical form and can be represented as,

$$\psi_{scatt} \sim f_{\alpha\beta} \frac{\exp(ik_\beta r_\beta)}{r} \tag{C.4}$$

where $f_{\alpha\beta}$ is known as the "scattering amplitude" and depends in general on the angle of emission θ and the azimuthal angle ϕ with respect to the collision axis. The number of scattered particles in time unit seen by a detector, placed at a large distance and covering an area dS, is expressed as,

$$v_\beta |\psi_{scatt}(r_\beta)|^2 dS \tag{C.5}$$

where $|\psi_{scatt(r_\beta)}|^2$ is the probability density that the particles are at a position (r_β) from the collision point. Replacing $|\psi_{scatt}(r)|$ by its equivalent from equation C.4, we get,

$$v_\beta |\psi_{scatt}|^2 dS = v_\beta \left| f_{\alpha\beta} \frac{\exp(ik_\beta r_\beta)}{r_\beta} \right|^2 dS = v_\beta |f_{\alpha\beta}|^2 d\Omega \tag{C.6}$$

where $d\Omega = dS/|r|^2$ is the solid angle covered by the detector. The differential cross section can than be expessed as,

$$\frac{d\sigma_{\alpha\beta}}{d\Omega} = \frac{v_\beta}{v_\alpha} |f_{\alpha\beta}|^2 \tag{C.7}$$

The problem of finding $\frac{d\sigma_{\alpha\beta}}{d\Omega}$ reduces than to finding the scattering amplitude $|f_{\alpha\beta}|$.

C.2 Distorted waves

The differential cross section for the reaction given by equation C.1 can be written as,

$$\frac{d\sigma_{\alpha\beta}}{d\Omega} = \frac{\mu_\alpha \mu_\beta}{(2\pi\hbar^2)^2} \frac{k_\beta}{k_\alpha} \frac{1}{(2J_a+1)(2J_A+1)} |T_{\alpha\beta}|^2 \tag{C.8}$$

where,

- μ_α and μ_β are the reduced masses of the entrance α and exit β channels,
- k_α and k_β are the corresponding wave numbers,
- J_a and J_A are the spins associated to the interacting nuclei in channel α,
- and $T_{\alpha,\beta}$ is the corresponding transition amplitude related to the scattering amplitude by,

$$T_{\alpha\beta} = -\frac{2\pi\hbar^2}{\mu_\beta} f_{\alpha\beta} \tag{C.9}$$

Finding $|T_{\alpha\beta}|$ theoretically requires solving the time-independant Schrödinger equation for the total wave Ψ with the boundary conditions presented above,

$$H_{tot}\Psi = E_{tot}\Psi \tag{C.10}$$

As an exact solution is not possible, alternative ways made up of several approximations are used to solve the problem. The total Hamiltonian can be written in terms of the entrance channel α as well as the exit channel β,

$$H_{tot} = H_\alpha + K_\alpha + V_\alpha = H_\beta + K_\beta + V_\beta \tag{C.11}$$

- $H_\alpha = H_a + H_A$ represents the internal Hamiltonian[1] for the nuclei a and A described by the wave functions ψ_A and ψ_a, respectively,

[1] $H_\alpha\psi_\alpha = E_\alpha\psi_\alpha \quad \Leftrightarrow \quad H_a\psi_a = E_a\psi_a, \quad H_A\psi_A = E_A\psi_A$

- K_α is their relative kinetic energy,
- V_α is their mutual interaction.

The same goes for H_β, K_β and V_β corresponding to the exit channel β. The potential $V_{\alpha(\beta)}$ can be divided into two parts by introducing an arbitrary auxiliary potential that will be used later in DWBA approximations,

$$V_{\alpha(\beta)} = W_{\alpha(\beta)} + U_{\alpha(\beta)} \tag{C.12}$$

$U_{\alpha(\beta)}$ is the auxilliary potential normaly chosen to be an optical potential describing the elastic channel and $W_{\alpha(\beta)}$ is the residual interaction. The total Hamiltonian in this case can be written as,

$$(E_{\alpha(\beta)} - H_{\alpha(\beta)} - K_{\alpha(\beta)} - U_{\alpha(\beta)})\Psi_{\alpha(\beta)} = W_{\alpha(\beta)}\Psi_{\alpha(\beta)} \tag{C.13}$$

We define $\chi_{\alpha(\beta)}$ as the exact solutions of the homogeneous part of equation C.13 called the **distorted waves** (by the potential $U_{\alpha(\beta)}$) where,

$$(E_{\alpha(\beta)} - H_{\alpha(\beta)} - K_{\alpha(\beta)} - U_{\alpha(\beta)})\chi_{\alpha(\beta)} = 0 \tag{C.14}$$

A formal solution of the Schrödinger equation of the total Hamiltonian using the distorted waves leads to an expression of $T_{\alpha,\beta}$ given by,

$$T_{\alpha\beta} = T^0_\beta \delta_{\alpha\beta} + \langle \chi^-_\beta \psi_\beta | W_\beta | \Psi^+_\alpha \rangle \quad (prior) \tag{C.15}$$

$$= T^0_\beta \delta_{\alpha\beta} + \langle \Psi^-_\beta | W_\alpha | \chi^+_\alpha \psi_\alpha \rangle \quad (post) \tag{C.16}$$

Where T^0_β is the elastic transition amplitude due to $U_{\beta(\alpha)}$ alone and $\delta_{\alpha\beta}$ is the kroeneker factor equal to 1 for $\alpha = \beta$ and *zero* for any other case. The "prior" and "post" forms are due to wheter we express the Hamiltonian with respect to channel α or β respectively. In the case of a transfer reaction, the transition amplitude is reduced only to the second term on the right-hand side.

C.3 Born Approximation

The expression of the transition amplitude presented in the section above is exact but is only a formal solution since it contains the unkown total wave function Ψ_α. Approximations are to be made in order to solve the problem. An expansion of Ψ_α into a distorted waves Born series in terms of the residual interaction W is possible using the Green function technique,

$$\Psi^+_\alpha = \left[1 + G^+_\alpha W_\alpha + G^+_\alpha W_\alpha G^+_\alpha W_\alpha + ...\right] \chi^+_\alpha \psi_\alpha \tag{C.17}$$

where G^+_α is the distorted-wave propagator for the potential U_α associated to the Hamiltonian $H_{tot} = H_\alpha + K_\alpha + V_\alpha$. Injecting the total wave function Ψ^+_α (equation C.17) in expression C.15, the transition amplitude for a transfer reaction ($\delta_{\alpha\beta} = 0$) writes as,

$$T_{\alpha\beta} = \langle \chi^-_\beta \psi_\beta | W_\beta + W_\beta G^+_\alpha W_\alpha + W_\beta G^+_\alpha W_\alpha G^+_\alpha W_\alpha + ... | \chi^+_\alpha \psi_\alpha \rangle \tag{C.18}$$

The Born approximation consists of considering only the first term of the expansion and assuming all the other terms negligible. $T_{\alpha\beta}$ can be finally written as,

$$T_{\alpha\beta} = \langle \chi_\beta^- \psi_\beta | W_\beta | \chi_\alpha^+ \psi_\alpha \rangle \tag{C.19}$$

The validity of the DWBA depends upon elastic scattering being dominant process so that the other processes can be treated as perturbations.

C.4 Transition potential

The potential of mutual interaction V_β between b and $A+x$ (see equation C.1) is assumed to be the result of two-body forces. Under this condition it can be written as,

$$V_\beta = \sum_{i=1}^{b} \sum_{j=1}^{B=A+x} v_{ij} = \sum_{i=1}^{b} \sum_{j=1}^{A} v_{ij} + \sum_{i=1}^{b} \sum_{k=1}^{x} v_{ik} \tag{C.20}$$

where the sums run over all the nucleons in b or B. In case of a (d,p) transfer reaction we have,

$$b \equiv p, \quad a \equiv d, \quad x = n \tag{C.21}$$

In this case the mutual interaction V_β reduces to,

$$V_\beta = \sum_{j=1}^{B=A+x} v_{pj} = \sum_{j=1}^{A} v_{pj} + V_{pn} = V_{pA} + V_{pn} \tag{C.22}$$

where V_{pn} and V_{pA} are the interactions between the outgoing proton and the transferred neutron and the remaining nucleons in B, respectively. Replacing the new expression of V_β in equation C.12 we get for the residual interaction W_β the following expression,

$$W_\beta = V_{pn} + \underbrace{(V_{pA} - U_\beta)}_{\approx 0} \sim V_{pn} \tag{C.23}$$

The nucleus B differs only by the addition of one neutron to nucleus A. Both nuclei have the same charge and very similar masses. To a first approximation, we have $(V_{pA} - U_\beta) \approx 0$. This approximation is further strengthen by the fact that the transferred part x (neutron) is small next to A which in our case is ^{68}Ni. Replacing the new expression of W_β the transition amplitude (equation C.19) becomes,

$$T_{\alpha\beta} = \langle \chi_\beta^- \psi_\beta | V_{pn} | \psi_\alpha \chi_\alpha^+ \rangle \tag{C.24}$$

$$= \int \chi_\beta^{-*} \langle \psi_\beta | V_{pn} | \psi_\alpha \rangle \chi_\alpha^+ dr_\alpha dr_\beta \tag{C.25}$$

where the matrix element $\langle \psi_\beta | V_{pn} | \psi_\alpha \rangle$ is responsable for all non elastic processes. It contains all the information on the nuclear structure and is usually called the **form factor**. The interaction $V_{pn} (\equiv V_{pn}(\overrightarrow{r_{pn}}))$ is considered as a function of the distance between the proton and the neutron, thus we can factorize the matrix element as follows,

$$\langle \psi_\beta | V_{pn} | \psi_\alpha \rangle = \langle \psi_B \psi_b | V_{pn} | \psi_a \psi_A \rangle \tag{C.26}$$

$$= \langle \psi_B | \psi_A \rangle \langle \psi_b | V_{pn} | \psi_a \rangle \tag{C.27}$$

Zero-range approximation

Our calculations were done in the zero-range approximation. This approximation has the physical meaning that the proton is emitted at the same point at which the deuteron were absorbed [Aust 70]. In other words the distance of proton and neutron inside the deuteron is zero. The approximation consists of replacing the second term $\langle\psi_b|V_{pn}|\psi_a\rangle$ on the right-hand side by a delta-Dirac function,

$$\langle\psi_b|V_{pn}|\psi_a\rangle = D_0\delta(\overrightarrow{r_{pn}}) \tag{C.28}$$

where D_0 is a constant. This approximation reduces the integral of the matrix element from 6 to 3 dimensions and is intended to simplify the calculations.

C.5 Form factor

In order to calculate $\langle\psi_B|\psi_A\rangle$, the wave function ψ_B may be expanded in terms of a complete set of states ψ_{γ_A} of the A nucleons that correspond to the core nucleus A,

$$\psi_B = (\xi_A, \xi_n) = \sum_{lj} C_J \;\; C_T \;\; \psi_{\gamma_A}(\xi_A) \;\; \phi_{\gamma_n}(r_{An}) \tag{C.29}$$

where,

- ξ_A is the internal variables of the core nucleus A,
- $C_J = \langle J_A j M_A m|J_B M_B\rangle$ is the angular momentum coupling (Clebsh-Gordon coefficients) of the neutron to the core nucleus,
- $C_T = \langle T_A N_A tn|T_B N_B\rangle$ is the isospin coupling,
- $\gamma_A \equiv \{A, J_A, M_A, T_A, N_A\}$ corresponds to the number of nucleons, spin, spin projection on $z-axis$, isospin and isospin projection on $z-axis$ in the core nucleus A, respectively,
- $\phi_{\gamma_n}(r_{An})$ is defined as the overlap function. It is obtained by solving the radial Schrödinger equation for some effective interaction potential $V(r)$. The last is adjusted in order to reproduce the binding energy E_B of the neutron in nucleus B. In our calculations we chose a Woods-Saxon potential form for $V(r)$, widely used in DWBA analysis.
- $\gamma_n \equiv \{l, j, m, t, n\}$ corresponds to the angular momentum, spin, spin projection on $z-axis$, isospin and isospin projection on $z-axis$ of the transferred neutron, respectively.

With expression C.29 of ψ_B, the overlap $\langle\psi_B|\psi_\alpha\rangle$ is calculated as,

$$\langle\psi_B|\psi_A\rangle = \sum_{lj} C_J \;\; C_T \int \psi^*_{\gamma_A}(\xi_A) \;\; \phi^*_{\gamma_n}(\xi_n) \;\; \psi_{\gamma_A}(\xi_A)\; d\xi_A \tag{C.30}$$

$$= \sum_{lj} C_J \;\; C_T \phi^*_{\gamma_n}(\xi_n) \underbrace{\int \psi^*_{\gamma_A}(\xi_A) \;\; \psi_{\gamma_A}(\xi_A)\; d\xi_A}_{=1} \tag{C.31}$$

$$= \sum_{lj} C_J \;\; C_T \phi^*_{\gamma_n}(\xi_n) \tag{C.32}$$

where $C_T\phi^*_{\gamma_n}(\xi_n)$ is related to the spectroscopic factor $\widetilde{S}_{lj}$ by,

$$\widetilde{S}_{lj} = C_T^2 \int |\phi_{\gamma_n}|^2 d\xi_n = C_T^2 S \tag{C.33}$$

$\widetilde{S}_{lj}$ gives a measurement of the overlap between the initial and final nuclei A and B, respectively. It corresponds to the probability of finding B (described by ψ_B) composed of a neutron moving as a single-particle with angular momentum l and spin j relative to the nucleus A (described by ψ_A).

In the case of a neutron transfer on a neutron-rich nucleus in its ground state the isospin coefficient C^2 is equal to 1. In practice the overlap function is assumed to be proportional to the wave function ψ_{γ_n} for a nucleon bound in the orbital generated by a potential (Woods-Saxon in our case) after solving the Schrödinger equation.

$$\phi_{\gamma_n}(\xi_n) \approx \beta_{lj}\psi_{\gamma_n}(\xi_n) \tag{C.34}$$

where β_{lj} represents the spectroscopic amplitude and ψ_{γ_n} is normalised to unity. With this final approximation, the spectroscopic factor is given as,

$$\widetilde{S}_{lj} = C_T^2 S_{lj} = C_T^2 \beta_{lj}^2 \tag{C.35}$$

C.6 Selection and sum rules

C.6.0.1 Selection rules: Angular momenta

The differential cross section depends sensitively on the transferred angular momentum in a transfer reaction. By a comparison between the measured angular distribution with the one calculated by a suitable transfer-reaction model such as the DWBA, the transferred angular momentum can be determined.

Let $\overrightarrow{J_a}$, $\overrightarrow{J_b}$ and $\overrightarrow{s}$ be the total spins of nuclei a, b and x, respectively. Where x is coupled to b ($a = b + x$) by the angular momentum $\overrightarrow{l'}$ before the transfer occurs. The spins are related through the following equations,

$$\overrightarrow{J_a} = \overrightarrow{J_b} + \overrightarrow{j'} \quad where \quad \overrightarrow{j'} = \overrightarrow{l'} + \overrightarrow{s} \tag{C.36}$$

After the transfer x will be coupled to A by $\overrightarrow{l}$. Considering the total spins of the A and B given by $\overrightarrow{J_a}$ and $\overrightarrow{J_B}$, respectively we can write,

$$\overrightarrow{J_B} = \overrightarrow{J_A} + \overrightarrow{j} \quad where \quad \overrightarrow{j} = \overrightarrow{l} + \overrightarrow{s} \tag{C.37}$$

According to the selection rules given by equations C.36 and C.37 the transferred spins can be identified by,

$$J_{BA} = j \quad and \quad J_{ba} = -j' \tag{C.38}$$

and the transferred angular momenta by,

$$\overrightarrow{l_{tr}} = \overrightarrow{l} - \overrightarrow{l'} \quad \Longleftrightarrow \quad |l - l'| \leqslant l_{tr} \leqslant (l + l') \tag{C.39}$$

A (d, p) transfer over a core nucleus in its ground state simplifies the above selection rules. The proton and neutron in the deuteron are coupled to an S state[2] ($l' = 0$) and $j' = s$ is simply the intrinsic spin of the neutron. Nucleus A is in its ground state during the transfer. If A is an even-even nucleus $J_A = 0 \Rightarrow J_{BA} = j = J_B$ and the transferred spin is equal to the spin of nucleus B. In this case the transferred angular momentum l_{tr} can be identified by l since,

$$|l - 0| \leqslant l_{tr} \leqslant (l + 0) \tag{C.40}$$

Thus the final state J_B can only correspond to the occupation of a defined orbital (l, j) in nucleus B. The probing power of single-nucleon transfers from light ions (*e.g.* deuteron) resides in this fact. It is not necessarily the case in other type of transfer reaction where J_B may have contributions from two or more different l values or, conversely, a given l can couple with a $J_A \neq 0$ to give several states with different J_B values.

C.6.0.2 Selection rules: Parity conservation

The parity conservation is expressed by,

$$\pi_a \pi_b = (-1)^l \quad and \quad \pi_A \pi_B = (-1)^l \tag{C.41}$$

where π_a, π_b, π_A and π_B represent the nuclei a, b, A and B, respectively. For $J_A^{\pi_A} = 0^+$ the parity of the final state in B is totaly determined by the transferred angular momentum l according to C.41.

C.6.0.3 Sum Rules: Spectroscopic factors

The spectroscopic factors are subject to sum rules. In general, all the force corresponding to a given orbital j is fragmented over several states. Summing over all these states, one can say how much the orbital j is occupied in the initial nucleus. For a $A(a, b)B$ reaction this sum rule is written as,

$$\sum_{\gamma_B J_B} \widetilde{S}_{lj} \frac{2J_B + 1}{2J_A + 1} = h(l, j) \tag{C.42}$$

[2]The coupling contains also small admixtures with a D state that we may neglect.

where the sum is over all final states in B, with spin J_B and γ_B which represent any other labels to specify the state. $h(l,j)$ is the average number of holes of the same type of the transferred particle in the l,j shell in B and is related to the number of particles $n(l,j)$ by,

$$(2j+1) - n(l,j) = h(l,j) \tag{C.43}$$

In the case of a (d,p) transfer on an even-even target A in its ground state ($J_A = 0, J_B = j$) the equation reduces to,

$$\sum_{\gamma_B j} \widetilde{S}_{lj} = \frac{h(l,j)}{2j+1} \tag{C.44}$$

Moreover, when the shell (l,j) is empty in A, the sum is maximum and equals to 1 since,

$$n(l,j) = 0 \Leftrightarrow h(l,j) = 2j+1 \tag{C.45}$$

In order to determine the spectroscopic factor of a state populated experimentally, the measured differential cross section is normalized to that calculated by DWBA for which it was assumed a spectroscopic factor of value 1 and a defined orbital (l,j). The experimental value of the spectroscopic factor is then given by the relation,

$$\frac{d\sigma}{d\Omega}(Exp.) = C^2 S_{lj} \frac{d\sigma}{d\Omega}(DWBA) \tag{C.46}$$

Appendix D

Shell-model calculations

$1g_{9/2}$		$2d_{5/2}$	
Energy [MeV]	SF	Energy [MeV]	SF
0.000000	0.888915	1.485330	0.794864
1.322149	0.000267	1.924422	0.091486
2.558006	0.001538	2.276588	0.004717
3.096662	0.004050	4.121419	0.007465
3.621179	0.000451	5.799263	0.031467
4.186779	0.001510	7.057368	0.022430
4.676600	0.003883	9.539168	0.007425
5.226059	0.010558		
5.693810	0.012324		
6.576853	0.007392		
7.426272	0.002271		
8.331960	0.002087		
9.344536	0.001182		

Table D.1: *Calculated shell-model energies less than* 10 MeV *and the associated spectroscopic factors for* $1g_{9/2}$ *and* $2d_{5/2}$ *orbitals in* ^{69}Ni*. The details of calculations are given in section 4.5.1.*

$1g_{9/2}$		$2d_{5/2}$	
Energy [MeV]	SF	Energy [MeV]	SF
0.000000	0.859548	2.123670	0.455986
1.593508	0.001318	2.499782	0.426897
2.951499	0.002215	3.125776	0.004113
3.470140	0.004494	4.342080	0.005666
4.523452	0.001229	5.306435	0.004558
5.551562	0.020939	6.194903	0.050271
6.858692	0.007963	7.216955	0.015052
8.178668	0.003196	8.403852	0.005810
9.855066	0.001321	10.134947	0.002829

Table D.2: *Calculated shell-model energies less than* 10 MeV *and the associated spectroscopic factors for* $1g_{9/2}$ *and* $2d_{5/2}$ *orbitals in* ^{69}Ni*. In this calculations the single-particle energy of the* $2d_{5/2}$ *orbital has been shifted* 1 MeV *to higher energies relative to the current interaction in order to better reproduce the experimental results. The details of calculations are given in section 4.5.1.*

$1g_{9/2}$		$2d_{5/2}$	
Energy [MeV]	SF	Energy [MeV]	SF
0.000002	0.932799	2.094752	0.049150
1.353808	0.001583	2.917429	0.795709
2.967356	0.004835	3.629198	0.027003
3.896914	0.003275	6.098971	0.066492
5.579645	0.025945	7.571749	0.029075
7.408907	0.010093	10.754938	0.008517
9.717280	0.004368		

Table D.3: *Calculated shell-model energies less than* 10 MeV *and the associated spectroscopic factors for* $1g_{9/2}$ *and* $2d_{5/2}$ *orbitals in* ^{69}Ni*. In this calculations the single-particle energy of the* $2d_{5/2}$ *orbital has been shifted by* 2 MeV *to higher energies relative to the current interaction. The details of calculations are given in section 4.5.1.*

Bibliography

[Abzo 91] A. Abzouzi *et al. Phys. Rev. Lett.*, Vol. 66, p. 1134, 1991. (Cited page 7.)

[Anne 92] R. Anne and A. C. Mueller. *Nucl. Instr. and Meth. B*, Vol. 70, 1992. (Cited in pages vi, xxii and 23.)

[Aust 70] N. Austern. *Direct nuclear reaction theories*, Chap. 5, p. 100. 1970. (Cited in pages 109 and 113.)

[Baro 03] P. Baron *et al.* In: *IEEE Nuclear Science Symposium Conference*, IEEE Nuclear and Plasma Sciences Society, Portland, United States of America, 2003. (Cited page 33.)

[Bern 82] M. Bernas *et al. Phys. Lett. B*, Vol. 113, p. 279, 1982. (Cited page 10.)

[Blum 99] Y. Blumenfeld *et al. Nucl. Instr. and Meth. A*, Vol. 421, p. 471, 1999. (Cited in pages vii, xxii and 29.)

[Bosc 88] U. Bosch *et al. Nucl. Phys. A*, Vol. 477, p. 89, 1988. (Cited page 14.)

[Brod 95] R. Broda *et al. Phys. Rev. Lett.*, Vol. 74, p. 868, 1995. (Cited in pages v, xxi and 10.)

[Burg 11] G. Burgunder. PhD thesis, université de Caen, France, 2011. (Cited page 101.)

[Catf 03] W. Catford *et al.* In: , Ed., *Tours Symposium on Nuclear Physics V*, p. 185, Tours, France, 26-29 August 2003. (Cited page 25.)

[Caur 05] E. Caurier *et al. Rev. Mod. Phys.*, Vol. 77, p. 427, 2005. (Cited in pages xiv and 97.)

[Caur 94] E. Caurier *et al. Phys. Rev. C*, Vol. 50, p. 225, 1994. (Cited page 7.)

[Daeh 80] W. Daehnick *et al. Phys. Rev. C*, Vol. 21, p. 2253, 1980. (Cited page 82.)

[Dess 84] P. Dessagne *et al. Nucl. Phys. A*, Vol. 426, p. 399, 1984. (Cited page 14.)

[Detr 79] C. Détraz *et al. Phys. Rev. C*, Vol. 19, p. 164, 1979. (Cited page 8.)

[Dijo 11] A. Dijon *et al. submitted to Phys. Rev. Lett.*, 2011. (Cited page 11.)

[Doba 94] J. Dobaczewski *et al. Phys. Rev. Lett.*, Vol. 72, p. 981, 1994. (Cited page 10.)

[Dufo 96] M. Dufour and A. P. Zuker. *Phys. Rev. C*, Vol. 54, p. 1641, 1996. (Cited in pages 6 and 7.)

[Elsa 34] W. Elsasser. *J. de Phys. et Rad.*, Vol. 5, p. 625, 1934. (Cited page 2.)

[Flan 09] K. T. Flanagan *et al.* *Phys. Rev. Lett.*, Vol. 103, p. 142501, 2009. (Cited page 96.)

[Fran 01] S. Franchoo *et al.* *Phys. Rev. C*, Vol. 64, p. 054308, 2001. (Cited in pages 14 and 96.)

[Fran 98] S. Franchoo *et al.* In: *Exotic Nuclei and Atomic Masses*, p. 757, Woodbury, N.Y., 1998. (Cited page 14.)

[Gale 88] S. Galès, C. Stoyanov, and A. Vdovin. *Physics Reports*, Vol. 166, p. 125, 1988. (Cited page 76.)

[Giro 11] S. Giron. PhD thesis, Université Paris Sud - Paris XI, France, 2011. (Cited in pages xiii, 25, 37, 52, 58 and 77.)

[Goep 49] M. Goeppert-Mayer. *Phys. Rev.*, Vol. 75, p. 1969, 1949. (Cited page 2.)

[Grzy 98] R. Grzywacz *et al.* *Phys. Rev. Lett.*, Vol. 81, p. 766, 1998. (Cited in pages 14, 15 and 95.)

[Guil 84] D. Guillemaud-Mueller *et al.* *Nucl. Phys. A*, Vol. 426, p. 37, 1984. (Cited page 8.)

[Harv 71] J. D. Harvey and R. C. Johnson. *Phys. Rev. C*, Vol. 3, p. 636, 1971. (Cited page 82.)

[Haxe 49] O. Haxel *et al.* *Phys. Rev.*, Vol. 75, p. 1766, 1949. (Cited page 2.)

[John 70] R. C. Johnson and P. J. R. Soper. *Phys. Rev. C*, Vol. 1, p. 976, 1970. (Cited page 82.)

[Joki 97] A. Jokinen *et al.* *Nucl. Instr. and Meth. B*, Vol. 126, p. 95, 1997. (Cited page 14.)

[Kane 08] K. Kaneko *et al.* *Phys. Rev. C*, Vol. 78, p. 064312, 2008. (Cited page 13.)

[Koni 03] A. Koning and J. Delaroche. *Nucl. Phys. A*, Vol. 713, p. 231, 2003. (Cited in pages xii and 83.)

[Kunz 74] P. D. Kunz. "DWUCK4 computer code". 1974. University of Colorado. (Cited in pages xii and 83.)

[Lau 95] K. Lau and J. Pyrlik. *Nucl. Instr. and Meth. A*, Vol. 366, p. 298, 1995. (Cited in pages viii, 42, 43 and 45.)

[Lenz 10] S. M. Lenzi *et al.* *Phys. Rev. C*, Vol. 82, p. 054301, 2010. (Cited in pages xiv, xxii, 9, 13, 91 and 97.)

[Ljun 10] J. Ljungvall *et al.* *Phys. Rev. C*, Vol. 81, 2010. (Cited in pages v, xiv, xxi, 12, 93 and 97.)

[Lomb 83] R. Lombard and D. Mas. *Phys. Lett. B*, Vol. 120, p. 23, 1983. (Cited page 10.)

[Mach 03] H. Mach *et al. Nucl. Phys. A*, Vol. 719, p. C213, 2003. (Cited page 15.)

[Mich 64] A. Michalowicz. *Cinématique des réactions nucléaires*, Chap. 2, p. 78. 1964. (Cited in pages x and 66.)

[Micr 10] Micron. "Micron Semiconductors Catalogue". 2010. www.micronsemiconductor.co.uk. (Cited in pages vii, 28 and 63.)

[Moto 95] T. Motobayashi *et al. Phys. Lett. B*, Vol. 346, p. 9, 1995. (Cited page 8.)

[Moug 08] X. Mougeot. PhD thesis, Université Paris VII - Denis Diderot, France, 2008. (Cited in pages 32 and 33.)

[Muel 99] W. F. Mueller *et al. Phys. Rev. Lett.*, Vol. 83, p. 3613, 1999. (Cited in pages 14 and 95.)

[NNDC] NNDC. "National Nuclear Data Center". www.nndc.bnl.gov. (Cited page 8.)

[Otsu 01] T. Otsuka *et al. Phys. Rev. Lett.*, Vol. 87, p. 082502, 2001. (Cited page 9.)

[Otsu 10] T. Otsuka *et al. Phys. Rev. Lett.*, Vol. 105, p. 032501, 2010. (Cited page 7.)

[Otti 99] S. Ottini-Hustache *et al. Nucl. Instr. and Meth. A*, Vol. 431, p. 476, 1999. (Cited in pages vii, viii, xxii, 20, 43 and 47.)

[Parz 62] E. Parzen. *Annals of mathematical statistics*, Vol. 33, p. 1065, 1962. (Cited in pages xi and 73.)

[Pauw 10] D. Pauwels *et al. Phys. Rev. C*, Vol. 82, p. 027304, 2010. (Cited page 11.)

[Poll 05] E. Pollacco *et al. Eur. Phys. J. A*, Vol. 25, p. 287, 2005. (Cited in pages vii, xxii, 21 and 29.)

[Pris 99] J. I. Prisciandaro *et al. Phys. Rev. C*, Vol. 60, p. 054307, 1999. (Cited page 14.)

[Pull 08] S. Pullanhiotan *et al. Nucl. Instr. and Meth. A*, Vol. 593, p. 343, 2008. (Cited page 11.)

[Raha 07] S. Rahaman *et al. Eur. Phys. J. A*, Vol. 32, p. 87, 2007. (Cited page 10.)

[Rama 01] S. Raman *et al. Atomic Data and Nuclear Data Tables*, Vol. 78, p. 1, 2001. (Cited in pages 1 and 2.)

[Ramu 09] A. Ramus. PhD thesis, Université Paris Sud - Paris XI, France, 2009. (Cited page 38.)

[Satc 83] G. R. Satchler. *Direct nuclear reactions*. 1983. (Cited in pages 82 and 109.)

[Siej 10] K. Sieja and F. Nowacki. *Phys. Rev. C*, Vol. 81, p. 061303, 2010. (Cited in pages 91, 96 and 98.)

[Simp 00] J. Simpson *et al.* *Acta Physica Hungarica New Series Heavy Ion Physics*, Vol. 11, p. 159, 2000. (Cited in pages 11 and 36.)

[Sorl 02] O. Sorlin *et al.* *Phys. Rev. Lett.*, Vol. 88, p. 092501, 2002. (Cited in pages v, xxi and 10.)

[Sorl 03] O. Sorlin *et al.* *Eur. Phys. J. A*, Vol. 16, p. 55, 2003. (Cited in pages v, xxi, 12 and 13.)

[Varn 91] R. Varner *et al.* *Physics Reports*, Vol. 201, p. 57, 1991. (Cited in pages xii and 83.)

[Verk 03] W. Verkerke and D. Kirkby. *arXiv:physics/0306116v1*, 2003. RooFit Toolkit for Data Modeling. (Cited page 73.)

[Warb 90] E. K. Warburton *et al.* *Phys. Rev. C*, Vol. 41, p. 1147, 1990. (Cited page 9.)

[Zieg 77] J. F. Ziegler *et al.* *Hydrogen stopping powers and ranges in all elements*. Vol. 3, 1977. (Cited page 52.)

[Zuke 95] A. P. Zuker *et al.* *Phys. Rev. C*, Vol. 52, p. R1741, 1995. (Cited page 9.)

Résumé:

La fermeture de couche de l'oscillateur harmonique à $N = 40$ dans le ^{68}Ni est faible et perd sa rigidité après l'enlèvement (ou l'ajout) de paires de protons. Les calculs effectués dans cette région de masse prédisent un nouvel îlot d'inversion à $N = 40$ semblable à celui à $N = 20$ et montrant que le placement de l'orbital neutron $2d_{5/2}$ est un ingrédient essentiel pour l'interprétation de la structure nucléaire à $N \sim 40$. La différence d'énergie $1g_{9/2} - 2d_{5/2}$ a été déterminée dans le noyau ^{69}Ni en utilisant la réaction de transfert d'un neutron d(^{68}Ni,p) en cinématique inverse. L'expérience réalisée au GANIL utilisait un faisceau de ^{68}Ni à 25,14 MeV/u. Les noyaux ^{68}Ni séparés par le spectromètre LISE3 ont ensuite interagit avec une cible de CD_2 d'épaisseur 2,6 mg/cm^2. Le dispositif expérimental était composé principalement des détecteurs CATS/MUST2-S1/EXOGAM couplés à une chambre d"ionisation et un scintillateur plastique. Les moments angulaires et les facteurs spectroscopiques de l'état fondamental ($J^\pi = 9/2^+$) et d'un doublet d'états ($J^\pi = 5/2^+$) autour de 2,48 MeV, associés à la population des orbitales $1g_{9/2}$ et $2d_{5/2}$, ont été obtenus après la comparaison des sections efficaces différentielles et des calculs ADWA. Les spins des états observés ont été attribués après comparaison aux calculs de modèles en couches dans un grand espace de valence. La position de l'orbitale $2d_{5/2}$ dans ^{69}Ni a été établie pour la première fois. Nos mesures confirment l'hypothèse de la faible différence d'énergie ($\sim$2,5 MeV) entre l'orbitale neutron $2d_{5/2}$ et l'orbitale $1g_{9/2}$ et son importance pour décrire la structure des noyaux autour de $N = 40$.

Mots clés: Structure nucléaire, Noyaux riches en neutrons, Ilôt d'inversion $N = 40$, calculs de modèle en couches, Réaction de transfert, Cinématique inverse.

Abstract:

The harmonic oscillator shell closure at $N = 40$ in ^{68}Ni is weak and loses its strength when removing (or adding) pair of protons. Calculations performed in this mass region predict a new island of inversion at $N = 40$ similar to the one at $N = 20$. Using a large valence space, the neutron orbital $2d_{5/2}$ is shown to be a crucial ingredient for the interpretation of the nuclear structure at $N \sim 40$. The neutron $1g_{9/2} - 2d_{5/2}$ energy difference has been determined in ^{69}Ni using the d(^{68}Ni,p) transfer reaction in inverse kinematics. The experiment performed at GANIL used a ^{68}Ni beam at 25.14 MeV/u seperated by the LISE3 spectrometer was impinging a CD_2 target of 2.6 mg/cm^2 thickness. The experimental setup consisted of CATS/MUST2-S1/EXOGAM detectors coupled to an ionization chamber and a plastic scintillator. The angular momenta and spectroscopic factors of the ground state ($J^\pi = 9/2^+$) and a doublet of states ($J^\pi = 5/2^+$) around 2.48 MeV corresponding to the population of the $1g_{9/2}$ and the $2d_{5/2}$ orbitals, were obtained from the comparison between the experimental cross-sections as a function of the proton detection angle and ADWA calculations. The spins of the observed states were assigned by comparaison to large scale Shell-Model calculations. The position of the $2d_{5/2}$ orbital in ^{69}Ni has been established for the first time. Our measurements support the hypothesis of a low-lying $2d_{5/2}$ orbital ($\sim$2.5 MeV) with respect to the $1g_{9/2}$ neutron orbital and thus its major role in the structure of the nuclei around $N = 40$.

Keywords: Nuclear structure, Neutron-rich nuclei, Island of inversion $N = 40$, Shell-Model calculations, Transfer reaction, Inverse kinematics.